The role of polymeric binders in water-based lithium-ion battery electrodes

zur Erlangung des akademischen Grades eines
DOKTORS DER INGENIEURWISSENSCHAFTEN (Dr.-Ing.)

von der KIT-Fakultät für Chemieingenieurwesen und Verfahrenstechnik
des Karlsruher Instituts für Technologie (KIT)
genehmigte

DISSERTATION

von
Ronald Gordon Grajales M.Sc.
aus Cali, Kolumbien

Erstgutachter: Prof. Dr. Norbert Willenbacher
Zweitgutachter: Prof. Dr.-Ing. Wilhelm Schabel
Tag der mündlichen Prüfung: 16.02.2021

Preface

This publication based dissertation consists of three peer-reviewed scientific journal articles. They include the main results of my experimental work from January 2017 until June 2020 at the Karlsruhe Institute of Technology (KIT), Institute of Mechanical Process Engineering and Mechanics in the group of Applied Mechanics.

This thesis follows a brief introduction to the current world environmental and energy situation as well as a comprehensive state of the art on lithium-ion batteries and a detailed motivation behind the aims of this work. The main part of this dissertation consists of the following publications:

- Sedimentation of lithium-iron-phosphate and carbon black particles in opaque suspensions used for lithium-ion-battery electrodes
- Effect of polymeric binders on dispersion of active particles in aqueous $LiFePO_4$-based cathode slurries as well as mechanical and electrical properties of corresponding dry layers
- Effect of carboxymethyl cellulose on the flow behavior of lithium-ion battery anode slurries and the electrical as well as mechanical properties of corresponding dry layers

The dissertation concludes with a general summary, an outlook as well as a bibliography. The bibliography includes all references of the publications. Hereby, the publications are slightly changed. Some graphs and images are modified in size and color.

Acknowledgments

At this point, I would like to thank all people who directly or indirectly contributed to the success of my dissertation and supported me during my time at the Karlsruhe Institute of Technology (KIT).

First and foremost, my thanks go to my supervisor Prof. Dr. Norbert Willenbacher for giving me the opportunity to do my doctorate under his guidance at the Institute of Mechanical Process Engineering and Mechanics (MVM) - Applied Mechanics Group (AME) and for the trust he has placed in me. The combination of ambitious goals with great scientific freedom and creative, innovative ideas contributed significantly to the success of this work. Our fruitful discussions pushed me to become a better researcher and scientist.

Furthermore, I would like to thank Prof. Dr. Wilhelm Schabel from the Institute of Thermal Process Engineering (TVT) - Thin Film Technology (TFT) of the KIT for taking over as second referee.

My special thanks are extended to Dr. Laurent Zinck and Julia Thümmel from Innolith Science & and Technology GmbH for providing the opportunity to work at the company and at the same time work on my doctorate. The generous, constant support and encouragement towards new ideas and the development of this dissertation has been greatly appreciated.

I would also like to thank the *100 Prozent erneuerbar Stiftung* for financial support.

Further thanks are extended to Dr. Bernhard Hochstein for sharing his knowledge on rheometry and technical issues as well as giving me great advice.

I would also like to express my deep gratitude to the technical staff of the MVM, especially to Klaus Hirsch, Astrid Huber and Regina Mall for their valuable technical support as well as to Volker Zibat from the Laboratory for Electron Microscopy (LEM) for the long hours of microstructure investigation.

I particularly acknowledge the help offered by Dr. Torsten Brezesinski and Dr. Katja Kretschmer from the KIT/BASF Joint laboratory BELLA. Thanks for the nice cooperation, experimental assistance, data analysis and sharing your expertise in the field of lithium-ion batteries.

This work would not have been possible without the hard work of my students: Sijia Liu, Zeynep Senyelli, Heike Balmer, Raquel Orias, Jeannine Roland, Heiko Mild, Tamara Miličić, Aïcha Laghmani, Meriem Kassar, Andrés García, Antonio Saxler, Nicole Frías and Lena Karcher. Thank you for your interest in my research topic, your motivation and dedication. I hope you were able to learn something during your time with me, I

can assure you I learned invaluable lessons from each of you.

I am very grateful to all my colleagues at the AME as they are a great team to work with. Thank you for the numerous discussions, useful critics and constructive suggestions towards this research work. I had the best time working, laughing and partying with you. In particular, I want to thank my office colleagues Müge, Katharina, Katrin, Annika V. and Moritz (Mauricio) for sharing and listening (or at least pretend) as well as bearing with my weird self. Special thanks go to David, Walter and Mauricio for the long board-game nights, the rare, occasional drink "after" work and the great time during my doctorate. I thank Annika V. and Annika H. for numerous funny moments and laughs as well as very interesting gossiping sessions.

Meriem, aychek aali aamaltou maaya lkol. Aychek ala tachjiiek, ala sabrek, ala wakftek maaya ou hobik leya.

Last but not least, I thank my family for their never ending support, guidance, advice and motivation. Despite the distance, you are always by my side.

Abstract

One of the defining political and economic issues of the 21st century is climate change and the associated demand for climate protection strategies. To this end, the German government adopted the "Climate Action Plan 2050" with the medium-term goal of reducing greenhouse gas emissions in Germany by at least 55% by 2030 compared to 1990 levels. One approach to a sustainable and global transformation of energy generation and consumption as well as mobility is the implementation and combination of electric mobility with renewable energies. Solar and wind, are playing a greater role in power generation, offering an alternative to fossil fuels sources, but without effective energy storage these intermittent sources will continue to rely on carbon-based energies. As the immediacy of the climate crisis becomes increasingly obvious, batteries are an important building block for a renewable-fueled world. In 2010, batteries powered phones and computers but by the end of the decade, they started powering cars and houses, too. Lithium-ion batteries (LIB) are the most promising energy storage technology for use in portable devices, electric vehicles and grid due to their high specific energy and power density. Despite the constantly increasing research and development activities in LIB, further improvements are demanded with respect to their capacity, lifetime, safety and cost. In addition, environmental concerns require a shift from systems based on organic solvents to water-borne alternatives. Therefore, the development of high capacity, safe, cheap and easily recyclable LIB is of utmost importance.

Research has focused particularly on new electrochemically active materials to improve battery performance, leaving electrochemically inactive electrode components, such as polymeric binders, as a secondary aspect. However, polymers can strongly affect the flow behavior of wet electrode slurries and hence their processing behavior during electrode fabrication. The interaction between polymers and active particles as well as the thickening effect of polymers in the solvent not only influence rheological properties of electrode slurries but also particle dispersion and electrode microstructure of corresponding dry layers. Hence, the resulting component distribution in the dry electrode determines the formation of a conductive particle network, which may be decisive to achieve optimum ion and electron transport kinetics, improving, in turn, rate capability as well as cell energy and power density. Furthermore, polymeric binders ensure mechanical stability of the electrode during charge/discharge cycling of the cell, mitigating local delamination of the electrode layer from the current collector as well as cracking within the layer induced by volume fluctuations of the electrochemically active material. Thus, sufficient cohesive and adhesive strength, provided by the binder, guarantees cycle stability and extended cell life-time. Despite this fundamental knowledge on the role of polymeric binders, the final contribution of the binder to battery performance and its complex interactions with the active material lacks thorough understanding.

This thesis focuses on the role of polymeric binders in water-based electrodes for LIB. The holistic approach highlights the importance of the binder from its interaction with active materials controlling the flow behavior of the wet slurry and resulting compo-

nent dispersion state in the dry layer to its effect on electrical conductivity, mechanical integrity and microstructure of the electrode imperative to understand the true contribution of polymeric binders to cell performance. Regarding the optimal processing behavior of the slurry throughout electrode fabrication, specially during the mixing, pumping and coating steps, homogeneous particle dispersion and slurry stability against particle settling are essential. As an alternative to optical techniques, two different methods to characterize the sedimentation process of $LiFePO_4$ and carbon black (CB) particles in opaque suspensions used for LIB are presented. Noninvasive spin-echo-based magnetic resonance imaging offers new insights into the particle sedimentation, revealing the spatial distribution of the particles and corresponding agglomerates, as well as the shape of the settling front. Despite reproducible and reliable results derived from this method, low-viscosity suspensions as well as high particle mass fractions can lead to measuring signal limitations, aggravating image definition and data analysis. Hence, supplementing gravimetric experiments using a self-manufactured sedimentation balance were performed to study particle settling at high, technically relevant concentrations. This technique enables the characterization of the sedimentation behavior of highly concentrated, water-based electrode slurries including $LiFePO_4$, CB and polymeric binders, yielding conclusive results. Accordingly, the presented methods render a reliable combination to characterize the sedimentation behavior of opaque suspensions with different particle loading for LIB.

Water-based cathodes including $LiFePO_4$, CB, carboxymethyl cellulose (CMC) and a fluorine/acrylate hybrid polymer were thoroughly investigated regarding the influence of the polymeric binders on the flow behavior of the wet slurry as well as on electrical and mechanical properties of corresponding dry layers. Whereas FAHP shows no significant effect on flow behavior, rheological data of wet cathode slurries exhibit a pronounced minimum at a critical CMC concentration, elucidating the adsorption behavior of CMC on particle surface, improving particle dispersion. Accordingly, CMC acts as dispersing and thickening agent depending on polymer concentration, controlling particle network and flow behavior of the slurry. Interestingly, the electrical conductivity of corresponding dry layers exhibits a clear maximum at a critical CMC concentration close to that at which rheological data yields a minimum, indicating optimal particle dispersion and relating the particle network in the slurry to microstructure formation in the corresponding dry layer. Adhesion tests performed on cathodes including CMC as only binder show technically low values irrespective of CMC conentration. However, adhesive strength monotonically increases with increasing FAHP concentration, confirming its role as secondary binder. Even though the increase in adhesion comes at the expense of loss in electrical conductivity, both parameters obtained in this work excel reported values for similar water-based $LiFePO_4$ cathodes using alternative polymeric binders. First reported cohesion values based on compression tests yield a linear increase of cohesive strength with increasing CMC and FAHP concentration. Despite its lower intrinsic mechanical strength, the addition of CMC leads to remarkably higher cohesion values than that corresponding to addition of FAHP. Microstructure investigations revealed a strong effect of CMC on particle alignment at high concentrations, whereas a ran-

dom particle orientation was obtained upon variation of FAHP. Consequently, particle alignment, governed by polymer type and concentration, seem to control the cohesive strength of the cathode.

The effect of CMC concentration, molecular weight M_w and degree of substitution DS on flow behavior of aqueous graphite anode slurries as well as on electrical and mechanical properties of corresponding dry layers was systematically studied. The influence of styrene butadiene rubber (SBR) as secondary binder on these electrode features was additionally addressed. Rheological data were used to discuss the adsorption behavior of CMC on active material particles and the associated particle dispersion at technically relevant concentrations. At constant CMC concentration, the fraction of adsorbed CMC on particle surface increases with increasing M_w and decreasing DS, and correspondingly the amount of dissolved CMC in the solvent decreases as indicated by detailed rheological characterization. In contrast, the addition of SBR does not affect the flow behavior of anode slurries. Whereas DS has a weaker effect on flow behavior and electrical conductivity of corresponding dry layers, conductivity, interestingly, strongly increase with increasing M_w at constant CMC concentration, highlighting the findings of the rheological investigation suggesting lower fractions of randomly distributed polymer at high M_w. As expected, increasing CMC and SBR concentration results in a monotonic decay of electrical conductivity due to the remaining free polymer in the layer, deteriorating conductive pathways. CMC hardly contributes to anode adhesion irrespective of CMC type and concentration, whereas addition of SBR leads to a linear increase of adhesive strength. First cohesion data for water-based graphite anodes was obtained using different well-defined load types to determine critical stress at which electrode structure collapses. Cohesive strength decreases with increasing DS but substantially increases with increasing M_w, even though the intrinsic mechanical strength of CMC is independent of this properties. Microstructure analysis revealed a strong orientation of graphite particles for anodes including CMC with high M_w or low DS. Accordingly, the degree of adsorbed CMC on graphite particles has a strong impact on electrode microstructure and, in turn, on electrical conductivity and mechanical integrity.

In total, this dissertation offers comprehensive and systematic understanding of the role of polymeric binders in water-based electrodes for LIB through a holistic approach, unveiling clear relationships between polymer/particle interactions and resulting electrode properties. New insights into the effect of polymer adsorption and associated particle dispersion on flow behavior of electrode slurries at technically relevant conditions and microstructure formation of corresponding dry layers render clear correlations to electrical conductivity and mechanical integrity of electrodes. This thesis provides the groundwork to fine-tune slurry processing behavior and optimize electrode mechanical properties through targeted polymer choice. Consequently, optimal electrochemical performance and superior mechanical cycle stability of LIB cells might be achieved. Future work taking up this topic should conduct a thorough investigation on the electrochemical behavior to allow for a detailed correlation between electrode properties and cell performance, focusing on the polymer role.

Zusammenfassung

Eines der bestimmenden politischen und wirtschaftlichen Themen des 21. Jahrhunderts ist der Klimawandel und die damit verbundene Forderung nach Klimaschutzstrategien. Zu diesem Zweck hat die Bundesregierung den "Klimaschutzplan 2050" verabschiedet mit dem mittelfristigen Ziel, die Treibhausgasemissionen in Deutschland bis 2030 um mindestens 55% gegenüber 1990 zu reduzieren. Ein Ansatz für eine nachhaltige und globale Transformation der Energieerzeugung und des Energieverbrauchs sowie der Mobilität ist die Umsetzung und Kombination von Elektromobilität mit erneuerbaren Energien. Solar- und Windenergie spielen bei der Stromerzeugung eine größere Rolle und bieten eine Alternative zu fossilen Energieträgern, aber ohne effektive Energiespeicherung werden diese intermittierenden Quellen weiterhin auf kohlenstoffbasierte Energien angewiesen sein. Da die Unmittelbarkeit der Klimakrise immer offensichtlicher wird, sind Batterien der Schlüssel für den Übergang zu einer Welt mit erneuerbaren Energien. Im Jahr 2010 wurden Telefone und Computer mit Batterien betrieben, aber bis zum Ende des Jahrzehnts begannen sie auch Autos und Häuser mit Strom zu versorgen. Lithium-Ionen-Batterien (LIB) sind aufgrund ihrer hohen spezifischen Energie- und Leistungsdichte die vielversprechendste Energiespeichertechnologie für den Einsatz in tragbaren Geräten, Elektrofahrzeugen und im Stromnetz. Trotz der ständig zunehmenden Forschungs- und Entwicklungsaktivitäten im Bereich LIB sind weitere Verbesserungen hinsichtlich ihrer Kapazität, Lebensdauer, Sicherheit und Kosten erforderlich. Darüber hinaus erfordern Umweltbelange eine Verlagerung von Systemen auf der Basis organischer Lösungsmittel hin zu wasserbasierten Alternativen. Daher ist die Entwicklung von hochkapazitiven, sicheren, kostengünstigen und leicht recycelbaren LIB von größter Bedeutung.

Die Forschung hat sich insbesondere auf neue elektrochemisch Aktivmaterialien zur Verbesserung der Batterieleistung konzentriert, wobei elektrochemisch inaktive Elektrodenkomponenten, wie z.B. polymere Bindemittel, als sekundärer Nebenaspekt berücksichtigt werden.Polymere können jedoch das Fließverhalten von nassen Elektrodenpasten und damit das Verarbeitungsverhalten bei der Elektrodenherstellung stark beeinflussen. Die Wechselwirkung zwischen Polymeren und aktiven Partikeln sowie die Verdickungswirkung von Polymeren im Lösungsmittel beeinflussen nicht nur die rheologischen Eigenschaften von Elektrodenpasten, sondern auch die Partikeldispersion und die Elektrodenmikrostruktur entsprechender Trockenschichten. Daher bestimmt die resultierende Komponentenverteilung in der Trockenelektrode die Bildung eines leitfähigen Partikelnetzwerks, das für die Erzielung einer optimalen Ionen- und Elektronentransportkinetik entscheidend sein kann, was wiederum das Ratenvermögen sowie die Zellenergie und Leistungsdichte verbessert. Darüber hinaus gewährleisten polymere Bindemittel die mechanische Stabilität der Elektrode während der Lade-/Entladezyklen der Zelle, wodurch die lokale Delaminierung der Elektrodenschicht vom Stromableiter sowie Risse innerhalb der Schicht, die durch Volumenschwankungen des elektrochemisch Aktivmaterials induziert werden, gemildert werden. Somit garantiert eine ausreichende Kohäsions- und Haftfestigkeit, die durch das Bindemittel bereitgestellt wird, die Zyklusstabilität

und eine verlängerte Lebensdauer der Zelle. Trotz dieses grundlegenden Wissens über die Rolle von polymeren Bindemitteln erfordert der letztendliche Beitrag des Bindemittels zur Batterieleistung und seine komplexen Wechselwirkungen mit dem Aktivmaterial immer noch Verständnis.

Diese Arbeit konzentriert sich auf die Rolle von polymeren Bindemitteln in wasserbasierten Elektroden für LIB. Der ganzheitliche Ansatz unterstreicht die Bedeutung des Bindemittels von seiner Wechselwirkung mit Aktivmaterialien, die das Fließverhalten der nassen Pasten und den daraus resultierenden Dispersionszustand der Komponenten in der trockenen Schicht steuern, bis hin zu seiner Wirkung auf die elektrische Leitfähigkeit, die mechanische Integrität und die Mikrostruktur der Elektrode, die für das Verständnis des wahren Beitrags von polymeren Bindemitteln zur Zellleistung unerlässlich sind. Im Hinblick auf das optimale Verarbeitungsverhalten der Elektrodenpasten während der gesamten Elektrodenherstellung, insbesondere während der Misch-, Pump- und Beschichtungsschritte, sind eine homogene Partikeldispersion und die Stabilität der Aufschlämmung gegen Partikelablagerung von wesentlicher Bedeutung. Als Alternative zu optischen Techniken werden zwei verschiedene Methoden zur Charakterisierung des Sedimentationsprozesses von $LiFePO_4$- und Rußpartikeln (CB) in opaken Suspensionen, die für LIB verwendet werden, vorgestellt. Die nicht-invasive Spin-Echo-basierte Magnetresonanztomographie bietet neue Einblicke in die Partikelsedimentation und zeigt die räumliche Verteilung der Partikel und der entsprechenden Agglomerate sowie die Form der Absetzfront auf. Trotz reproduzierbarer und zuverlässiger Ergebnisse aus dieser Methode können niederviskose Suspensionen sowie hohe Partikelmassenanteile zu Messsignaleinschränkungen führen, die die Bildschärfe und Datenanalyse erschweren. Daher wurden ergänzende gravimetrische Experimente mit einer selbstgefertigten Sedimentationswaage durchgeführt, um das Absetzen der Partikel bei hohen, technisch relevanten Konzentrationen zu untersuchen. Diese Technik ermöglicht die Charakterisierung des Sedimentationsverhaltens von hochkonzentrierten, wasserbasierten Elektrodenaufschlämmungen einschließlich $LiFePO_4$, CB und polymeren Bindemitteln, was zu schlüssigen Ergebnissen führt. Dementsprechend stellen die vorgestellten Methoden eine zuverlässige Kombination zur Charakterisierung des Sedimentationsverhaltens von opaken Suspensionen mit unterschiedlicher Partikelbeladung für LIB dar.

Wässrige Kathoden einschließlich $LiFePO_4$, CB, Carboxymethylcellulose (CMC) und ein Fluor/Acrylat-Hybridpolymer wurden hinsichtlich des Einflusses der polymeren Bindemittel auf das Fließverhalten der nassen Paste sowie auf die elektrischen und mechanischen Eigenschaften entsprechender Trockenschichten eingehend untersucht. Während FAHP keinen signifikanten Einfluss auf das Fließverhalten zeigt, zeigen die rheologischen Daten der Kathodenpasten bei einer kritischen CMC-Konzentration ein ausgeprägtes Minimum, das das Adsorptionsverhalten von CMC an der Partikeloberfläche aufklärt. Dementsprechend wirkt CMC in Abhängigkeit von der Polymerkonzentration als Dispergier- und Verdickungsmittel und steuert das Partikelnetzwerk und das Fließverhalten der Paste. Interessanterweise zeigt die elektrische Leitfähigkeit entsprechender Trockenschichten ein deutliches Maximum bei einer kritischen CMC-Konzentration nahe

der Konzentration, bei der die rheologischen Daten ein Minimum ergeben, was auf eine optimale Partikeldispersion hinweist und das Partikelnetzwerk in der Paste mit der Mikrostrukturbildung in der entsprechenden Trockenschicht in Beziehung setzt. Adhäsionsprüfungen an Kathoden, die CMC als einziges Bindemittel enthalten, zeigen technisch niedrige Werte unabhängig von der CMC-Konzentration. Die Haftfestigkeit nimmt jedoch mit zunehmender FAHP-Konzentration monoton zu, was ihre Rolle als sekundäres Bindemittel bestätigt. Auch wenn die Zunahme der Adhäsion auf Kosten des Verlustes der elektrischen Leitfähigkeit geht, übertreffen beide in dieser Arbeit erhaltenen Parameter die berichteten Werte für ähnliche wasserbasierte $LiFePO_4$-Kathoden, die alternative polymere Bindemittel verwenden. Erste berichtete Kohäsionswerte, die auf Druckversuchen basieren, ergeben eine lineare Zunahme der Kohäsionsfestigkeit mit zunehmender CMC- und FAHP-Konzentration. Trotz der geringeren intrinsischen mechanischen Festigkeit führt die Zugabe von CMC zu bemerkenswert höheren Kohäsionswerten als die, die der Zugabe von FAHP entsprechen. Mikrostrukturelle Untersuchungen zeigten einen starken Einfluss von CMC auf die Partikelausrichtung bei hohen Konzentrationen, während bei Variation von FAHP eine zufällige Partikelorientierung erzielt wurde. Folglich scheint die Partikelausrichtung, die vom Polymertyp und der Konzentration abhängt, die Kohäsionsfestigkeit der Kathode zu steuern.

Der Einfluss von CMC-Konzentration, Molekulargewicht M_w und Substitutionsgrad DS auf das Fließverhalten von wässrigen Graphitanodenpasten sowie auf die elektrischen und mechanischen Eigenschaften entsprechender Trockenschichten wurde systematisch untersucht. Der Einfluss von Styrol-Butadien-Kautschuk (SBR) als sekundäres Bindemittel auf diese Elektrodeneigenschaften wurde zusätzlich untersucht. Bei konstanter CMC-Konzentration nimmt der Anteil der adsorbierten CMC an der Partikeloberfläche mit zunehmendem M_w und abnehmendem DS zu, wodurch die Menge der im Lösungsmittel gelösten CMC abnimmt, wie aus der detaillierten rheologische Charakterisierung hervorgeht. Im Gegensatz dazu hat die Zugabe von SBR keinen Einfluss auf das Fließverhalten von Anodenpasten. Während DS keinen signifikanten Einfluss auf das Fließverhalten und die elektrische Leitfähigkeit der entsprechenden trockenen Schichten hat, steigt die Leitfähigkeit interessanterweise mit zunehmendem M_w bei konstanter CMC-Konzentration stark an, was die Ergebnisse der rheologischen Untersuchung unterstützt, die auf geringere Anteile von zufällig verteiltem Polymer bei hohem M_w hindeuten. Wie erwartet, führt eine zunehmende CMC- und SBR-Konzentration zu einem monotonen Zerfall der elektrischen Leitfähigkeit aufgrund des verbleibenden freien Polymers in der Schicht, wodurch sich die Leiterbahnen verschlechtern. CMC trägt unabhängig von CMC-Typ und Konzentration kaum zur Anodenhaftung bei, während die Zugabe von SBR zu einem linearen Anstieg der Haftfestigkeit führt. Erste Kohäsionsdaten für Graphitanoden auf Wasserbasis wurden unter Verwendung verschiedener Belastungstypen erhalten, um die kritische Spannung zu bestimmen, bei der die Elektrodenstruktur zusammenbricht. Die Kohäsionsfestigkeit nimmt mit zunehmendem DS ab, nimmt aber mit zunehmendem M_w wesentlich zu, obwohl die intrinsische mechanische Festigkeit der CMC unabhängig von diesen Eigenschaften ist. Die Mikrostrukturanalyse ergab eine starke Orientierung der Graphitteilchen für Anoden einschließlich CMC mit

hohem M_w oder niedrigem DS. Dementsprechend hat der Grad der adsorbierten CMC auf Graphitpartikeln einen starken Einfluss auf die Mikrostruktur der Elektrode und damit auf die mechanische Integrität.

Insgesamt bietet diese Dissertation ein umfassendes und systematisches Verständnis der Rolle von polymeren Bindemitteln in wasserbasierten Elektroden für LIB und enthüllt klare Beziehungen zwischen Polymer/Partikel-Wechselwirkungen und den daraus resultierenden Elektrodeneigenschaften. Neue Erkenntnisse über den Einfluss der Polymeradsorption und der damit verbundenen Partikeldispersion auf das Fließverhalten von Elektrodenpasten und die Mikrostrukturbildung entsprechender trockener Schichten machen klare Zusammenhänge zur elektrischen Leitfähigkeit und mechanischen Integrität von Elektroden deutlich. Diese Arbeit liefert die Grundlagen zur Feinabstimmung des Pastenverhaltens und zur Optimierung der mechanischen Elektrodeneigenschaften durch gezielte Polymerauswahl. Folglich könnten eine optimale elektrochemische Leistung und eine überlegene mechanische Zyklusstabilität der LIB-Zellen erreicht werden. Zukünftige Arbeiten, die dieses Thema aufgreifen, sollten eine gründliche Untersuchung des elektrochemischen Verhaltens durchführen, um eine detaillierte Korrelation zwischen Elektrodeneigenschaften und Zellleistung zu ermöglichen, wobei der Schwerpunkt auf der Rolle des Polymers liegen sollte.

Notations

Abbreviations

CB	Carbon black
CCCV	Constant current - constant voltage
CMC	Carboxymethyl cellulose
C-rate	Current rate
DOD	Depth of discharge
DS	Degree of substitution
EDX	Energy-dispersive x-ray spectroscopy
EV	Electric vehicle
FAHP	Fluorine/acrylate hybrid polymer
FOV	Field of view
HEV	Hybrid electric vehicle
ICP-OES	Inductively coupled plasma optical emission spectrometry
Li	Lithium
$Li_4Ti_5O_{12}$ (LTO)	Spinel lithium-titanate oxide
LIB	Lithium-ion battery
$LiCoO_2$ (LCO)	Lithium-cobalt oxide
$LiFePO_4$ (LFP)	Lithium-iron phosphate
$LiMn_2O_4$ (LMO)	Spinel lithium-manganese oxide
$LiMnO_2$	Lithium-manganese oxide
$LiNiO_2$ (LNO)	Lithium-nickel oxide
M_w	Molecular weight
MRI	Magnetic resonance imaging
NMP	N-methyl-2-pyrrolidone
NMR	Nuclear magnetic resonance
PAA	Polyacrylic acid
PDMS	Poly-dimethylsiloxane
PE	Polyethylene
PHEV	Plug-in hybrid electric vehicle
PS	Polystyrene
PSD	Particle size distribution
PSSA	4-styrene sulfonic acid
PTFE	Poly(tetrafluoroethylene)
PVAc	Polyvinyl acetate
PVDF	Polyvinylidene difluoride
RARE	Rapid acquisition with relaxation enhancement
ROI	Region of interest
SBR	Styrene butadiene rubber
SEI	Solid electrolyte interphase
SEM	Scanning electron microscopy

SF	Settling front
Si	Silicon
SOC	State of charge
SSA	Specific surface area
UCV	Cut-off voltage
VdW	Van der Waals
XPS	X-ray photoelectron spectroscopy

Latin symbols

x_g	Boltzmann constant	[JK^{-1}]
Q_3	Cumulated particle size distribution	[%]
x_g	Distance to particle surface	[nm]
e	Elementary charge	[C]
R_g	Gyration radius	[nm]
A_H	Hamaker constant	[J]
a	Interparticle distance	[nm]
n_i	Ion concentration	[$moll^{-1}$]
z_i	Ion valence	[-]
L	Length of polymer layer	[nm]
V_{liquid}	Liquid volume	[ml]
G"	Loss modulus	[Pa]
r	Particle radius	[nm]
q_3	Particle size density	[μm^{-1}]
w_i	Settled mass fraction	[%]
V_{solid}	Solid volume	[ml]
S_A	Specific surface area	[m^2g^{-1}]
G'	Storage modulus Storage modulus	[Pa]
T	Temperature	[K]
$x_{50,3}$	Volume-based average diameter	[nm]

Greek symbols

ϕ_{CMC}	CMC volume fraction	[vol %]
k^{-1}	Debye length	[nm^{-1}]
ρ	Density	[gcm^{-3}]
ϵ_r	Dielectric constant	[-]
ϕ_{eff}	Effective volume fraction	[vol %]
Σ	Electrical conductivity	[Scm^{-1}]
Ψ	Electrostatic interparticle potential	[mV]
ϕ_{FAHP}	FAHP volume fraction	[vol %]
η_∞	High shear limiting viscosity	[Pas^{-1}]
ν	Kinematic viscosity	[mm^2s^{-1}]

$\sigma_{\mathrm{c,max}}$	Maximum compressive strength	[Nmm^{-2}]
$\sigma_{\mathrm{b,max}}$	Maximum flexural strength	[Nmm^{-2}]
$\sigma_{\mathrm{t,max}}$	Maximum tensile strength	[Nmm^{-2}]
$\sigma_{\mathrm{tor,max}}$	Maximum torsional strength	[Nmm^{-2}]
ϵ_0	Permitivity of free space	[Fm^{-1}]
ϵ	Porosity	[-]
ϕ_{SBR}	SBR volume fraction	[vol %]
$\dot{\gamma}$	Shear rate	[s^{-1}]
τ	Shear stress	[Pa]
ϕ_{m}	Solid particle mass fraction	[wt %]
ϕ_{p}	Solid particle volume fraction	[vol %]
η_{s}	Solvent viscosity	[Pas^{-1}]
Ψ_0	Surface potential	[mV]
$\eta_{\mathrm{rel},\infty}$	Relative high shear viscosity	[-]
η_{rel}	Relative viscosity	[-]
$\eta_{\mathrm{r},0}$	Relative zero shear viscosity	[-]
Ψ_{VdW}	Van der Waals force	[N]
η	Viscosity	[Pas^{-1}]
τ_{y}	Yield stress	[Pa]

Contents

1 General introduction

The world energy consumption has been steadily increasing since the industrial revolution, making fossil fuels the most widely used energy source. As a result, huge carbon dioxide emissions are causing irreversible damage to the environment with potentially disastrous consequences to mankind. Hence, a legally binding global climate change agreement was adopted at the Paris climate conference (COP21) on December 2015. As a historic landmark, the Paris agreement aims to keep the increase in global average temperature to well below 2°C above pre-industrial levels and to limit the increase even further to 1.5°C. This attempt to accelerate and intensify the actions and investments needed for a sustainable low carbon future set in motion the pursue to increment the development and application of renewable energy sources.

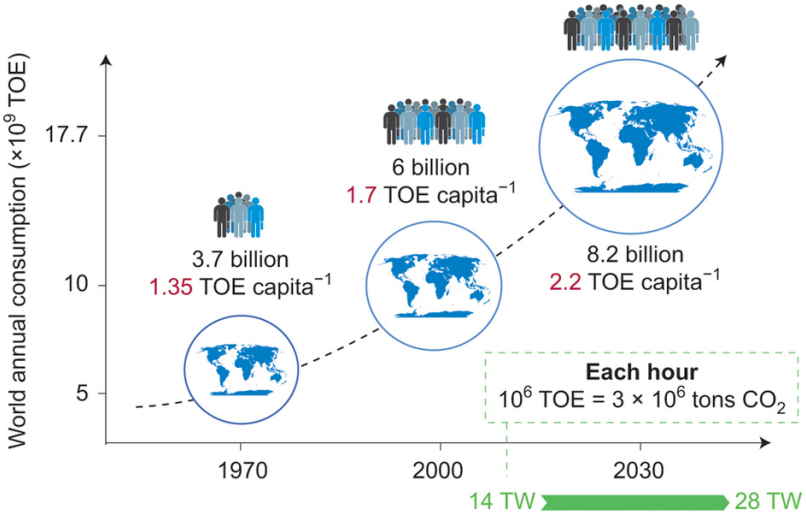

Figure 1.1: Past, present and forecast of the world's energy needs up to 2050. With the changing lifestyles of an increasing number of inhabitants, our energy rate demand will double from 14 TW (2010) to 28 TW (2050). TOE = ton of oil equivalent. Map: © Macmillan Mexico/Haide Ortiz Ortiz, Mario Enrique Ramírez Ruiz [1].

In addition, the availability of non-renewable energy sources nears an end as the world population continuous to grow. Therefore, a transition from depleting energy sources to renewables, such as biomass, wind, solar and tidal, is crucial to keep up with the ceaseless worldwide energy demand as depicted in Figure 1.1. However, these alternative sources are inherently fluctuating and generally isolated relative to established fossil fuel power plants supplying the majority of electrical energy. To maximize the use of renewable energy sources and ensure power network stability and reliability, efficient and sustainable energy storage is of utmost importance. The diverse field of applications for energy storage technologies still lacks the optimal candidate able to fulfill every purpose simultaneously. Lithium-ion batteries (LIB) are currently considered the most suitable technology for short- and mid-term energy storage as well as for transportation

due to their high energy and power density [2–5]. Thus, inclusive of their potential use in stationary grid storage, LIB are nowadays the dominant power supply for portable electronic devices and the technology of choice for replacing the fossil-fuel-based modern transportation technologies. To achieve a widespread commercialization of hybrid electric vehicles (HEVs), plug-in hybrid electric vehicles (PHEVs), and full electric vehicles (EVs), however, LIB costs must still be reduced to less than $100 per kWh to achieve a fast market penetration. Moreover, it is of common agreement that further improvements are required regarding their specific energy and power, safety and lifetime, in addition to the general concern about the foreseen shortage of chemical raw materials as well as efficient battery recycling. Thus, the development of high capacity, safe, cheap and easily recyclable LIB have become an urgent demand.

At the end of 2019, the electric battery sector witnessed a breakthrough as the European Commission approved 3.2 billion euros of state aid from seven countries including Germany for research, development and production of battery technologies. This initiative will unlock around 5 billion euros private investment, rounding its total sum to about 9 billion euros to support innovative technologies from mining and processing the raw material to production and recycling of the LIB. This ambitious project aims to accomplish the EU plan to become the first climate-neutral continent by 2050. Consequently, the industrial sector but also the scientific community are urged to strengthen their research and development activities and deliver beyond state-of-the-art innovation across the battery value chain to achieve sustainable technologies for LIB that last longer, have shorter charging times, are safer and more environmentally friendly than those currently available.

2 State of the art

This section offers a brief overview on the necessary theoretical foundations of this work. First, interactions between solid particles dispersed in a liquid phase are assessed. The effect of polymer addition to these dispersed systems is discussed, focusing on the adsorption of polymer chains on solid particles surface and its contribution to particle distribution. These complex, multi-phase systems find application in a wide variety of technologies such as electrode slurries for LIB. Considering the topic of this work, the understanding of the principles governing particle/polymer interaction and polymer adsorption is, at this point, essential for the interpretation of the discussed results. The fundamentals required to understand the composition, manufacture and operation of these energy storage systems are presented here.

2.1 Particle interaction and suspension stability

Heterogeneous mixtures of at least two immiscible substances are called dispersions. A distinction is mainly made between emulsions, suspensions and foams. In these systems the disperse phase is finely distributed in the surrounding continuous phase. In the case of emulsions, both the disperse and the continuous phase are present as mutually insoluble liquids. In suspensions, on the other hand, solid particles are well dispersed in a liquid main phase. The flow behavior of dispersions is largely determined by the properties of the disperse phase. In the case of suspensions, these are the solid volume fraction, the mean particle size, the particle size distribution (at high particle loading), the particle shape and, noting its minor relevance, the surface roughness of the particles [6]. The solid volume fraction is defined as:

$$\phi_p = \frac{V_{solid}}{V_{solid} + V_{liquid}} \tag{2.1}$$

where V_{solid} and V_{liquid} define the solid and liquid phase volume, respectively. Suspensions are usually not stable from a thermodynamic point of view, which is why without stabilization of the dispersion separation of continuous and disperse phase may occur. Suspensions including solid particles with a particle size between 1 nm and 10 μm are known as colloidal suspensions [7]. At this particle size, thermal fluctuations lead to collisions between particles and solvent molecules termed as Brownian motion. In addition, stability and flow are determined by hydrodynamic as well as attractive and repulsive thermodynamic forces acting on the particles. Particle collisions may result in agglomeration when inter-particle attractive forces are stronger than repulsive ones. As a result, large agglomerates may sediment due to the gravitational force, functionally destabilizing the colloidal suspension.

2.1.1 Particle-particle interaction

Van der Waals (VdW) forces and depletion interactions belong to the interparticle attractive interaction, whereas electrostatic and steric interactions are associated to a repulsive

behavior. VdW forces are generated by dipole-dipole interactions. These interactions can occur between two dipoles, between a dipole and an induced dipole or two induced dipoles. When colloidal particles approach each other, they are pulled together by the VdW interaction, thus forming agglomerates. The attraction between two particles can be described by the sum of all intermolecular interactions [8]. The VdW force between two equally large particles with radius r and a very small distance a between the surfaces ($a << 2r$) can be calculated as:

$$\Psi_{VdW} = -\frac{A_H r}{12a} \tag{2.2}$$

where A_H is the material dependent Hamaker constant.

The addition of a flexible polymer, which does not adsorb on the particle surface, results in a so-called depletion layer around the particles. The depletion zone is not accessible for the centers of gravity of the polymer coils in the continuous phase. The polymer concentration in this zone is lower than that in the rest of the continuous phase, resulting in a lower osmotic pressure. When these layers overlap a larger volume for the polymers is accessible to diffuse, decreasing the free energy of the polymers and inducing an interparticle attractive effect [9]. The range of the depletion interaction depends on the polymer size, i.e. its gyration radius R_g. The strength of the interaction depends on the osmotic pressure and thus on the polymer concentration.

Colloids dispersed in an aqueous medium exhibit a surface charge as a consequence of ion formation or ion adsorption. The range of this electrostatic interaction depends on the surface charge and the concentration of dissolved ions in the dispersion, as well as the valence of the ions. Co- and counter-ions form a double-layer around the particle. The overlap of two double-layers result in a repulsive interparticle potential [10]. This potential results from the linearization of the Poisson-Boltzmann-equation and is represented by the Debye-Hückel approximation for a sphere:

$$\Psi = \Psi_0 \frac{r}{h} \exp\left(-k(h-r)\right) \tag{2.3}$$

where Ψ_0 is the surface potential, k^{-1} is the Debye-length and h is the distance between the center of gravity of two particles. The range of the potential in a solution with ions is characterized by the Debye-length.

$$k^{-1} = \sqrt{\frac{\epsilon_0 \epsilon_r k_B T}{e^2 \sum n_i z_i^2}} \tag{2.4}$$

Where ϵ_0 is the permittivity of free space, ϵ_r is the dielectric constant, k_B is the Boltzmann constant, T is the temperature, e is the elementary charge, n_i is the ion concentration and z_i is the ion valence.

2.1.2 Polymer adsorption / particle-additive interaction

Alternative ways to stabilize colloidal suspensions include adding polymers that dissolve in the liquid phase, thus acting as rheology modifiers. Polymers dissolved in the continuous phase are able to interact with solid surfaces and adsorbe at the solid interface to the liquid phase. This phenomenon may result in attractive or repulsive interparticle interaction depending on the solubility of the polymer in the liquid phase. Polymer adsorption takes place at low solvent quality due to the higher affinity of the polymer to the solid surface, resulting from the strong repulsion between solvent and polymer molecules. The polymer chains may be adsorbed or chemically bound to the particle surface, forming a polymer layer of length L around the solid particle. This polymer layer adds to the effective particle radius, hence increasing the effective volume fraction of the suspension [10].

$$\phi_{eff} = \phi_p \left(1 + \frac{L}{r}\right)^3 \tag{2.5}$$

The length of the polymer chain must extend further than the distance at which the strength of the VdW interactions exceeds k_BT in order to ensure an interparticle repulsive effect. As two colloidal particles with adsorbed polymer on the surface approach each other the local osmotic pressure increases significantly due to the increased polymer concentration in the overlap region, resulting in a repulsive force as shown in Figure 2.1.

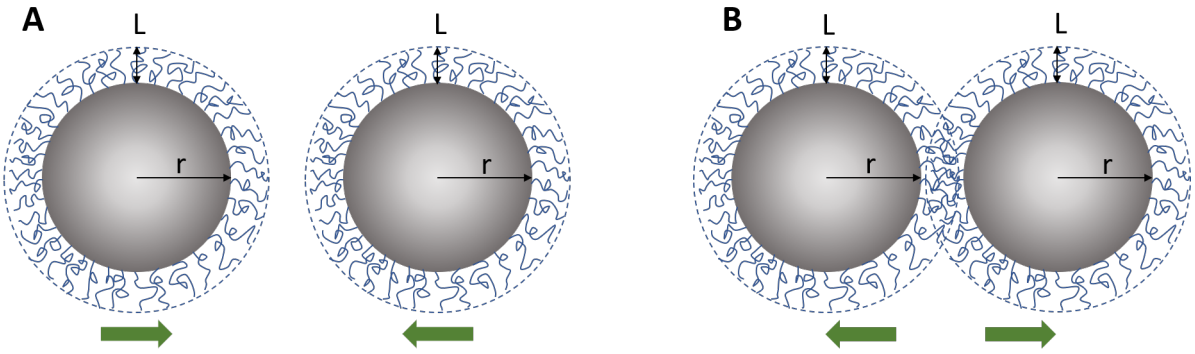

Figure 2.1: Schematic illustration of (A) approaching particles with adsorbed polymer on the surface and (B) repulsive interaction effect of polymer-coated particles with overlapped polymer layers. L is the polymer layer length and r is the particle radius.

Several factors play a decisive role regarding the solvent quality and the polymer affinity to solid surfaces:

- Molecular polymer structure, particularly hydrophilic and hydrophobic groups
- Hydrophobicity or hydrophilicity of the solid surface
- Charge of the solid surface

- Solvent polarity

Polymers often exhibit differently hydrophilic areas, especially if they are structured as block copolymers. Therefore, these molecules adopt different conformations at the interface, depending on their molecular structure. It should be noted that for adsorption to occur, the chain segments should have a minimum adsorption energy at the interface. Chain segments with high affinity to the surface provide a strong adsorption, whereas segments with low affinity (non-adsorbing) are highly solvated by the medium, ensuring steric stability. These configurations represent the most common and favorable structures for stabilizing colloidal suspensions, showing a sequence of loops, trains and tails, as illustrated in Figure 2.2 [11].

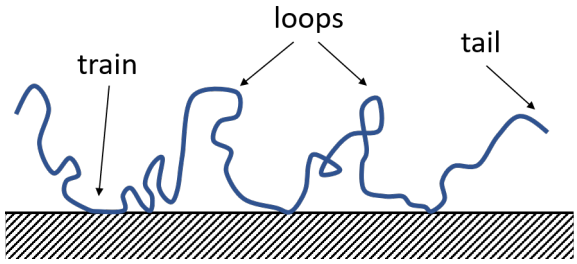

Figure 2.2: Schematic illustration of a polymer chain adsorbed on a solid particle surface.

The desorption of adsorbed polymer chains on particle surfaces is thermodynamically strongly inhibited due to the attachment of different segments at the interface. Hence, desorption of the polymer chain can often only be achieved by changing the polymer/solvent solubility or by adding a better adsorbing molecule [12]. The former can be influenced through temperature change, pH-value or adding ions. For polydisperse polymer fractions and polymers with different molecular weight, larger molecules adsorb preferentially over smaller ones. At low polymer concentration, polymers with practically all molecular weight adsorb to the particle surface. Higher molecular weight fractions displace the lower ones at the surface with increasing polymer concentration, releasing them in solution. The addition of a second substance, which has a higher affinity to the solid surface, leads to a competition between the two molecules for surface area to adsorb onto. This competitive behavior may shift the distribution of adsorbed and dissolved polymer in the suspension [13].

2.2 Fundamentals of lithium-ion batteries

Lithium-ion batteries are a type of rechargeable battery, which does not contain lithium metal, but only charged Li^+-ions. They consist of two electrodes, anode and cathode, a porous membrane also known as separator, hindering direct contact between the electrodes, and an electrolyte, which serves as a transport medium for Li-ions and does not participate in the chemical reaction (see Figure 2.3).

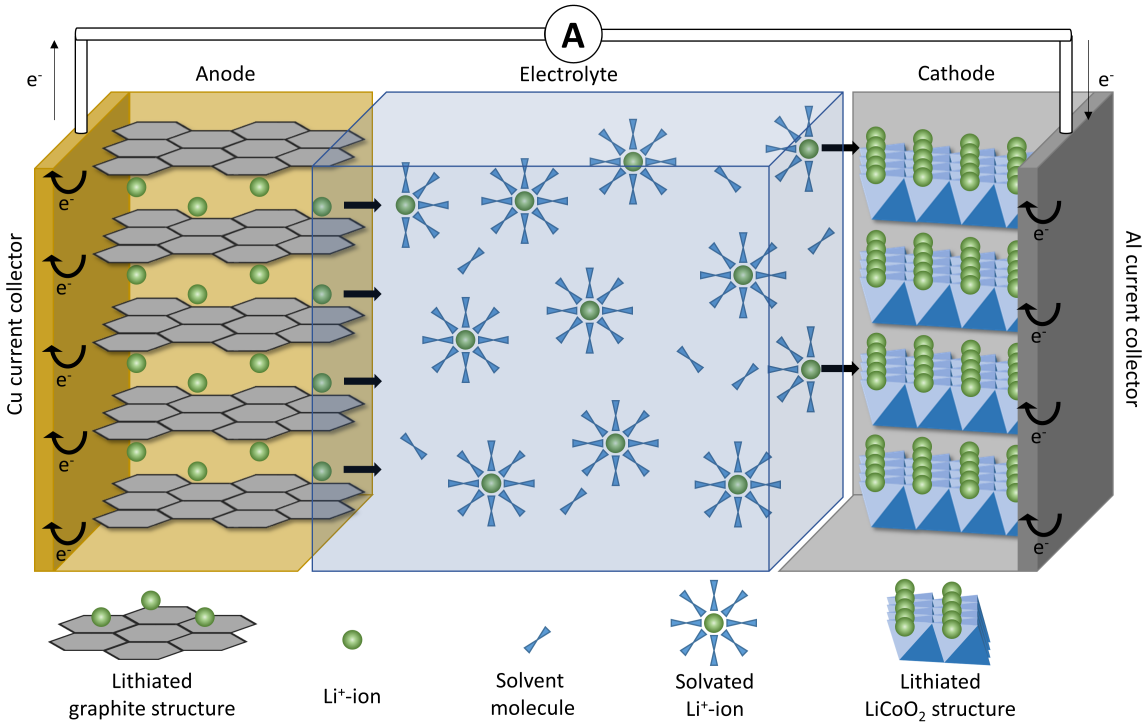

Figure 2.3: Schematic illustration of a Li-ion cell. Adapted from [2].

During charging, an external electrical power source induces the migration of Li-ions across the electrolyte from the cathode to the anode as electrons travel through a current conductor to the anode. Li-ions dissociate from the anode during discharging and diffuse through the separator to the cathode, whereas electrons travel back to the cathode, thereby keeping the electrode neutral. This reversible removal of lithium ions is referred to as lithium-ion intercalation and describes the insertion and extraction into the crystalline lattice of the host electrode without changing its crystal structure. The conversion from chemical to electrical energy occurs through a reduction-oxidation (redox) reaction as exemplary described in Table 2.1 for $LiFePO_4$ and graphite as electrochemically active material.

Table 2.1: Extraction and insertion of Li-ions during charge/discharge of a Li-ion cell using graphite and $LiFePO_4$ as active material.

	Anode	Cathode
Charge	$C_6 + xLi^+ + xe^- \rightarrow Li_xC_6$	$LiFePO_4$ - xLi^+ - $xe^- \rightarrow xFePO_4 + Li_{1-x}FePO_4$
Discharge	Li_xC_6 - xLi^+ - $xe^- \rightarrow C_6$	$FePO_4 + xLi^+ + xe^- \rightarrow xLiFePO_4 + (1-x)FePO_4$

The redox reactions take place in the host lattice of the respective electrode, which releases or accepts the electrons. It must be noted that the lithium is never present in metallic form, i.e. the Li-ions are never oxidized or reduced. The lithium transport consists of several steps. In case of cell discharge, lithium atoms are first removed from

the anode as a result of a concentration difference. This solid state diffusion is slow and is strongly controlled by the lattice structure of the anode material. Lattice defects can easily hinder the ion transport, whereas multidimensional structures enhance ion transport kinetics due to the multidimensional diffusion channels. Li-ions are removed from the anode surface by releasing an electron. Subsequently, the positively charged ions are solvated in the liquid electrolyte. The organic molecules protect the charged ions and facilitate their transport through the separator and electrolyte. Finally, the Li-ions remove their solvate shell at contact with the cathode interface and are inserted in the host lattice, taking up an electron. This process is also associated with a charge transfer and is controlled by a diffusion process defined by the structure of the cathode material.

The electrodes, anode and cathode, are essential components of the Li-ion cell, which in turn consist of further components. Electrodes consist of metallic current collectors coated with a porous particulate layer. In addition to the electrochemically active material, these layers contain, additives as a conductivity enhancer and polymers as binder. In the electrode fabrication process, these components are dissolved/dispersed in a solvent to prepare the electrode slurry, which is then coated or printed onto the current collector and dried. Due to the different components, Li-ion electrodes are also referred to as composite layers. The active materials and additives used for electrode fabrication as well as the selected parameters of the electrode layer significantly determine the properties of the Li-ion cell. The following section briefly discusses critical selection parameters regarding the composition and target parameters of electrodes and corresponding cells.

2.2.1 Electrode and cell design

A vast variety of active materials can be used for the fabrication of Li-ion electrodes. These materials differ in their crystal structure, affecting ion insertion. Additionally, they exhibit different potentials at which they store Li-ions. Since the open-circuit voltage of a cell depends on the combination of electrode materials used, the choice of electrode materials is decisive for the cell voltage. In order to achieve good cell performance the electrochemically active materials of the electrode should meet the following criteria [14, 15]:

- High volumetric lithium storage capacity (specific capacity) in the lattice structure
- Low volume change during de- and intercalation of Li-ions
- High electrical and ionic conductivity
- High electrochemical potential between electrode materials
- Operational safety and stability of the individual components
- High cycle stability, i.e. long cycle lifetime

Although the choice of electrochemically active materials is of utmost importance, electrochemically inactive materials play a decisive role in electrode performance. Electron conductive metal foils are used as current collectors, connecting the composite layer to the external electrical conductor. They must ensure good mechanical stability and adhesion to the electrode layer. In addition, they must show chemical stability at the required electrode potential, i.e. there is no reaction with lithium or the electrolyte components. Commonly, aluminum foils are used for the cathodes, whereas anodes are fabricated using copper foils. The electron transport through the electrode layer can be enhanced adding particulate conductive additives. Nanoscale carbon black particles (CB) or carbon nanotubes create a conductive network throughout the electrode layer, improving electron transport kinetics. Further, polymers are added to ensure the mechanical integrity of the electrode and adhesion between current collector and electrode layer.

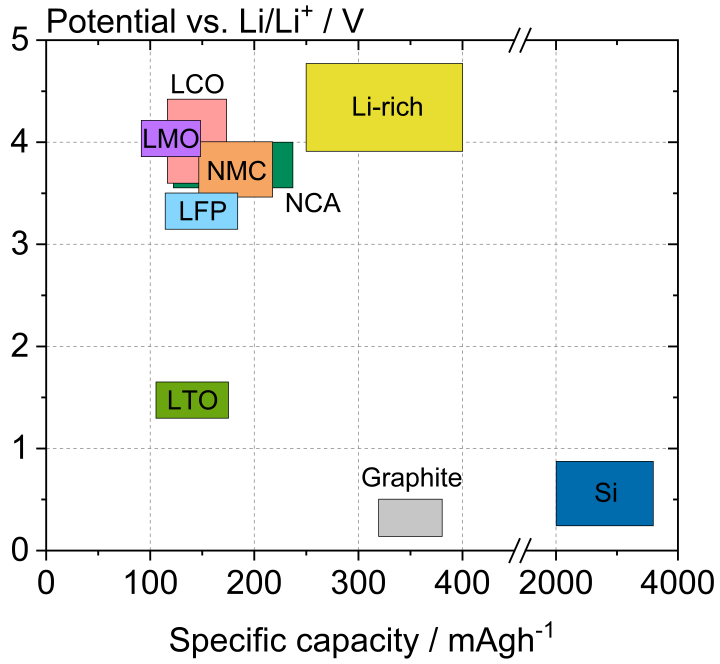

Figure 2.4: Approximate range of average discharge potential relative to Li metal over specific capacity of common electrode materials: Silicon (Si), lithium-titanate oxide (LTO), lithium-iron phosphate (LFP), lithium-nickel-manganese-cobalt oxide (NMC), lithium-manganese oxide (LMO), lithium-nickel-cobalt-aluminum oxide (NCA) and lithium-cobalt oxide (LCO). Adapted from [16–18].

The capacity of a cell depends mainly on the selected electrode materials. In this context, the parameters specific energy ($Whkg^{-1}$) and energy density (Whl^{-1}) are decisive. In order to achieve high values, the electrodes must have high specific capacities ($Ahkg^{-1}$) and capacity densities (Ahl^{-1}) as well as the greatest possible potential difference between them. The specific power (Wkg^{-1}) or power density (Wl^{-1}) is determined

by the current intensity and the corresponding cell voltage. Figure 2.4 shows the approximate range of average potential relative to Li metal over the specific capacity of common electrode active materials. Proper selection of the active material and battery design is critical to meeting both the energy and power performance required for different battery applications. Depending on the target application, batteries can be categorized into energy and power cells. Energy cells are characterized by their high capacity to store energy, i.e. high specific energies. They are used in grid applications combined with renewable energy sources as well as in electromobility, especially for large operation ranges. Power cells, on the other hand, must be able to deliver and take on energy at faster rates, thus yielding higher specific power. These cells are particularly suitable for use in hybrid vehicles as well as in fast charging applications, providing and adsorbing high currents at high peak phases. Usually, high-energy cells are found at low power densities, whereas power cells have a low energy density. However, cell specific properties can be optimized through targeted cell design. In case of high-energy cells, active materials with high specific capacity and thick electrode layers with high porosity are favorable. In contrast, high-power cells are related with high ionic and electrical conductivity active materials as well as thin electrode layers with low porosity.

2.2.2 Active material and conductivity additive

As discussed above, inherent characteristics of active materials are critical to the electrochemical performance of Li-ion battery electrodes. In the following, typical and frequently used materials for electrode production are briefly introduced, whereby the focus of this work is on aqueous, lithium-iron phosphate ($LiFePO_4$)-based cathodes and graphite-based anodes.

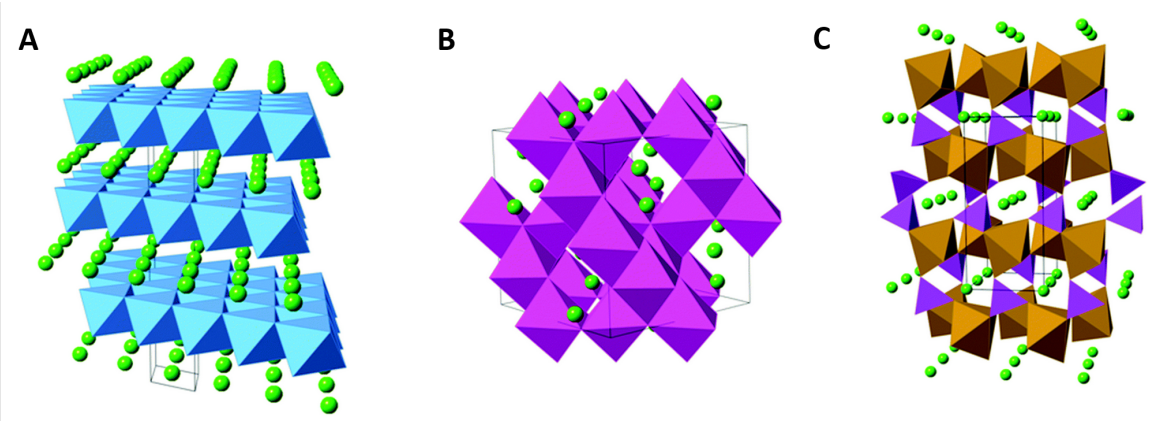

Figure 2.5: Schematic crystal structure of representative cathode materials: (A) layered α-$LiCoO_2$, (B) cubic $LiMn_2O_4$ spinel and (C) olivine $LiFePO_4$. Green dots represent Li-ions. Edited from [19] - Published by The Royal Society of Chemistry.

Multiple lithium metal oxides and phosphates can be generally used as cathode materials. In addition to the potential difference over elemental lithium, the crystal structure,

thermal and chemical stability, price and availability play a major role in the selection of a suitable material. Furthermore, the cathode material should have a high reversibility and low volume change during the intercalation of lithium-ions. Regarding the crystal structure, olivine (1D), layered (2D) and spinel structures (3D) can be distinguished as shown in Figure 2.5 [20, 21]. In contrast to most of cathode materials, $LiFePO_4$ is a metal-phosphate and crystallizes in an olivine structure, providing 1-dimensional transport paths through the crystal structure for Li-ions [22]. This material shows a theoretical capacity of 170 $mAhg^{-1}$, which can be nearly fully exploited in practice. However, the average electrode potential is only 3.4 V vs. Li, reducing the achievable energy density of the cell. Thermal stability of the crystal structure and the associated safety and slow degradation as well as cycle stability of the material even at high currents represent some key advantages of $LiFePO_4$. In addition, low cost and toxicity as well as good environmental compatibility make this material suitable for large cell applications [23–27]. Nevertheless, its poor electric conductivity (10^{-9} Scm^{-1}) and a low Li^+-ion diffusion coefficient ($1.8x10^{-18}$ m^2s^{-1}) at room temperature constitute critical intrinsic drawbacks [28–30]. Besides nano- and carbon coated particles, $LiFePO_4$-particles have been doped with e.g., Al, Nb, Ni, Mn, Mg, W, Ti or Zn in an attempt to improve the material conductivity [31–40].

Active materials with layered structures (2D) are often used in order to achieve higher specific capacities. One of the most important representatives is the compound lithium-cobalt oxide $LiCoO_2$, which shows a high average potential of 3.9 V vs. Li^+/Li, high cycle stability and low tendency to oxidative decomposition [20, 41, 42]. Approximately 50% of the intercalated lithium can be deintercalated from the lattice structure, resulting in a relatively low practical capacity of 150 mAg^{-1}. Moreover, high material costs lead to alternative cathode materials such as lithium-nickel oxide ($LiNiO_2$) and lithium-manganese oxide ($LiMnO_2$). The former is isostructural to $LiCoO_2$, has lower costs, better high current behavior as well as a higher theoretical capacity of 200 $mAhg^{-1}$ and an average cell voltage of 3.8 V [43–45]. However, this material shows a high degree of electrolyte decomposition, an expensive synthesis and thermal instabilities of the deintercalated material. On the other hand, low-cost and environmental friendly $LiMnO_2$ exhibit a specific capacity of approximately 190 $mAhg^{-1}$. This material yields an irreversible phase transformation into the spinel structure, resulting in poor cycle stability [20, 46–48].

Lithiated manganese oxide in the spinel crystal structure ($LiMn_2O_4$) provides 3-dimensional transport paths for Li^+-ions. It shows a high discharge potential of 4.0 V and a capacity of about 120 $mAhg^{-1}$. Compared to $LiCoO_2$, $LiMn_2O_4$ has a relatively high electronic conductivity, a good stability against overcharging and thus high safety as well as a low price and good environmental compatibility [20, 49]. However, the release of manganese from the crystal lattice and structure transformations at low charge states lead to a low long-term cycle stability. Manganese spinel can be stabilized using blend electrodes, i.e. mixing $LiMn_2O_4$ with $LiCoO_2$ or $LiNiO_2$, as well as by substitution of part of the manganese by other elements. Therefore, the combination of high cycle

stability, high specific capacity as well as safety and environmental compatibility from $LiCoO_2$, $LiNiO_2$ and $LiMnO_2$, respectively, was used to develop new $Li(Ni_{1-y-z}Mn_yCo_z)$ compounds, also called NMC. Depending on the mixture proportions, the attainable capacity lies between 130 and 160 $mAhg^{-1}$, with an average discharge voltage of approx. 3.9 V. This material is characterized by high cycle stability even at high currents, low volume change during lithium intercalation, and good safety properties [50–53].

On the negative electrode side, elemental lithium metal meets all requirements for anode materials. Its considerably high theoretical capacity of 3860 $mAhg^{-1}$, extremely low electrode potential and high electrical conductivity make elemental lithium the perfect anode material. Except for primary batteries, lithium metal is not used as anode due to major safety drawbacks. Cycling of lithium metal not only consumes lithium, causing a limited cycling capability of the cell, but the cycled lithium is also irregularly deposited on the anode surface. Lithium is deposited at the first available free place at the surface of the anode and forms needle-shaped lithium dendrites, which in extreme cases cause a short circuit with subsequent fire and bursting of the cell [54]. Nonetheless, basic electrochemical characterization of electrode materials is carried out in half-cells using elementary lithium as counter-electrode. As an alternative for lithium metal, lithium alloys were also studied. Despite the achievable high capacities of these materials, the significant volume change during intercalation lead to poor cycle stability and irreversible capacity loss.

Lithium titanate, spinel ($Li_4Ti_5O_{12}$) offers a theoretical capacity of 233 $mAhg^{-1}$, which is reduced to approximately 150 $mAhg^{-1}$ in practice. It exhibits good thermal stability, low cyclic and calendar aging, high mobility for lithium ions, and no electrolyte reduction at a potential of 1.55 V vs. Li^+/Li. In addition, minimal volume changes occur during Li intercalation, resulting in low capacity loss. However, low conductivity render a significant disadvantage for this material. Particle size reduction and ion doping have been studied as methods to increase the conductivity [55, 56].

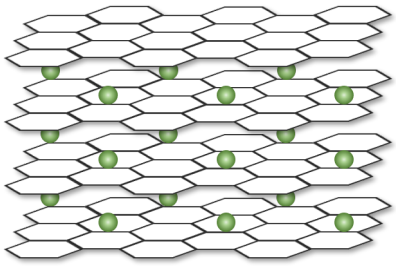

Figure 2.6: Schematic crystal structure of lithiated graphite.

Traditional lithium-ion cells use crystalline graphite as anode material, which has a maximum theoretical capacity of 372 $mAhg^{-1}$. Even though this material has poor capacity retention at high current density, its intercalation stability, long-term cycle life, significantly low electrode potential and irreversible capacity loss as well as low price and

high environmental compatibility sum-up to numerous advantages for its application in LIB [20]. Graphite consists of parallel, offset stacked graphene layers as shown in Figure 2.6 for its lithiated crystal structure. The intercalation of Li^+-ions in the graphite lattice takes place through a step process due to its specific crystal structure. First every fourth graphite interlayer is filled with Li-ions, then every second and finally every interlayer. During this process, the stacking sequence of the graphene layers changes, resulting in an increase in volume of about 10%.

Silicon (Si) anodes have attracted considerable attention in the past decade due to its significantly higher specific capacity of approximately 3579 $mAhg^{-1}$ for its $Li_{15}Si_4$ phase. It also exhibits a low discharging potential, is abundant, inexpensive, and environmentally friendly. However, Si-based electrodes yield poor electrical conductivity, short cycle life and large volume expansion during lithiation [57–60]. Drastic volume expansions of about 400% in the fully lithiated state of Si lead to cracking of Si particles, causing prompt degradation of the components connectivity in the electrode [61]. Despite the extensive research work regarding the performance improvement of Si-based anodes, most of the methods involve complex processes and require expensive overall costs, limiting the practical application of this promising material.

Electron conducting additives are essential components of lithium-ion batteries due to the low conductivity of most electrode active materials. The conductive additives do not contribute to the electrochemical process of the cell but are imperative to lower the internal cell resistance, improving the power density and specific power of the cell. Numerous nano-carbon materials, such as carbon black, ethylene black, acetylene black, ketjen black, conductive graphite, graphene nano-sheets as well as carbon nanofibers and nanotubes have been used for this purpose [62–70]. Conductive fillers with higher aspect ratio, like carbon nanofibers/-tubes and graphene nano-sheets, have been extensively studied as conductivity aids due to their ability to effectively form conductive pathways between active material particles at lower concentrations. However, its high chemical inertness, high electrical conductivity, low cost and long durability after cycling make carbon black (CB) the most frequently used conductive additive for conventional electrodes. CB is commonly used as a powder of colloidal particles under 100 nm, which tend to form agglomerates of up to 5 μm diameter. The formation of this branched clusters are, in turn, contra-beneficial for the cell performance. Therefore, several studies have investigated the break-up of CB agglomerates and dispersion mechanisms of the CB particles [71–74]. Sill, van der Waals attraction forces may lead to formation of CB agglomerates even after agglomerate break-up. Hence, particle dispersion must be accompanied by simultaneous particle stabilization. The addition of polymeric binders result in steric stabilization, promoting the formation of conductive network through the electrode layer, thus enhancing electron transport kinetics. The relationship between conductive additives and polymeric binders is discussed in the next section. The amount of CB in the electrode must be optimized to comply with the trade-off between cell energy and power. In order to reduce electrode resistivity the CB concentration must reach the percolation threshold at which conductive paths are formed. Beyond the

percolation threshold, conductivity does not increase much. The determination of this critical amount is essential to optimize electrode performance.

2.2.3 Polymeric binder

Polymeric binders have been consider of minor importance for lithium-ion electrodes due to their chemical and electrochemical inactivity. However, it is now of common consence that the binder, even at very low concentrations, plays a critical role in the electrode performance. In addition to the active material and conductive additive, polymers are dissolved/dispersed in a solvent during the electrode manufacture process to prepare the electrode slurry, which is then cast onto the current collector and dried. These polymeric additives strongly affect the flow behavior of the electrode slurry as they may act as thickening agents increasing slurry viscosity, but also as dispersing agents as they interact with the solid particles in the slurry, controlling structure and flow, i.e. the processing behavior of the slurry. As discussed in section 2.1, non-adsorbing polymers affect the rheological properties of the liquid phase, whereas adsorbing-polymers interact with the particle surface, stabilizing the particles against agglomeration. Hence, the formed particle-network in the wet slurry defines particle dispersion in the dry electrode. Optimal polymer concentration result in homogeneous particle dispersion, improving Li-ion as well as electron conductive pathways and thus enhancing ion intercalation. Furthermore, polymeric binders fundamental function is to ensure mechanical integrity of the electrode. Due to the volume fluctuations during the lithiation and delithiation of the electrode, the binder must cohere active materials and conductive additives together in addition to ensure sufficient adhesion strength between composite layer and current collector. Therefore, polymeric binders have an enormous impact on the stability and cycle performance of the electrode.

The choice of a suitable polymeric additive is essential to its effective application. Analog to conductive additives, the binder is kept to minimal amounts, exploiting its advantages without compromising the electrochemical properties of the active material. Thus, different polymer characteristics must be considered. Its selection usually follows the following criteria [75]:

- Facile processing of wet slurry and dry electrode
- Insolubility in the electrolyte and low swelling
- High chemical, thermal and electrochemical stability
- High cohesive strength withing the electrode layer
- High adhesive strength between electrode layer and current collector
- Low cost and high environmental compatibility

Polyvinylidene difluoride (PVDF) is the traditional polymeric binder for both cathodes and anodes for commercial LIB due to its good electrochemical stability and excellent binding strength. However, this binder is insoluble in water and requires organic solvents like N-methyl-2-pyrrolidone (NMP) for electrode processing. Since these solvents are not only environmentally harmful, but also toxic, flammable and expensive, safety concerns and high costs are associated to their use in LIB [76–78], especially for the upcoming high-volume production of electric vehicles. Therefore, greener alternatives have been developed for electrode fabrication. Regarding electrode processability, environmentally benign solvents, such as water and ethanol, are favored for dissolving or dispersing the polymeric binder. Fluorinated polymers like poly(tetrafluoroethylene) (PTFE) can be dispersed and stabilized in water, enabling aqueous electrode processing. The strong C-C and C-F bonds of these polymers provide high chemical and thermal stability, rendering them suitable for LIB. Although fluoropolymers can be processed in aqueous systems, they are characterized by their resistance to solvents, acids and bases, complicating their disposal after battery life. Usually, expensive, flammable and/or toxic solvents must be used to decouple these polymers from the electrode, diminishing their potential as environmentally benign binders. Hence, fluor-free polymers have caught attention in the past years. Polyacrylates, aliphatic and aromatic synthetic polymers, such as polyacrylic acid (PAA), polyethylene (PE) and polystyrene (PS), respectively, are the most popular selection due to their rubbery nature, offering good mechanical stability and enhancing electrode cycle life. The already established large-scale production of these compounds would facilitate the transition from fluorinated polymers and organic solvents to a more environmentally compatible electrode for commercial LIB. Still, this electrode concept would rely on non-renewable polymers.

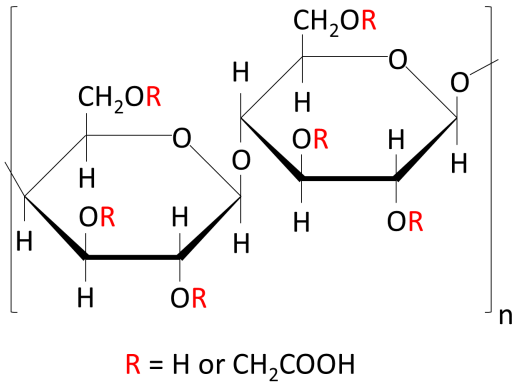

Figure 2.7: General chemical structure of carboxymethyl cellulose.

Naturally available bio-polymers and their derivatives can be processed in water-based systems, are environmentally sustainable and can be easily disposed. Recently, oligo- and polysaccharides, such as carboxymethyl cellulose (CMC), chitosan, alginate, pectine, starch and gums, have been used as green alternative for polymeric binders. In the state-of-the-art production of LIB anodes, CMC is often combined with styrene butadiene rubber (SBR) as polymeric binder system. Contrary to pure cellulose, CMC

is soluble in water. It consists of a linear chain of two anhydroglucose units (β-linked glucopyranose residues) with three hydroxyl groups each (see Figure 2.7). Hydrogen atoms in the hydroxyl groups are substituted by carboxymethyl groups to enable the solubility of the molecule in water. Thus, the average number of substituted hydroxyl groups per anhydroglucose unit is maximal three and is described by the degree of substitution (DS). The typical DS for use in commercial products lies between 0.4 and 1.5 [79]. The physicochemical properties of CMC and the flow behavior of CMC-based solutions strongly depend on molecular weight (M_w), nature of substituents, DS as well as pH of the solution and CMC concentration [80–85]. Accordingly, the viscosity and hence the processing properties of the electrode slurry can be adjusted by varying the CMC properties and amount. Despite its advantageous ability to act as a thickener and surfactant in the wet slurry, CMC does not provide the required adhesive strength in the dry electrode due to its stiff and brittle nature.

In contrast, SBR does not significantly affect the flow behavior of the slurry, since it is not soluble in water it is added during slurry preparation as an aqueous dispersion of nano-scale particles. It has, however, a significant impact on the adhesive strength of the electrode layer to the current collector. Its flexibility, high tensile strength and abrasion resistance highlight the strengths of SBR, complementing the contrasting, poor mechanical performance of CMC. Consequently, these compounds have been paired as binder system, exploiting their corresponding advantages.

2.2.4 Cell manufacturing process

Selection of suitable and complementing active materials, conductive additives and binders is of utmost importance in the manufacturing process of lithium-ion cells. The selection criteria mentioned above must be considered to achieve good electrode processability and superior cell performance. Initially, the three main electrode components are mixed in a solvent, aiming at a homogeneous electrode slurry. It is particularly important that the network of conductive additive is uniformly dispersed. The mixing sequence of the main components, as well as the type of the mixing device and the mixing conditions, i.e. the kind of energy input, can have a great influence on the distribution of the components, the deagglomeration of aggregated solids and the flow behavior of the processed slurry [86–89]. At an industrial scale, dry mixing of the active material with some or all of the additives is often carried out before the wet slurry preparation, attempting enhanced solids dispersion [71, 73, 86].

After the mixing step, the slurry is coated on the metallic current collector foil. Usually, doctor blade (or tape casting), screen printing or slot die coating techniques are employed to coat thin electrode films. The latter is commonly used in industrial manufacturing processes due to its high efficiency, precision and volume flow rate. Subsequently, the solvent is removed from the wet electrode in the drying step. The drying conditions, such as temperature and time, have a substantial impact on the binder distribution in the resulting dry electrode. Binder migration and distribution of solid particles during

solvent evaporation can be detrimental for the mechanical properties of the electrode, especially for the adhesive strength between layer and current collector [90–94]. Following the solvent removal, the dry electrode is compressed in the calendering step. The pressure applied on the electrode surface compresses the electrode, reducing the porosity of the layer and increasing interparticular contact. Therefore, the electrode conductivity and the mechanical integrity of the electrode can be enhanced. In addition to the reduced porosity, the volumetric energy density of the electrode is increased [95, 96]. Finally, individual electrodes are punched out and assembled together with a separator and a counter electrode to form the cell, which is then filled with an electrolyte. The quality of the resulting cell, thus, depends on numerous aspects influenced by the different steps involved in its manufacturing process (see Figure 2.8).

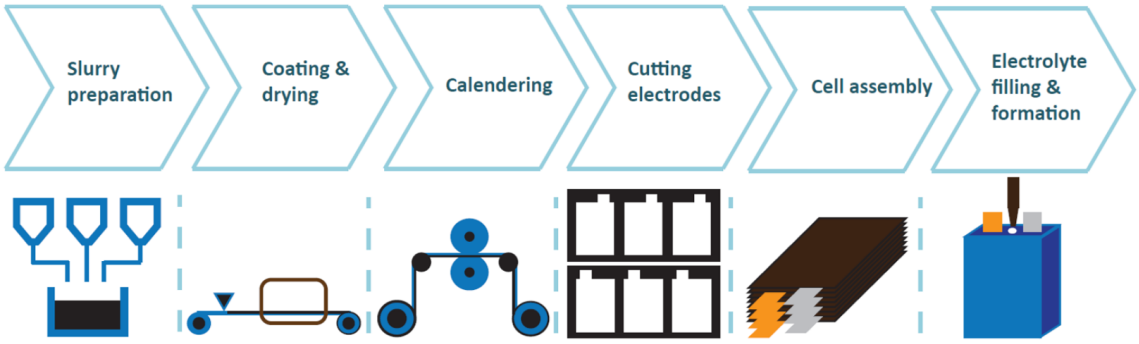

Figure 2.8: Schematic representation of manufacturing steps of lithium-ion cells. Edited from [97].

Li-ion electrodes can be fabricated into different cell types varying not only in their shape but also in their advantages and disadvantages. Cylindrical cells are still the most widely used packaging design, which can be manufactured cost-effectively and in large quantities. These cells consist of rolled up double-coated electrodes as shown in Figure 2.9A. The tubular cylinder can withstand high internal pressures without deforming, yielding high mechanical stability. Cylindrical cells may exhibit safety features such as a positive thermal coefficient switch and a pressure relief mechanism for short circuit and positive pressure protection, respectively. Despite their high specific energy and long calendar life, these cells lack ideal packing density when assembled into large battery packs. However, the empty spaces can be used to improve thermal management of the cell. Cylindrical cells are typically used for portable applications including power tools, medical devices, laptops and e-bikes.

Button cells, also known as coin cells, are compact and inexpensive (see Figure 2.9B). Although these cells show low capacities, they can be stacked in a tube to achieve higher voltages. Coin cells usually charge at low rates and swell if charged too rapidly, leading to safety drawbacks. Nevertheless, these cells have a remarkable calender life, offering long service. Most coin cells are non-rechargeable, primary cells used for small devices like watches, calculators, medical implants and hearing aids. Prismatic cells use a flat layered

or stacked approach, optimizing packaging space as well as offering flexible designs and satisfying consumer demands for thinner technologies (see Figure 2.9C). However, their manufacture is more expensive compared to other cell types. Apart from the casing, this design is very similar to that of cylindrical cells.

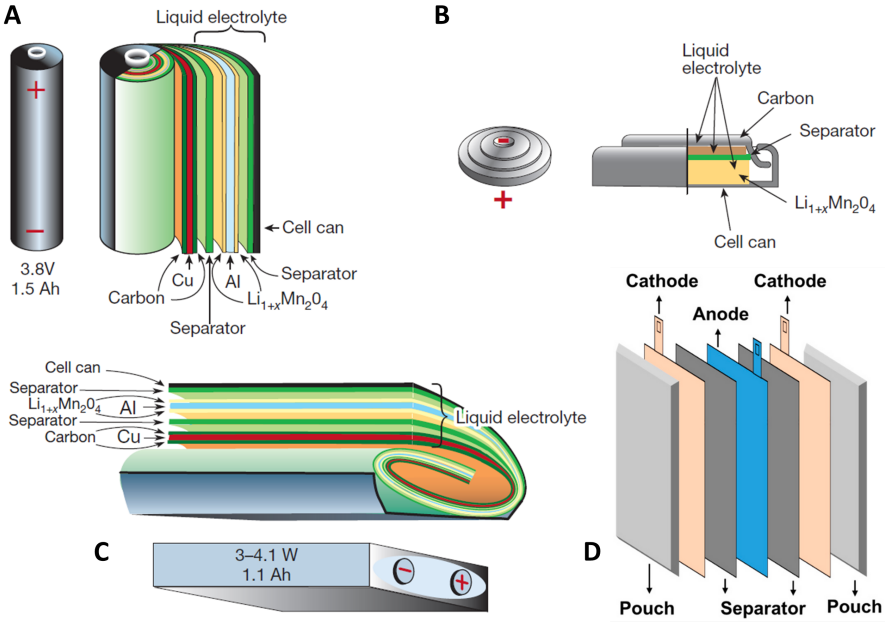

Figure 2.9: Schematic illustration of different cells types including their corresponding components. (A) cylindrical cell, (B) coin cell and (C) prismatic cell. Edited from [14, 98].

Prismatic single cells are predominantly found in small devices such as mobile phones, compact cameras and music players. Furthermore, these cells are also used for battery units in electric powertrains, battery electric vehicles and plug-in hybrid electric vehicles, as they offer good mechanical stability.

In contrast to other cell types, pouch cells commonly use a coated, flexible aluminum foil as casing instead of a metallic housing (see Figure 2.9D). In addition to being chemically resistant to the electrode and electrolyte components, the coated foil acts as an isolator. Conductive foil-tabs are welded to the stacked electrodes and are sealed on the outside of the cell. This flexible and light-weighted cells are the most space efficient and can endure high load currents. This design, however, needs space in the battery unit to expand due to swelling. Analog to prismatic cells, there is no standardized design, allowing for different cell dimensions. Pouch cells can be found in similar applications as prismatic ones.

2.2.5 Cell charge and discharge

The performance behavior of LIB strongly depends on environmental and operating conditions such as temperature, load current, state of charge (SOC) and current rate (C-rate). The electrochemical behavior of electrodes investigated in this work is studied using charge/discharge performance tests (cycle tests) on half and full coin cells including different electrode combinations. In addition to offering information regarding capacity retention, cell efficiency and long-term cycle life, this characterization method enables a correlation between electrochemical behavior and physical as well as chemical properties of the corresponding electrode.

The charging process of a LIB can be controlled by current or voltage. Charging, usually, follows the CCCV-aproach consisting of a first period of constant current (CC) and a subsequent period of constant voltage (CV) as shown in Figure 2.10A. A CC charge is applied until reaching the upper cut-off voltage (UCV). This voltage is then maintained until the current, which continuously drops due to the increase in internal resistance, has reached its lower limit. The CCCV method combines the high currents with the current limiting charging of the CV and CC, respectively, using their disadvantages to limit the amount of current and effectively charge the battery. A pure CC charge could overcharge the battery or, in turn, risk an incompletely charged battery due to interruption in order to avoid overcharging. The discharging process can take place at different currents under consideration of the upper limit. Generally, a cut-off voltage is provided to indicate the depth of discharge (DOD).

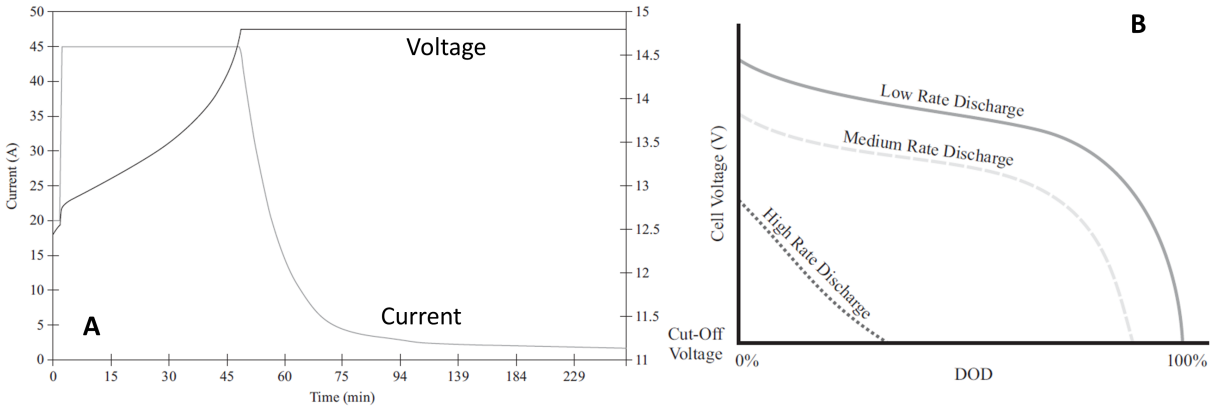

Figure 2.10: Exemplary (A) constant-current and constant-voltage charge curves and (B) voltage curves for different discharging rates. Edited from [99].

The SOC determines the working range of a battery, i.e. the available capacity until reaching the cut-off voltage. A 100% SOC (or 0% DOD) defines a fully charged battery. The charge and discharge dynamics as well as the ability to use battery capacity strongly depends on the C-rate. It measures the rate at which a battery can be charged and discharged. This technical parameter reflects the charge or discharge rate of a cell at a constant current in relation to a given cell capacity. For example, a 1C discharge

rate for a 1Ah battery should provide 1A for an hour. The available capacity can be assessed by plotting the measured voltage over time or DOD at constant current for different discharge rates as displayed in Figure 2.10B. Voltage curves approximate to the equilibrium cell potential, exhibiting ideal near constant voltage decay over time. Higher rates lead to ohmic and charge transfer kinetic losses in addition to mass transport limitations, shifting the voltage-curve downwards. Strong voltage decays at high C-rates indicate limited capacity availability.

The capacity retention capability or long-term cycle stability of batteries is studied using charge/discharge tests, commonly known as cycle tests. Typically, the discharge capacity of the battery is plotted as function of the cycle number at a constat C-rate. Initial capacity differs from theoretical capacity due to the formation of the solid electrolyte interphase (SEI), defined by irreversible Li-ion loss during the first cycle. Generally, capacity drops monotonically over several hundred cycles as a result of increase of the internal resistance of the cell due to volume fluctuations of the electrode or a further thickening of the SEI. This degradation mechanisms are addressed in the following section. Eventually, nominal capacity drops significantly, indicating the end of the battery cycle lifespan. Note that nominal capacities below 80% of the initial capacity after 500 cycles are no longer consider for electrochemical investigation regarding state of the art batteries.

2.2.6 Degradation mechanisms

Li-ion batteries degrade as a result of operation and environmental conditions, limiting their performance and life span [100–102]. Several chemical and physical mechanisms affect the electrodes, electrolyte, separator and the current collectors, leading to cell degradation. Figure 2.11 illustrates the most common degradation mechanisms in Li-ion cells. Chemical degradation is caused by irreversible side reactions at the components interfaces as well as by contact between different cell components, resulting in further undesired reactions. Physical or mechanical degradation is induced by the volume fluctuations during repeated intercalation of lithium-ions into the active material. Therefore, high temperatures, currents, voltages, operating time and mechanical stresses can trigger different aging mechanisms which increase internal resistance of the cell, decrease cell capacity and lead to end of battery life [103].

Undesired, irreversible side reactions may take place on both the anode and cathode side. At the anode, the degradation mechanisms focus on parasitic reactions such as decomposition reactions, lithium plating and SEI formation. The SEI is a complex, inhomogeneous, passivation surface layer formed at the anode/electrolyte interphase during the reduction reaction of the first charge/discharge cycle, also known as the formation step. It protects the electrolyte from further decomposition and the anode from co-intercalation of solvent molecules into the graphite crystal structure and associated exfoliation. However, the continuous formation, dissolution, re-forming and growth of the SEI leads to losses of capacity and performance due to increasing impedance

and loss of lithium and active material. High temperatures increase SEI decomposition and promote stabilization of meta-stable SEI components, decreasing ion conductivity [104–106]. In turn, low temperatures or high currents cause lithium metal deposition on the anode surface (lithium plating) and dendrite formation, leading to further reactions with the electrolyte, rapid capacity loss and in worst case scenarios induce a short circuit [101, 107, 108]. In addition, the decrease in porosity due to SEI growth also leads to impedance increase and overpotentials, as the electrolyte inhomogeneously distributes throughout the anode. Deep cell discharge and electrolyte side reactions can also result in corrosion of the current collector foil. The cathode, on the other hand, faces structural changes during lithiation, decomposition reactions and formation of a surface film due to precipitation of side-reactions products. Although the film does not significantly grow during aging, its porosity, conductivity and diffusion coefficient change over time as result of the precipitate blocking the pores. Depending on the selected active material, decomposition reactions of the electrolyte and the binder, oxidative decomposition of the cathode material, gas evolution and corrosion of the current collector may occur. Moreover, transition metals may decompose, migrate to the anode side and deposit onto the electrode layer, contributing to the dendrite formation. These dendrites can grow through the separator and come into contact with the cathode material, leading to instant cell failure [109, 110].

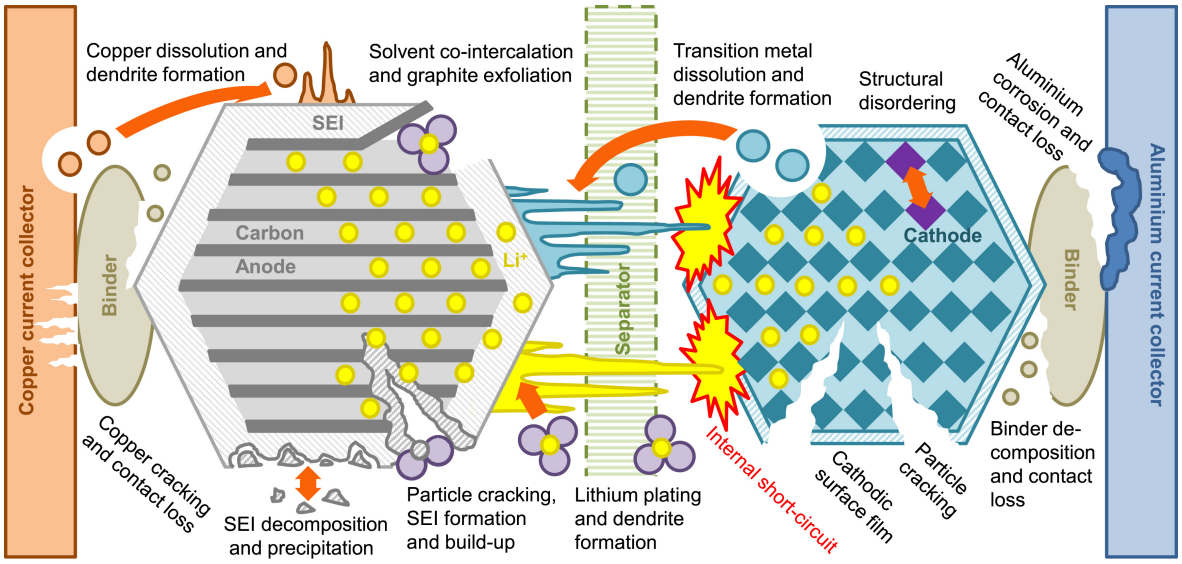

Figure 2.11: Schematic illustration of degradation mechanisms of Li-ion cells [103].

In addition to chemical side reactions, mechanical degradation mechanisms play a key role in the aging process of the Li-ion cells. The cyclic inter- and deintercalation of the Li-ions into the active material during battery operation leads to expansion and shrinkage processes. The corresponding volume fluctuation results in mechanical stresses. Mechanical degradation mechanisms have an impact on a particle or even molecular level as well as at a macroscopic scale defined by inhomogenities of the electrode structure [111]. Heterogeneous structures can lead to nonuniform current and ion distribution

in the electrode and thus inhomogeneous cell degradation [112,113]. Mechanical stresses within the active material may induce particle crack formation or complete break-up as shown in Figure 2.12A [114,115]. Furthermore, the change in volume of the active material can lead to separation of the electrical conductive paths between active material and conductive additive as well as between active material and current collector (see Figure 2.12B) [114,115]. As a result, the electrical and ionic conductivity of the electrode deteriorates, increasing the internal resistance and decreasing the capacity of the cell. Volume fluctuations can induce electrode cracks at a macroscopic scale and contact loss between binder and metal foil, which in extreme cases can result in a short-circuit due to electrode delamination. The choice and quantity of the polymer binder used has a direct impact on the degree of degradation. Appropriate mechanical properties of the binder can significantly suppress the mechanical degradation mechanisms affecting capacity, power and cycle life performance.

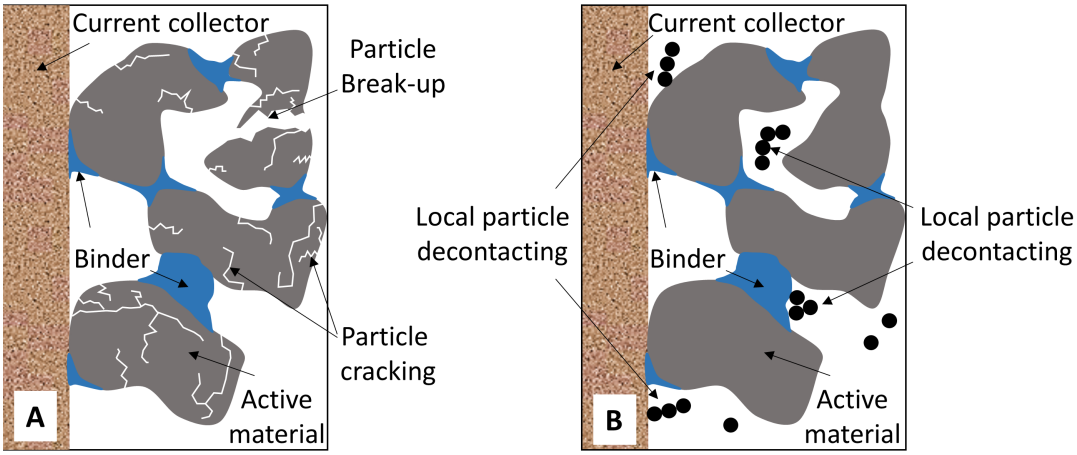

Figure 2.12: Schematic illustration of (A) particle cracking and break-up as well as (B) particle decontacting due to mechanical degradation of Li-ion cells.

3 Motivation and manuscript outline

The first rechargeable LIB for consumer electronics was launched in 1991 by Sony and was further developed through the years based on the fundamental work of A. Yoshino, J, Goodenough and S. Whittingham [41, 116, 117]. The basic principle has not changed since then, but the materials and process technology are constantly being developed. It is commonly accepted that battery performance depends significantly on the electrode properties and thus on the electrode architecture. So far, research and development has focused on new electrochemically active materials and their processing techniques to achieve high cell performance [118–120]. Electrochemically inactive binders, in contrast, have attracted little attention, although their application, analog to the active material and conductive additive, is essential to optimal cell performance. After all, polymeric binders control the dispersion state of active particles and hold the electrode mechanical integrity.

Considering the realization of ideally fully sustainable and environmentally friendly electrochemical energy storage devices, electrode processing must move on from the use of fluorine-containing polymers and associated toxic organic solvents to alternative binders using water-based systems. Therefore, several research activities concentrated on exploring novel aqueous binder systems for both electrodes including polyacrylic acid (PAA) [121–124], pectin [125, 126], chitosan [127–129], poly 4-styrene sulfonic acid (PSSA) [130], xanthan gum [131, 132], alginate [133, 134] and salts of carboxymethyl cellulose (CMC) [87, 135–138]. The latter is commonly combined with styrene butadiene rubber (SBR) as binder system. CMC strongly affects the rheological properties of electrode slurries as it acts as a thickening agent but also as it interacts with other components in the slurry, controlling structure and flow, i.e. stabilizing the slurry against sedimentation and determining the processing behavior of the slurry. As a result, the flow properties of the electrode slurry can be tuned to match specific needs during electrode processing, especially for the coating of the electrode slurry on the metallic current collector foil. The interactions between organic additives and active materials have been reported before, correlating the findings to the resulting electrochemical performance of corresponding cells [87]. Zeta potential and sedimentation measurements of $LiFePO_4$- and graphite-based slurries indicated that styrene butadiene rubber (SBR) and CMC adsorb on the active material particle surface and CMC, as a dissociable polyelectrolyte, provided a superior effect on the dispersion of solid particles through electrosteric stabilization. Lim et al. investigated the rheological properties and microstructure of aqueous, graphite-based anode slurries in dependence of binder content, reporting the formation of a gel structure at low and high CMC concentrations [139]. Accordingly, these structures were attributed to aggregation of graphite particles and formation of a polymer network, respectively. However, the implications of this effect on further electrode properties have not been assessed. The resulting assembly of particles in the dry electrode strongly depends on the particle dispersion state in the wet slurry. Several studies have shown the relationship between polymeric additives and particle distribution, reporting the formation of a conductive particle network at appropriate

binder concentrations [62, 140–142]. Consequently, controlling particle dispersion in the wet electrode slurry as well as the resulting component distribution and microstructure of the dry electrode layer is essential to achieve optimum Li-ion and electron transport properties, improving, in turn, rate capability, cell energy and power as well as cycle life performance. However, the final influence of polymer characteristics on electrode microstructure and conductivity still lacks understanding.

The fundamental role of polymer binders in the electrode is to ensure mechanical stability. During charge/discharge cycle of the cell, Li-ion intercalation leads to expansion and shrinkage of the electrochemically active material, causing mechanical stresses in the electrode [143–145]. Local delamination of the electrode layer from the current collector as well as cracking within the layer can be induced by these volume fluctuations. At a microscale, particle fracture and detachment of electronic conductive pathways between active material, electrical conductors, and current collectors reduce usable Li-capacities and aggravate irreversible capacity fading [110, 112]. Hence, the reliable determination of adhesive strength between electrode layer and current collector as well as cohesive strength within the layer is crucial. The former has been thoroughly investigated using an extensive range of measuring methods [123, 124, 129, 146–152]. Nonetheless, the cohesive strength of the electrode layer has not received much attention. Indentation, tensile and scratch tests have been used to characterize the mechanical strength of electrodes [146–148, 153–156]. Lee et al. studied the effect of molecular weight and degree of substitution of CMC on mechanical strength of lithium titanium oxide (LTO)-based anodes employing the scratch test [155]. Since the electrode layer experiences normal and tangential forces, this test provides information about adhesive as well as cohesive strength, complicating the interpretation of these results. Chen et al. decoupled particle to particle cohesive bonds from electrode layer to current collector adhesive strength combining micro-scratch and digital image correlation techniques, defining the coefficient of friction as a measure of cohesive strength [157]. However, it remains elusive whether the measured local forces are representative for the cohesive strength of the electrode layer. A. M. Gaikwad and A. C. Arias used a variation of the scratch test equipping a broader tip to suppress the large mismatch between the tip width and the particle size in the electrode layer [151]. The horizontal drag force required to break interparticle bonds was then correlated to the cohesive strength of the layer. Even though these studies provided some understanding about how mechanical properties of the electrode layer are related to slurry formulation and processing, the complex contribution of the binder to the processing behavior, mechanical integrity, microstructure and electrochemical performance of the electrode is not yet resolved.

Despite the vast amount of research on LIB, the overall contribution of polymeric binders to the battery performance still demands understanding. Controlling particle dispersion in the wet electrode slurry as well as the resulting component distribution and microstructure of the dry electrode layer is essential to achieve optimum Li-ion and electron transport properties. Therefore, polymer type and concentration are a key factor in electrode slurry formulation. Beyond that, the impact of binders on the mechanical

integrity of the electrodes must be thoroughly investigated with respect to battery cyclic stability and lifetime. At which extent the mechanical degradation impacts the power and energy density as well as cycle life of the cell still must be addressed. The independent determination of adhesive and cohesive strength is imperative to understand the delamination and cracking behavior due to cyclic lithium intercalation. Hence, it must be systematically studied how binders contribute to adhesion as well as cohesion. This is of special concern when it comes to identifying the source of decreased cell performance due to mechanical failure of the electrode. Moreover, the effect of polymeric binders on electrode microstructure should be investigated in detail, not only to understand what controls the mechanical properties but also to be correlated to the electrochemical performance of the electrode and corresponding cell. This will result in a deeper understanding of the role of polymeric binders in battery electrode slurries finally resulting in novel concepts yielding improved battery performance through targeted use of electrochemically inactive polymeric binders.

This thesis presents an experimental study on the role of polymeric binders in electrodes and corresponding cells for lithium-ion batteries. Anticipating a strongly growing, large scale production of Li-ion batteries for electric vehicles and storage of fluctuating energy supply from renewable sources, the focus lies on commonly used binders for environmentally benign water-based graphite anodes and $LiFePO_4$ cathodes. The interactions between polymeric binders and active materials as well as the effect of polymer type and concentration on rheological properties of electrode slurries is systematically investigated. The dispersion state of the active particles in the wet slurry is correlated to the component distribution, microstructure and resulting electrical conductivity of corresponding dry electrode layers. A detailed characterization of the mechanical properties, specifically of the cohesive strength within the electrode layer as well as the adhesive strength between layer and current collector, is carried out, including novel insights regarding the relationship between electrode microstructure and cohesion. Finally, the influence of the aspects outlined above on the electrochemical behavior of corresponding cells and thus battery performance is addressed.

The first section of this thesis introduces a brief overview of the current world environmental and energy situation, highlighting the importance of further research and development of innovative technologies for lithium-ion batteries. This is followed by the state of the art of LIB from their fundamentals, components and fabrication process to their design, performance and degradation, comprising a short theoretical background on slurry stabilization and particle/additive interaction key to comprehend the aspects discussed in this thesis. The motivation, aims and outline of the manuscript close this introductory part. The following main part of this work is divided in three sections consisting of a peer-reviewed scientific paper, each:
The publication in section 4 presents two different methods to characterize the sedimentation process of $LiFePO_4$ and CB particles in opaque suspensions used for LIB. Regarding the good slurry processability during electrode manufacture steps, optimal particle dispersion and slurry stability against particle settling are key. As an alternative

for optical characterization techniques, noninvasive spin-echo-based magnetic resonance imaging (MRI) experiments and gravimetric measurements using a sedimentation balance were carried out. The former offers new insights into the particle sedimentation in opaque suspensions, profiting from the ^{1}H images to uncover the spatial distribution of the particles and corresponding agglomerates, as well as the shape of the settling front. However, this method renders some limitations regarding low viscosity of the suspension and high particle loading. Thus, supplementing the MRI experiments, the increase in mass fraction over time due to the settling of particles at high, technically relevant concentrations was studied gravimetrically. In addition, the sedimentation behavior of an industrially applicable aqueous cathode slurry including $LiFePO_4$, CB and polymeric binders was investigated, showing reliable and reproducible results. The complementing application of the presented methods provide a reliable combination in order to characterize the sedimentation of opaque suspensions with different particle mass fractions for LIB.

Section 5 consists of a scientific article depicting the effect of concentration and type of two different polymeric binders on the dispersion state of $LiFePO_4$- and CB particles in water-based cathode slurries as well as the resulting mechanical and electrical properties of corresponding dry electrodes. Rheological data were used to characterize the degree of dispersion of active material and adsorption behavior of polymer on particle surface at technically relevant concentrations. Rheological data of the wet slurry were correlated to electrical conductivity experiments of corresponding dry layers, evidencing a clear relationship between the dispersion state of active particles in the wet and dry electrode. Moreover, the cohesive and adhesive strength of the electrode was independently determined for the first time, unveiling the singular contribution of different polymeric binders to mechanical integrity. Finally, the electrode microstructure was thoroughly examined, yielding further understanding of particle distribution and alignment defining the formation of the particle network in the layer. These results provide new insights into the relationship between electrode microstructure and mechanical stability and how polymer type and concentration affect cohesion. First results aiming at a characterization of the electrochemical behavior of half and full cells using the corresponding electrodes studied in this publication can be found in the outlook and appendix section of this thesis.

The third peer-reviewed scientific paper (section 6) in this work focuses on the influence of CMC type and concentration on the electrical and mechanical properties of water-based graphite anodes. Particularly, molecular weight, degree of substitution and concentration of CMC was varied in a wide range. Additionally, the effect of SBR type and concentration on the mentioned parameters was addressed. A detailed rheological characterization of the wet anode slurries was performed to assess the adsorption behavior of the binder in dependence of its properties at technically relevant conditions. The resulting electrical conductivity of corresponding dry layers was determined. A new approach to measure the cohesive strength in a well-defined way within the layer is introduced here for the first time, rendering reliable and reproducible results. All tests methods used here proved to be suitable for characterization of cohesive strength of electrodes for LIB. Compression strength data for water-borne anode layers comprising graphite, CB and CMC are presented. Furthermore, electrode microstructure was investigated, focus-

ing on the effect of CMC on the formation of a specific particle network configuration. New insights regarding the controlling factors governing over the mechanical integrity of the electrode could be derived from these results. Preliminary results regarding the electrochemical behavior of half and full cells using the corresponding electrodes studied in this publication can be found in the outlook and appendix section of this thesis.

Section 7 and 8 complete this thesis with a summary and outlook, respectively, compiling the most significant results regarding the role of polymeric binders in water-based electrodes for LIB as well as presenting preliminary results regarding the electrochemical performance of cell including selected electrodes studied in this work and proposing new ideas and potential next steps for future research and development of this topic.

4 Sedimentation of lithium-iron-phosphate and carbon black particles in opaque suspensions used for lithium-ion-battery electrodes

Full title:	Sedimentation of lithium-iron-phosphate and carbon black particles in opaque suspensions used for lithium-ion-battery electrodes
Authors:	Roland Balbierer, Ronald Gordon, Sebastian Schuhmann, Norbert Willenbacher, Hermann Nirschl, Gisela Guthausen
Status:	published [158]
Bibliographic data:	J Mater Sci 54, 5682–5694 (2019); DOI:10.1007/s10853-018-03253-2

4.1 Abstract

Sedimentation of opaque suspensions of carbon black and lithium-iron-phosphate was investigated by spin-echo based magnetic resonance imaging. Optical methods are usually applied to determine settling velocities, but are limited with respect to high concentrations and optical transparency. The presented method uses intensity data from the non-invasively measured magnetic resonance signal of the sample. The settling velocity is obtained from the evolution of the signal intensity profiles based on the contrast in ^{1}H magnetic resonance imaging between particles and liquid. New insights into the sedimentation in opaque suspensions are provided, since the ^{1}H images uncover the spatial distribution of the particles and its agglomerates, as well as the shape of the settling front. Additionally the sedimentation was experimentally studied using a sedimentation balance, which gravimetrically measures the increase of mass fraction over time due to the settling of particles. By parallel usage of these two methods, the sedimentation processes of opaque suspensions of lithium-ion-battery electrode materials was investigated. The sedimentation balance covers high, technically relevant concentrations. Limiting factors of the methods are discussed, which are mainly signal intensity in the magnetic resonance imaging and the increasing viscosity of high concentrated suspensions.

4.2 Introduction

Gravity driven sedimentation processes of carbon black (CB) and lithium-iron-phosphate (LFP) particles was observed by a sedimentation balance and magnetic resonance imag-

ing (MRI). These particles are increasingly applied as active material in lithium-ion-battery (LIB) electrodes.

The majority of LIB utilizes cobalt based cathode materials as well as aluminum, manganese and nickel blends to fulfil the dominant application demands [159]. In comparison to that and in regards to safety, LFP based cathodes deliver undisputable advantages, when the less dominant requirement is capacity. The lack of required conductivity and energy density/capacity of LFP is addressed by coating the nanoscale LFP particles with CB as well as adding CB nanoparticles [160–163]. New approaches insert silicon, tin or germanium to the active materials of electrodes, which reduce the mechanical stress during lithiation [164–167]. However, it remains to future generations of LIB whether the cyclical and calendrical stability of these materials meet the application requirements [15, 168, 169]. Thus, LFP presently is a commonly used electrode material with respect to well-balanced capacity and safety properties, as well as economic factors.

The slurries of the active material are steadily under improvement, due to the rising demand of increasing capacity and cyclic durability. To increase the homogeneity of LFP and CB particle distribution in the slurry, the particle systems of electrode materials are of general interest [170, 171]. Gravity driven sedimentation occurs and affects the homogeneity of particles distribution.

Over decades, the sedimentation of particles that vary in shape and kinematic properties was investigated. Several theoretical models were published and describe the experimental data within given limits [172–177]. The sedimentation itself can be understood as the movement of particles in fluids due to external forces, e.g. due to gravitational or centrifugal forces. Important for the motion in a suspension are certainly the density difference between particles and liquid, the particle volume fraction and their shape, as well as the liquid's viscosity. Several techniques were developed to optically study sedimentation [178–180]. The limitations of the optical methods are obvious: a certain amount of light needs to reach a photosensitive detector to measure the amount and rate of particle movement. Concentration is limited as hindered settling occurs due to particles interactions [181]. Suspensions with LFP and CB tend to become opaque even for low particle mass fractions (ϕ_p<0.5 %). Hence, optical measurements are limited regarding this class of materials.

MRI was used to explore sedimentation of CB and LFP in these opaque suspensions. As the particles themselves do not provide a ^{1}H-MRI signal, the MR intensity is due to the liquid in the suspension, which was silicon oil. The versatility of the MRI approach is emphasized as only a single suitable and nuclear magnetic resonance (NMR) active fluid needs to be applied to measure both particle classes *in-situ*. Signal intensities were measured spatially and time-resolved to observe the sedimentation at the bottom of an NMR tube, caused by settling particles with different particle size and agglomeration, i.e. the settling front (SF). In addition, a sedimentation balance was built to characterize the evolution of mass fraction over time. By parallel usage of these two methods, velocities

for CB and LFP at a given viscosity can be measured and the final slurry composition with the required particle fractions can be characterize in terms of sedimentation.

4.3 Materials

In order to achieve one suitable viscosity for both particle classes a silicon oil (Polydimethylsiloxane (PDMS), Quax GmbH, Germany) was used as fluidic phase in the suspension of the ^{1}H-MRI measurements. This choice allows the sedimentation to take place but simultaneously enlarges the time scale for the measurements. Carbon coated LFP, i.e. $LiFePO_4$ particles (Alees: Advanced Lithium Electrochemistry Co., Ltd., Taiwan) and CB particles (Alfa Aesar, United States of America) were used as received. The values for the specific surface area (SSA) for LFP were provided. According to the manufacturer, the mean size of the primary CB particles is approximately 42 nm. However, CB and LFP particles tend to agglomerate, reaching an average size of a few microns. Dispersed CB and LFP particles in PDMS also show this trend to agglomeration and increase the viscosity as a function of volume fraction [182, 183]. The density of the solid materials was determined using a helium pycnometer (Micromeritics, Multi Volume Pycnometer, Karlsruhe, Germany).

Table 4.1: Material properties of used fluid and particles.

Fluid	**Polydimethylsiloxane (PDMS)**	
$\rho(\vartheta = 25°)$	0.955 gcm^{-3}	
ν	20 mm^{2}s^{-1}	
η	19.1 mNsm^{-2}	
Particles	**Carbon Black (CB)**	**Lithium-Iron-Phosphate (LFP)**
$x_{50,3}$	5.47 μm	1.71 μm
rel.span	2.96	5.24
ρ	1.73 gcm^{-3}	3.51 g^{-3}
SSA	-	11.6 m^{2}g^{-1}
sample notation	CB_1, CB_2, CB_3, CB_4	LFP_1, LFP_2, LFP_3, LFP_4

The targeted particle mass fraction for the MRI experiments was ϕ_p= 0.5 wt%. This was achieved by a PDMS mass of m_F= 859.4 mg±1.3 % and a particle mass of m_P= 4.25 mg±5.8 %. This results in an overall sample particle mass fraction of ϕ_p= 0.495±0.036 wt%, which deviates from the targeted particle mass fraction of ± 7.2 %. Four samples of each material class were investigated by MRI (Table 4.1).

The equivalent sphere-particle size distribution (PSD) was determined by Fraunhofer diffraction (HELOS H0309, Sympatec GmbH, Clausthal-Zellerfeld, Germany) using an ultrasonic wet dispersing unit (QUIXEL, Sympatec GmbH, Clausthal, Germany) for dispersing the LFP and CB particles in acetone and ethanol respectively (Figure 4.1).

The same PDMS was used for the experiments with the sedimentations balance. In contrast to the MRI measurements the particle concentrations were vastly increased.

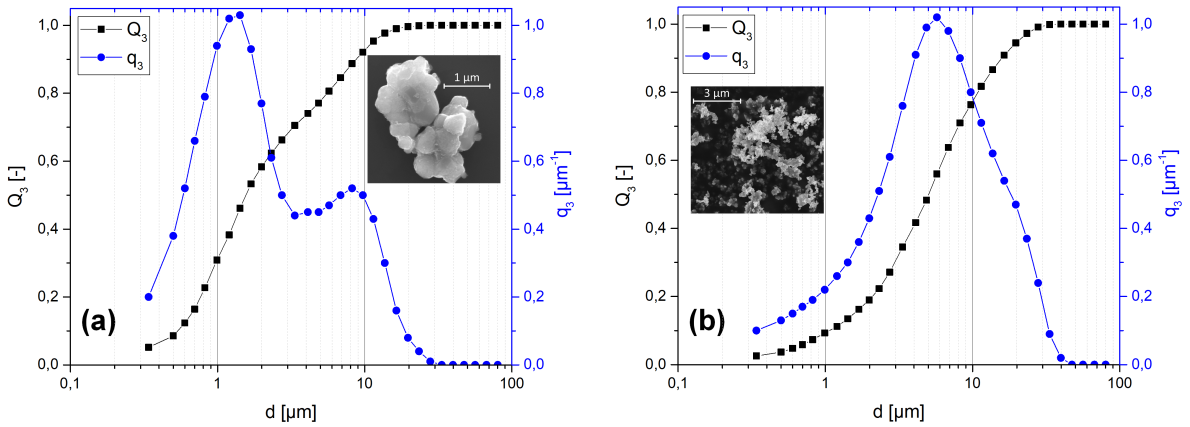

Figure 4.1: Cumulated particle size distribution (Q_3) and its density (q_3) of LFP (a) and CB (b). The insets show SEM images of a particle agglomerate of the respective material.

Experiments with particle mass fractions of ϕ_m=10,30 and 50 wt% for LFP were performed. The corresponding LFP suspensions had a low shear ($\dot{\gamma}$=2.2 s^{-1}) viscosity of η=0.1, 1.5 and 12.9 Pa·s, respectively (Figure 4.2).

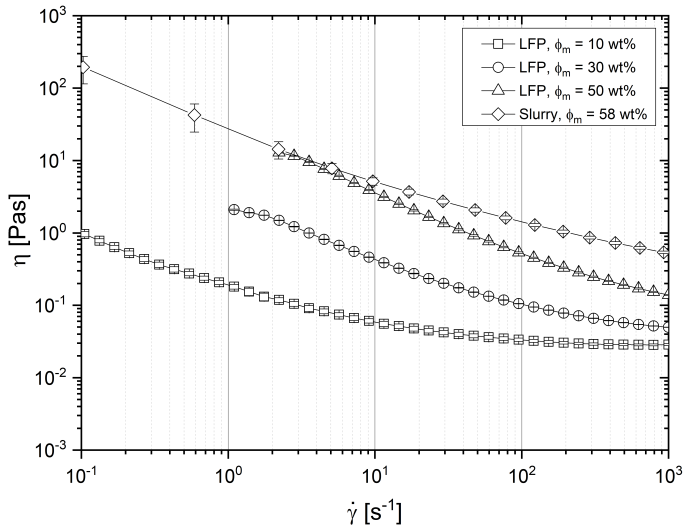

Figure 4.2: The viscosity η depends on the shear rate $\dot{\gamma}$. of the LFP suspensions with different mass fractions ϕ_m. The lines are guides to the eye.

Investigations of higher particle mass fractions with CB failed due to the increase in viscosity and the thus reduced and presumable absent sedimentation. Particle mass fractions of ϕ_m> 1 % for CB already showed the mentioned behavior. As CB is mainly added to increase the conductivity of LIB electrodes, low mass fractions of CB are realized in real applications. Hence, only three different mass fraction of LFP were investigated by the sedimentation balance, due to LFP being gravimetrically the main ingredient for the

active material of an LFB based LIB. Additionally, a practically relevant composition of an electrode slurry, used for LIB, was investigated by the sedimentation balance with respect to its sedimentation behavior. This composition is based on the experimental recipe of a LFB based LIB.

4.4 Experimental and methods

With the help of an in-house manufactured cylindrical Polytetrafluorethylen (PTFE) sample holder, two NMR tubes were placed side by side into a radio-frequency probe of the NMR spectrometer, i.e. into the field of view (FOV) (Figure 4.3). A sagittal slice across the center of the tubes was measured by MRI. A time series of experiments with identical parameters and orientation allows the measurement of the particle's sedimentation. Due to the NMR properties of the particles, i.e. especially their low ^{1}H-density and fast transverse relaxation, the images are negative images, i.e. the measured intensity is due to the liquid.

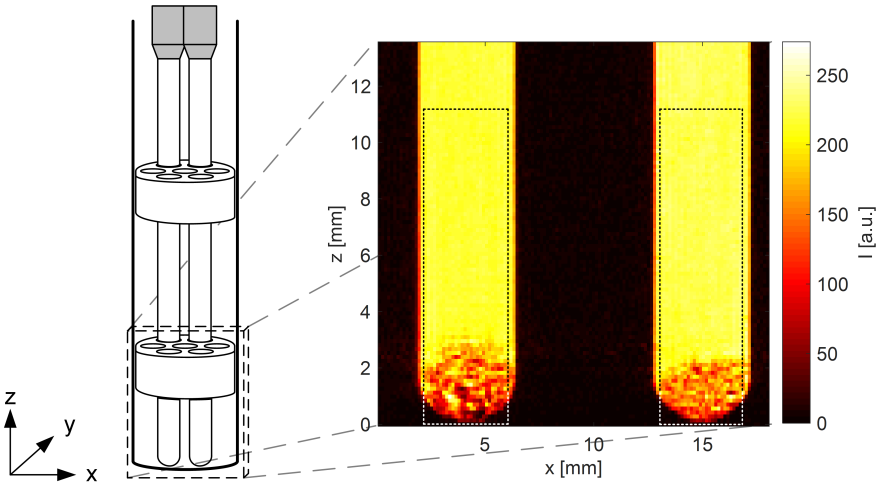

Figure 4.3: Experimental setup: two samples were measured simultaneously in one sagittal slice. A PTFE sample holder was used to provide robust and aligned orientation of tubes. High intensities correlate with low particle concentration and are attributed to the ^{1}H-MRI signal of the liquid.

The materials were separately inserted into a NMR tube after it was filled with 900 μl of PDMS. After coarsely dispersing the particles at the top of the PDMS, the tubes were placed into the probe of a Bruker 200 MHz Avance III HD spectrometer. The maximum gradient for imaging was 1.5 Tm^{-1}. The MICWB40-probe with a ^{1}H birdcage allowed for a maximum outer sample diameter of 20 mm. Hence, multiple NMR-tubes with outer diameter of 5 mm could be measured simultaneously (Figure 4.3).

4.4.1 Spin-echo-based MRI

The spin-echo based pulse sequence RARE (rapid acquisition with relaxation enhancement) was used for the MRI experiments with parameters specific for the materials and application (Table 4.2). The advantage of RARE with respect the often faster gradient-echo based methods is the reduced sensitivity towards magnetic susceptibility differences between materials, especially along the phase direction in the images. The samples were measured applying a 2D RARE sequence with slice selection. Thus, the MRI signal intensity evolution is a measure to the SF in the opaque suspensions. The acquisition time given by the timestamp of the MRI raw data was used as time axis of sedimentation.

Table 4.2: MRI parameters of the 2D RARE MRI experiments.

^{1}H-RARE MRI parameter	**Value**
Echo time	10.16 ms
Repetition time	2 s (CB), 1 s (LFP)
Number of averages	4 (CB), 2 (LFP)
RARE factor	4
Single experiment time	4:16 min (CB), 1:04 min (LFP)
Field of view (FOV)	18 mm * 18 mm (128 px * 128 px)
Slice thickness of the sagittal slice	1 mm
Resolution (isotropic in the plane)	140.6 μm

The aim of the study was to deduce the sedimentation velocity from the MR images. Mean values of the signal intensity were calculated. Only the image area in the middle of the tubes was considered. Boundary or wall effects near the tube's wall were therefore eliminated.

The wall-effects are neglected with the argument, that the ratio between the average particle diameter x obtained from PSD and the inner tube diameter of approximately D= 4.09 mm is relatively small [184]. The ratios for LFP and CB are: $\{x/D\}_{LFP}= 4.16{\cdot}10^{-4}$ and $\{x/D\}_{CB}= 1.34{\cdot}10^{-3}$. The thus defined region of interest (ROI) is the basis for the calculation of the z-profiles (dashed lines in Figure 4.3). For each tube, the ROI had a dimension (x,y,z) of 28* 1*79 voxels corresponding to 3.94* 1* 11.11 mm as the slice thickness in the sagittal slices was 1 mm.

The principle expectation for the measured MRI signal intensity of the evolving sedimentation is summarized in [173, 184–186]. As a suspension contains arbitrarily distributed particles, rather constant intensity of the liquid can be measured along z (Figure 4.4). As the particles continue settling over time, three regions are formed: suspension, clear liquid and sediment. These regions differ in particle concentration. Thus, the maximum signal intensity is measured in the liquid containing no particles. The lowest intensity is observed in the sediment layer. Between these two regions, the signal intensity varies due to various particle concentrations. After the particles settled completely, only particle poor and particle rich regions remain, which are reflected in the

MRI profiles along z (Figure 4.4).

The slight increase of intensity below the sediment layer in Figure 4.4, i.e. outside the glass sample tube, is due to susceptibility artifacts due to LFP particles, which arise from the increasing concentration of these highly paramagnetic particles at the bottom. This issue will be discussed later in more detail.

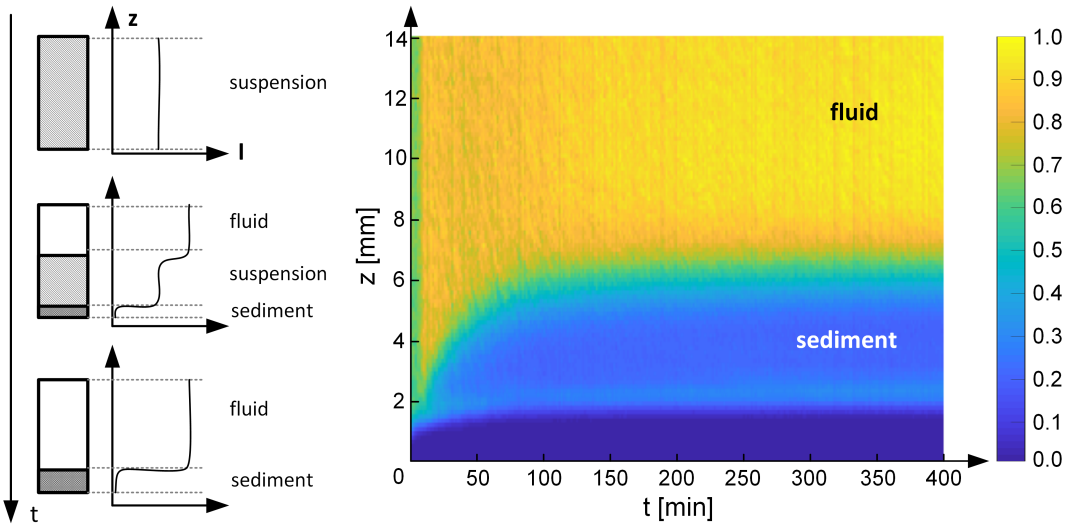

Figure 4.4: Scheme of NMR intensity profiles during sedimentation (modified from [184], left). In comparison, the measured z-profiles over 6 h 40 min are shown on the right. The experiment was performed on LFP particles with a volume fraction ϕ_m=0.32 vol% in glycerin/water mixture (80:20 wt%) with a total volume of 1.55 ml. The evolution of the settling can be observed in the profiles. The bottom of the tube was at z=1.13 mm.

The z-profiles, i.e. axial mean values, are a function of sedimentation time t as the particle concentration changes with t along z (Figure 4.5). Calculating horizontal mean values from unevenly distributed shapes of the settling front would result in a wrong interpretation of the evolution of particle sedimentation along z. Thus, apart from the z-profiles, the x-profiles were also calculated to get an estimation about the shape of the sediment's bed. Homogeneously distributed sedimentation over the cross section of the tube was observed, thus wall effects can be neglected in the ROI of the z-profiles.

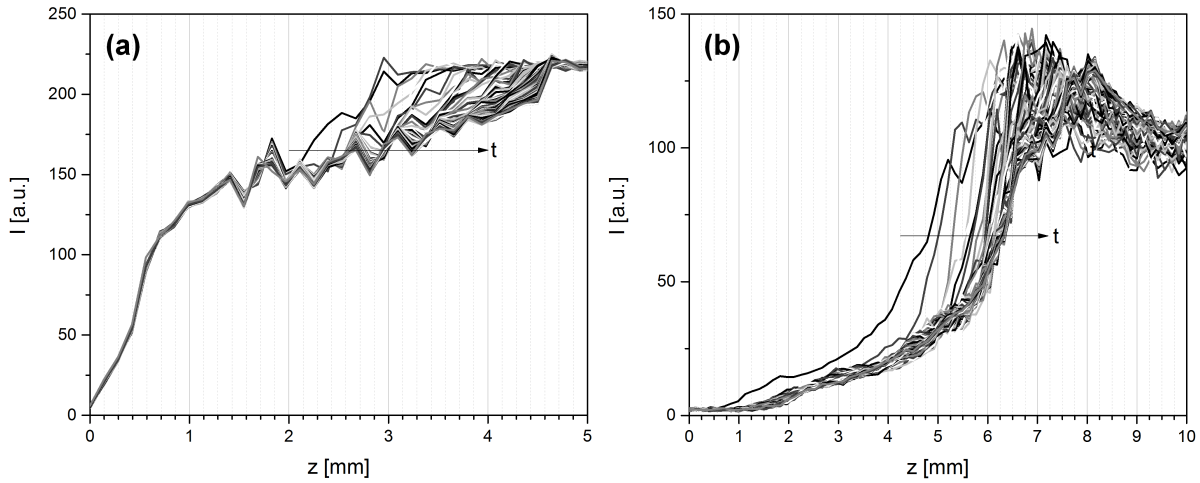

Figure 4.5: z-profiles as a function of sedimentation time t of samples CB_1 (a) and LFP_2 (b). The higher the intensity, the lower the particle concentration. The total experiment time for sedimentation was 18 h 51 min for CB and 5 h 47 min for LFP.

4.4.2 Sedimentation balance

A self-manufactured sedimentation balance was developed based on the standard DIN 66116-1:1973-11 and was used to measure the settling rate of the LFP particle suspensions and a commercial cathode slurry for LIB. (Figure 4.6).

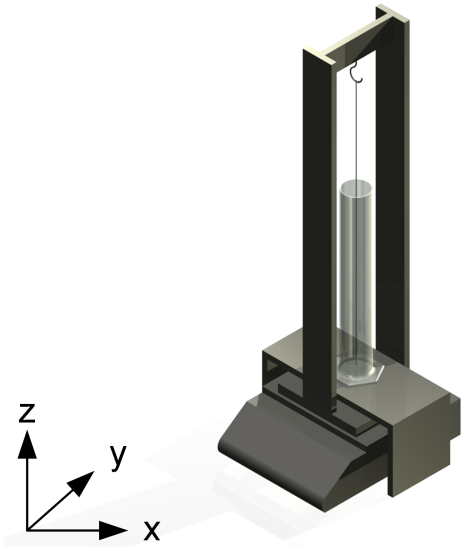

Figure 4.6: Schematic setup of the self-manufactured sedimentation balance based on standard DIN 66116 1:1973-11.

A steel stage was placed over a digital balance. A glass container rests on top of the steel stage, decoupling the weight of the glass container from the balance. A perforated

pan was mounted hanging from a frame, which is placed on top of the balance, using a steel wire. As a result, the weight on top of the pan was directly connected to the balance. In order to guarantee the retention of the settling LFP particles by the pan, a filter with a mesh size of 500 nm was attached on top. At first, the hanging pan was placed in the glass container, ensuring no contact. Subsequently, the suspension was poured into the glass container and the balance was tared. As the LFP particles settled on top of the pan the weight was directed through the steel wire and frame to the balance. The balance was connected to a computer, which recorded the time dependent weight increase using the software KERN Balance Connection 4. The weight was recorded each second for a total experiment time of 4 h 10 min for each sample. Suspensions with LFP mass concentrations of ϕ_m=10 wt%, 30 wt%, and 50 wt% were dispersed in PDMS using a dissolver at various speeds between 1500 and 2000 rpm.

4.5 Results and discussion

4.5.1 MRI measurements

The data set of I(z,t) (Figure 4.5) contains the complete information about sedimentation as the x-profiles (vertical mean values) showed no peak formation, but a uniform, evenly distributed intensity signal. Further data processing can now be performed either along z or t, in order to quantify the sedimentation process.

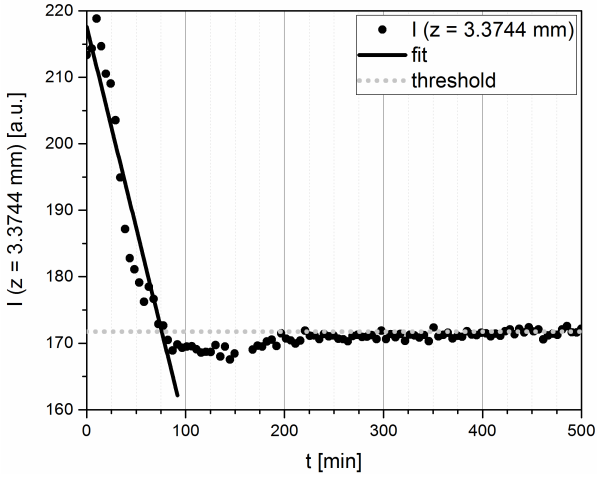

Figure 4.7: Signal intensity for z=3.3744 mm as a function of time t (dots) for the CB particle sample CB_1. The resulting profile is approximated by a linear function to extract the gradient of the signal intensity over t.

At first, the data is processed along t to obtain I(z = const,t): The intensity was computed as a function of sedimentation time for each of the 79 z-values measured for each sample. The form indicates an approximately linear dependence of I on t. Similar behavior was observed for all samples of the same particle type, i.e. LFP or CB. For each z-value I is approximated by a linear function to extract the gradient $\frac{\Delta I(z,t)}{\Delta t}$ of the signal

intensity over time (Figure 4.7). The standard algorithm was applied to solve non-linear curve-fitting problems in a least-square sense. The fitting parameters were calculated in the time range [0,82] min for the sample CB_1 (Figure 4.7). 0 min represents the first measurement respectively the first timestamp, which is approximately 2 min after sample preparation. The delay is caused by inserting the prepared sample into the probe and starting the experiment.

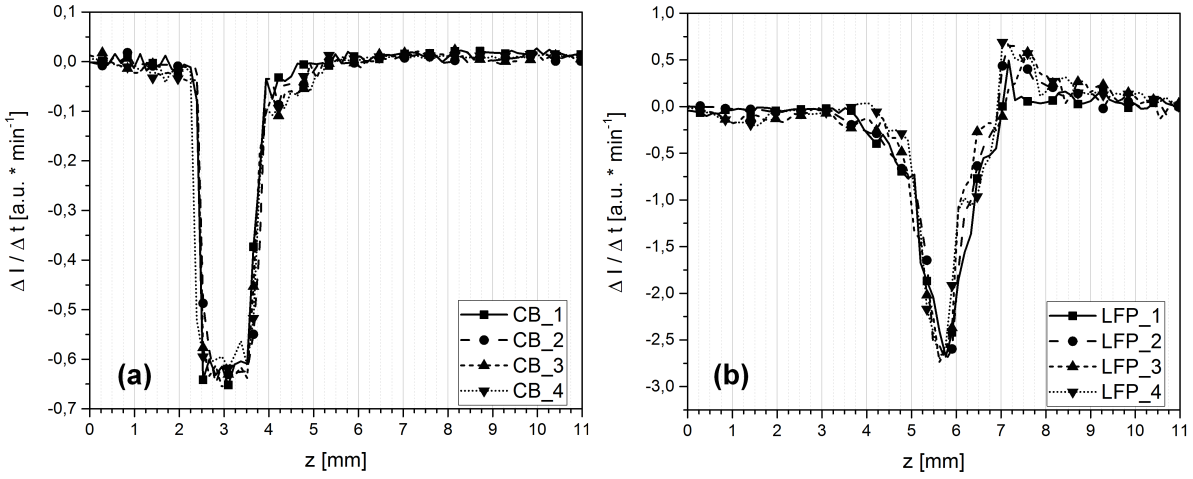

Figure 4.8: The gradient $\frac{\Delta I(z,t)}{\Delta t}$ reflects the sensitive regions and gives an estimate of the reproducability of the MRI measurements. The most sensitive region for CB (a) is found in the interval [2.5,4.0] mm, for LFP (b) in the region [4.0,7.0] mm. The lines are guides to the eye.

A mean value was calculated to define a threshold from the end to the middle of the data matrix, i.e. large sedimentation times. The data matrix had 233 data points in total, respectively 233 timestamps at a resolution of approximately 5 min for CB and 1.5 min for LFP. For better illustration a zoom is depicted in Figure 4.7. Starting from the first value, iterations compare the intensity values sequentially to the threshold. As soon as the value equals less than this threshold, the data points of intensities at larger t-values are not considered in the linear fit. The threshold was adapted to each z-value automatically. As the ROI contained 79 z values, the same amount of iterations were computed for each of the eight samples. The change in intensity $\frac{\Delta I(z,t)}{\Delta t}$ as a function of z gives insight into the reproducibility of sedimentation (Figure 4.8). The gradients are in good agreement in each particle class, i.e. LFP or CB. Relatively time-constant concentration profiles (i.e. $\frac{\Delta I(z,t)}{\Delta t} = 0$ are observed for top and bottom of the ROI. For the sedimentation of CB, the most sensitive values of $\frac{\Delta I(z,t)}{\Delta t}$ are in the range [2.5,4.0] mm; a second sensitive region was observed in the interval [4.0,5.0] mm. This probably represents smaller intensity changes $\frac{\Delta I(z,t)}{\Delta t}$ due to slower sedimentation of small particles with lower settling velocities. Furthermore the weighting error during sample preparation should be taken into account, especially at low particle mass fraction, i.e. ϕ_{p}=0.5 wt%.

In the case of LFP, the most sensitive region is observed for z∈[4.0,7.0] mm; additionally a signal enhancement at larger values of z occurs between 7 and 8 mm. An explanation of this pronounced difference within a certain material class can be found in different magnetic susceptibility χ_{magn}. The most sensitive axis regarding χ_{magn} is the read gradient axis in MRI, which was chosen along z in the experiments. As LFP is known to be paramagnetic, larger differences in $\mathrm{x}_{\mathrm{magn}}$ lead to spatially varying distortions of the main magnetic field of the NMR instrument with the consequence that NMR intensity shifts to other regions of the samples, leading to larger signal intensities in neighboring regions z>7 mm (Figure 4.8). Please note that some 10 ppm are sufficient for this type of artifacts in MRI [187–192]. Similar behavior of $\frac{\Delta I(z,t)}{\Delta t}$ was observed. Negative values represent declining signal intensities. Therefore, particles settle in this region.

The next step to process the experimental data (Figure 4.5) is to monitor the z profiles and to deduce the sedimentation velocity by analyzing the intensity isolines I(z,t)= const. The basis for the calculation of the sedimentation velocity is z (t,I= const) (Figure 4.9). The isolines were only computed at intensity steps of ΔI= 10 a.u. for both samples. In detail the intervals were for CB at I∈[150,210] a.u. and at I∈[20,80] a.u. for LFP.

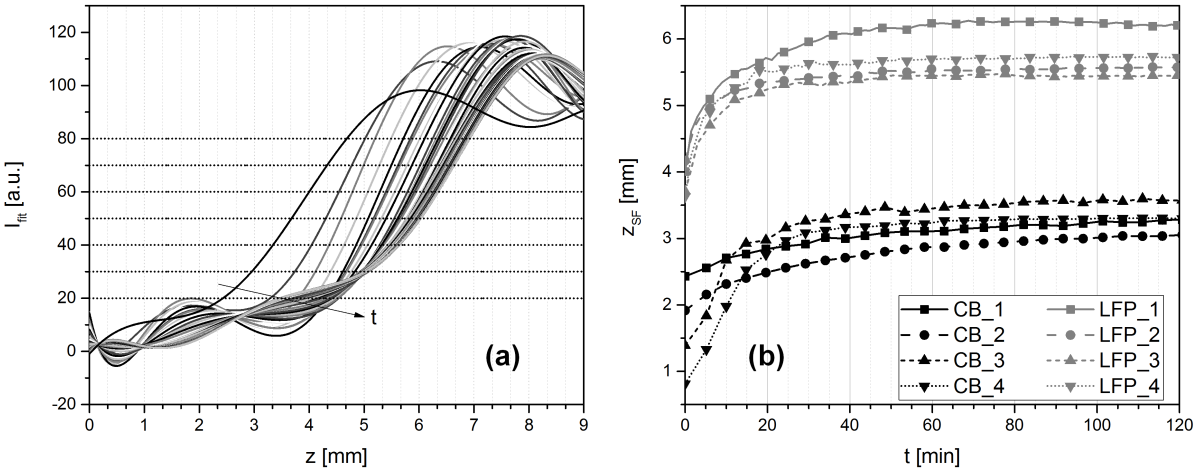

Figure 4.9: (a) Signal intensity profiles $\mathrm{I}_{\mathrm{fit}}$(z,t) as derived from polynomial fits to experimental data $\mathrm{I}_{\mathrm{exp}}$(z,t) of the sample LFP_3. Each profile represents a timestamp. Therefore, the settling front was observed from the intersections of the isolines with the profiles. (b) The progression of the settling front for all measured samples.

Since the measured data is discrete with limited signal to noise ratio, also due to the required time discretization of the measurement, each signal intensity profile was interpolated and therefore smoothed with a polynomial of the order n = 9 for CB and n = 7 for LFP. The high polynomial degrees were chosen to maintain the overall shape of the profile (Figure 4.9), while removing artifacts and statistical noise. The settling velocity was calculated by considering the determined time distance between each profile from

the timestamp and generating the required distance in z-direction by subtraction of the respective intersections. The quotient of $\Delta z/\Delta t$ provides the desired item and declines with t.

Sedimentation is dynamic process and the velocity is expected to be a function of sedimentation time. Therefore $v_{mean}=\Delta z/\Delta t$ was modeled by an exponentially decaying function. The fit describes the measured data well within the experimental error. Large particles with high velocities settle first and form the initial growth of the sediment. Furthermore, they entrain smaller particles and accelerate them or induce agglomeration. The resulting effect is a primary, rather large velocity, which declines as smaller and less agglomerated particles remain in the suspension (Figure 4.10).

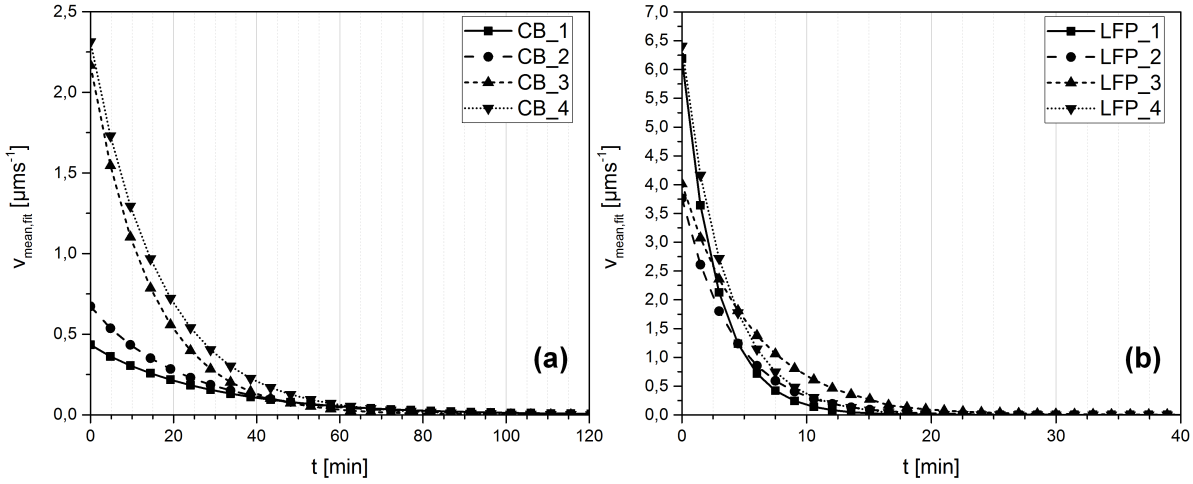

Figure 4.10: Settling velocities of the exponentially decaying model for CB (a) and LFP (b). The deviation for the velocities within the two material classes is a result of small variations of the particle mass fraction ϕ_p and of particle size distribution.

Further experiments with mechanically homogeneously dispersed particles were performed, but showed another aspect of the investigated material. As instruments exploring Fraunhofer diffraction use an ultrasonic wet dispersing unit and is mainly sensitive to agglomerates in the order of several μm, the particles nanoscale is not considered. CB and LFP particles are specifically manufactured to have average diameters <1 μm. Nanomaterials play a key role in the improvement of performance and energy density of LIB, since the overall thermal and electric DC conductivity increase with reciprocal particle size [193]. When CB and LFP are dispersed into PDMS at for instance the mentioned viscosity, i.e. 20 $mm^2\ s^{-1}$, by using a dissolver for a certain duration, e.g. >15 min, and various speeds in the range 1500 to 2000 rpm, the majority of the agglomerates are torn apart. This results in a rather homogeneous and arbitrary distribution of the nanoscale particles. Sedimentation at low and even at higher particle suspension fractions was not observable for the dissolved CB and LFP. Experiments were performed with 1 ml of PDMS and 0.5 wt% dispersed CB as well as LFP. Intensity profiles were

measured for more than 65 h, but no sedimentation was observable by MRI. It seems natural, that the counterforce of the liquid restrain the nanoparticles on a large scale. Furthermore, particle diffusion needs to be taken into account on this length scale of particle diameters. Increasing the particle fraction in the suspension only leads to high viscosities and therefore even lower theoretically sedimentation rates. Hence, reasonable limits can be outlined for the presented spin-echo based MRI method: certain viscosities need to be maintained to observe, i.e. meet MRI measurement time resolution with sedimentation time scale. The MRI time scale is thereby given by mainly the repetition time, the number of averages and the number of phase steps which could be reduced to 5-10, leading to a measurement time reduction by a factor of two at least. Furthermore, minimum as well as maximum particle suspension fraction and its PSD needs to be considered. Increasing LFP particle mass fractions in MRI experiments would also increase the effect of signal intensity distortion. Hence, a valuable compromise needs to be achieved.

4.5.2 Sedimentation balance

Supplementing the MRI measurements, suspensions based on PDMS with LFP mass fractions of ϕ_{m}=10 wt%, 30 wt%, and 50 wt% were studied. The measured mass concentration w_i represents the settled mass fraction in relation to the total solid mass in the suspension, i.e. $w_i=\frac{m_i}{m_{\Sigma,solid}}$. In Figure 4.11 the change of w_i over time is shown for LFP slurries of different concentrations as well as a commercial cathode paste. In all cases the slope of the $w_i(t)$ curves decreases with settling time. Larger particles or agglomerates sediment rapidly, resulting in a prompt increase of the settled mass concentration at short measuring times. Homogeneously dispersed particles and small agglomerates sediment at slower rates. The sedimentation behavior, i.e. the decay of the measured mass concentration over time, described by the sedimentation balance is in good agreement with the settling behavior as characterized by the MRI measurements (Figure 4.10), where the settling velocities exponentially decline over time. The slope of the curves at short measuring times (< 1000 s) decreases as the solid content in the suspension increases, suggesting higher settling velocities for diluted LFP suspensions at short measuring times. Furthermore, the total amount of settled LFP particles decreases.

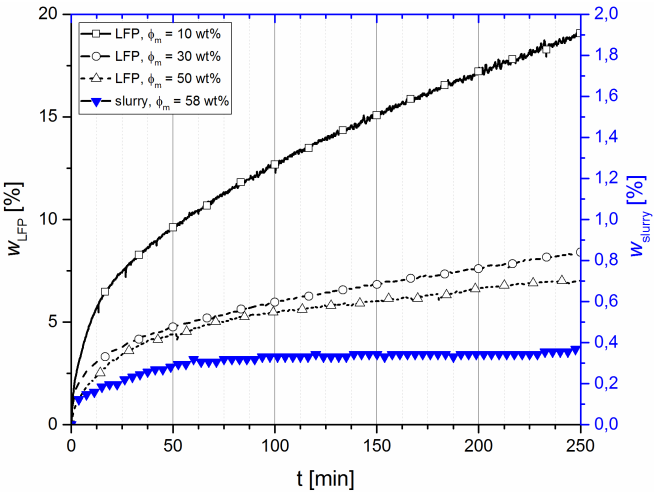

Figure 4.11: Mass concentration profiles over time t for LFP suspensions with particle mass fractions ϕ_m= 10,30,50 wt% measured on a sedimentation balance. The profile of the aqueous cathode slurry including organic additives such as dispersant, binder or thickener and a total suspension mass fraction ϕ_m= 58 wt% shows a very weak increase of measured mass due to the high low shear viscosity of this slurry.

At a particle concentration of 10 wt% the viscosity of the suspension is low enough and particles can settle on the pan. Increasing the solid fraction results in strong increase in viscosity [194–196]. Thus, highly concentrated suspensions show overall lower sedimentation velocities. It should be noted that not all particles settle on top of the pan. In order to avoid contact between the pan and the glass container, the diameter of the pan and the attached filter is slightly smaller than that of the container. Hence, the pan covers 70 % of the total cross section area. Although the LFP particles cannot be measured in their entirety, the differences in measured mass changes are still representative and render a reasonable relative measure of sedimentation behavior.

Regarding the industrial application of the type of suspensions presented in this work, the settling behavior of highly concentrated electrode slurries, including various additives such as binders, dispersants and rheology control agents, is of great interest. Consequently, a water-based cathode slurry with LFP as active material was investigated (Figure 4.11). The sedimentation behavior of the aqueous cathode slurry, i.e. the decay of measured solid mass concentration over time, is similar to that of LFP suspensions. Larger particles and particle agglomerates settled at short time scales, while fine dispersed particles remained suspended. The total amount of settled particles, i.e. the increase of mass concentration w_i, however, is more than one order of magnitude lower compared to the results obtained for LFP suspensions. The electrode slurry consists of active material, carbon black as conductive agent and a polymeric additive. The polymer acts as a dispersing agent for LFP and CB and also as a thickener increasing the viscosity of the continuous phase [130, 138, 197, 198]. Both mechanisms stabilize the

slurry against sedimentation resulting in the much lower weight gain compared to the pure slurries shown in Figure 4.11.

4.6 Conclusion

Spin-echo based MRI experiments were performed to characterize LFP and CB particles in opaque suspensions used for LIB electrodes at a particle mass fraction of ϕ_{p}= 0.5 wt%. The presented method of processing the intensity profiles from the MR images yields good reproducibility throughout the samples. The sedimentation velocity for the two particle classes was derived from the measured evolution of a settling front and modeled by an exponentially decaying function. Detailed insights into the sedimentation of opaque suspensions are provided, since the ^{1}H images uncover the spatial distribution of the particles during sedimentation. Supplementing the MRI experiments, the sedimentation of highly concentrated LFP suspensions was investigated using a self-manufactured sedimentation balance. LFP mass fractions of ϕ_{m}=10,30 and 50 wt% were measured. The time dependent decay of the sedimentation velocity measured by MRI is in good agreement with the increase of the settled mass concentration measured by the gravimetrical method. Inter-particle interactions at higher solid fractions result in a strong increase of the sedimentation viscosity.

Moreover, the sedimentation behavior of an aqueous cathode slurry with LFP as active material and CB as conductive additive was investigated for a realistic and industrially applicable total mass fraction including all components of ϕ_{m}=58 wt%. Although the sedimentation behavior is similar to the one measured for LFP suspensions, the total amount of settled particles is more than one order of magnitude lower. This is attributed to the added polymer serving as a dispersing agent and as a thickener for the continuous phase, thus slowing down sedimentation significantly. Hence, the presented measuring methods provide a reliable combination in order to characterize the sedimentation of opaque suspensions of LFP and CB particles with different particle mass fractions.

4.7 Acknowledgments

The authors would like to thank the German Research Foundation (DFG) for financial support of the instrumental facility Pro^{2}NMR. Furthermore the authors thank the DFG for funding and the cooperative support within *SiMET* (Simulation of mechanical, electrical and thermal properties of Lithium-Ion-Batteries, project number: 281041241/GRK2218). R. Gordon gratefully acknowledges financial support by the *100 prozent erneuerbar Stiftung*.

4.8 Compliance with ethical standards

The authors declare no conflicts of interest.

5 Effect of polymeric binders on dispersion of active particles in aqueous $LiFePO_4$-based cathode slurries as well as mechanical and electrical properties of corresponding dry layers

Full title:	Effect of polymeric binders on dispersion of active particles in aqueous $LiFePO_4$-based cathode slurries as well as mechanical and electrical properties of corresponding dry layers
Authors:	Ronald Gordon, Meriem Kassar, Norbert Willenbacher
Status:	published [199]
Bibliographic data:	ACS Omega 2020, 5, 20, 11455–11465; DOI:10.1021/acsomega.0c00477
Note:	Further permissions related to the excerpted material should be directed to ACS

5.1 Abstract

We investigated the effect of carboxymethyl cellulose (CMC) and the particulate fluorine/acrylate hybrid polymer (FAHP) on the flow behavior of $LiFePO_4$-based cathode slurries as well as on electrical and mechanical properties of the corresponding dry layers. CMC dissolves in water and partly adsorbs on the active particles. Thus, it has a strong impact on particle dispersion and a critical CMC concentration distinguished by a minimum in yield stress and high shear viscosity is found, indicating an optimum state of particle dispersion. In contrast, the nano-particulate FAHP binder has no effect on slurry rheology. Electrical conductivity of the dry layer exhibits a maximum at a CMC concentration corresponding to the minimum in slurry viscosity, but monotonically decreases with increasing FAHP concentration. Adhesion to the current collector is provided by FAHP and the line load in peel tests strongly increases with FAHP concentration, whereas CMC does not contribute to adhesion. The electrical conductivity and adhesion values obtained here excel reported values for similar aqueous $LiFePO_4$-based cathode layers using alternative polymeric binders. Both CMC and FAHP contribute to the cohesive strength of the layers, the contribution of CMC, however, is stronger than that of FAHP, despite its lower intrinsic mechanical strength. We attribute this to

its impact on cathode microstructure since high CMC concentrations result in a strong alignment of $LiFePO_4$ particles, which yields superior cohesive strength.

5.2 Keywords

Lithium-ion battery, water-based cathode, rheological properties, polymer adsorption, mechanical integrity, electrode microstructure

5.3 Introduction

Lithium iron phosphate ($LiFePO_4$) has been extensively investigated for over two decades, since it was reported as a potential cathode material for lithium-ion batteries (LiB) [22]. Its high theoretical capacity (170 $mAhg_{-1}$), stability during charge/discharge, thermal stability, low cost and toxicity, and its environmental compatibility as well as its safety make it a suitable cathode active material for large cell applications [22–27]. However, poor electric conductivity (10^{-9} Scm^{-1}) and a low Li^+-ion diffusion coefficient ($1.8x10^{-18}$ m^2s^{-1}) at room temperature represent intrinsic drawbacks for $LiFePO_4$ as battery cathode material [28–30]. Therefore, considerable research work dealt with the improvement of ionic and electronic conductivity through decrease of particle size, addition of carbon or ion doping [31,33–38,40]. Although the former concept has improved cell performance, agglomeration of $LiFePO_4$ fine particles still constitutes a problem during processing of cathode slurries and limits electrochemical performance of corresponding electrodes.

Conventionally, organic solvents, such as N-methyl-2-pyrrolidone (NMP), are used for dispersing active materials and dissolving polymeric additives for control of processing behavior of the slurry during cathode manufacturing as well as to improve mechanical properties of the dry layer [95, 200, 201]. These solvents are not only environmentally harmful, but also toxic, flammable and expensive. Hence, water-based electrodes have been developed as greener alternative. Several research activities concentrated on exploring novel aqueous binder systems for $LiFePO_4$-based cathodes such as polyacrylic acid (PAA) [202–204], chitosan and its derivatives (CTS, CCTS, CN-CCTS) [127–129,205], poly 4-styrene sulfonic acid (PSSA) [130], styrene butadiene rubber (SBR) [203], poly vinyl acetate (PVAc) [30], polytetrafluorethylene (PTFE) [206], xanthan [132], as well as lithium and sodium salts of carboxymethyl cellulose (LiCMC, NaCMC) [87, 136–138, 207–210].

Carboxymethyl cellulose (CMC) and SBR are often combined as polymeric binders. CMC is a linear, long-chain, anionic polysaccharide, consisting of two anhydroglucose units with three hydroxyl groups each, enabling its solubility in water. SBR is not soluble in water and is, thus, added as nano-particulate dispersion to the slurry. Li and Lin studied the interaction between organic additives and active materials and the resulting electrochemical performance of corresponding cells [87]. Zeta potential and sedimentation measurements of $LiFePO_4$ and carbon black (CB) showed that both, dispersed SBR particles and molecularly dissolved CMC, can adsorb on the solid particles. SBR

showed higher affinity than CMC to adsorb on the $LiFePO_4$ particle surface. Nevertheless, CMC, as a dissociable polyelectrolyte, provided a superior effect on the dispersion of solid particles through electrosteric stabilization.

Instead of SBR, particulate FAHP has been blended with CMC for manufacturing water-based cathodes [211–214]. These studies reported improved coating surface quality and higher adhesive strength between cathode layer and current collector when increasing FAHP concentration. In addition, electrodes based on FAHP show high thermal stability and equivalent electrochemical performance compared to conventionally fabricated NMP-based cathodes. Still, the influence of FAHP on the performance of $LiFePO_4$-based cathodes has not been addressed yet.

Binder properties and concentration not only affect the dispersion behavior of solid particles but also the resulting electrical conductivity of the electrode. Even though the addition of CB particles reduces the electrical resistivity in the electrode layer, particle agglomeration leads to discontinuous conductive pathways. The addition of dispersing polymeric binders at appropriate concentrations and particle to binder ratios results in homogeneous particle distribution and formation of a conducting network, enhancing electron transport kinetics [62,140–142]. As a result, the rate capability of the electrode can be improved, yielding higher cell energy and power as well as enhanced battery lifetime. Furthermore, polymeric binders are of utmost importance for the mechanical integrity of the electrode, determining battery lifetime. The electrode must withstand mechanical stresses due to expansion and shrinkage of the electrochemically active material during charge/discharge cycles [143, 145]. These volume fluctuations can result in delamination of the electrode layer from the current collector and cracking within the layer. Therefore, the determination and improvement of adhesive strength between layer and collector has been thoroughly investigated [123, 129, 148–151]. However, the cohesive strength in the electrode layer has not received much attention. Indentation, tensile, scratch and drag tests have been used to characterize the mechanical strength of electrode layers [151–157,215]. Despite several efforts to bring light into how mechanical properties depend on formulation and slurry processing, the complex contribution of the binder to the processing behavior, mechanical strength, microstructure and electrochemical performance of LiB cathodes still needs in-depth investigation. In preliminary work, we demonstrated that the intrinsic cohesive strength of electrode layers can be characterized using standard methods for mechanical characterization such as compression, flexural, tensile and torsion tests using samples of sufficient thickness. In the present work, the cohesive strength of cathode layers is characterized employing compression tests.

In this study, we first investigate the interaction of CMC and FAHP with $LiFePO_4$ and CB particles, using rheological data of cathode slurries to understand the polymer adsorption behavior. The electrical conductivity of dry cathode layers is determined and correlated to the flow behavior of corresponding slurries to elucidate the relationship between polymer adsorption and component distribution. Moreover, adhesive strength

measurements, and for the first time data regarding the cohesive strength of $LiFePO_4$-based cathodes are presented. Finally, the effect of the polymeric binders on the cathode microstructure is studied and linked to the cohesive strength.

5.4 Experimental

5.4.1 Materials

Needle-shaped $LiFePO_4$ (LFP) particles (Tatung Fine Chemicals Co., Taiwan) with a carbon-coating of 1.5 wt%, a density of 3.5 gcm^{-3}, a specific surface area S_A=11.3 m^2g^{-1} and an equivalent sphere, volume-based average diameter $x_{50,3}$=2.8 μm were used as active material. Carbon black (CB, Alfa Aesar, United States) with a density of 1.73 gcm^{-3} and a specific surface area S_A=70.3 m^2g^{-1} was added as conductivity promoter. According to the manufacturer, the CB particles have a primary particle size $x_{50,3}$=42 nm. However, they agglomerate reaching an average diameter of 5 μm as determined by Fraunhofer diffraction (HELOS H0309, Sympatec GmbH, Germany) equipped with an ultrasonic dispersing unit (QUIXEL, Sympatec GmbH, Germany) used to disperse the particles in ethanol. Carboxymethyl cellulose (Sigma Aldrich, Germany) with a molecular weight M_w=700 kDa and degree of substitution DS=0.9 was used as binder. In addition, an aqueous suspension of 41 wt% fluorine/acrylate hybrid polymer (FAHP, TRD202A, JSR Micro NV., Belgium) with a particle size of 200 nm, a density of 1.2 gcm^{-3}, and a glass transition temperature of -5°C, corresponding to the maximum of the loss modulus G" (Figure 5.1), was added to improve the mechanical strength of the cathode layer. Small amplitude oscillatory shear experiments (Figure 5.1) at fixed frequency covering a broad temperature range from -20°C to 100°C on dry FAHP films did not show a cross-over of the storage (G') and loss (G") moduli in the high temperature range, indicating a high molecular weight of the polymer or even chemical cross-linking. Gravimetric measurements using toluene as solvent yielded a degree of cross-linking of 84.1 ± 3.4 %.

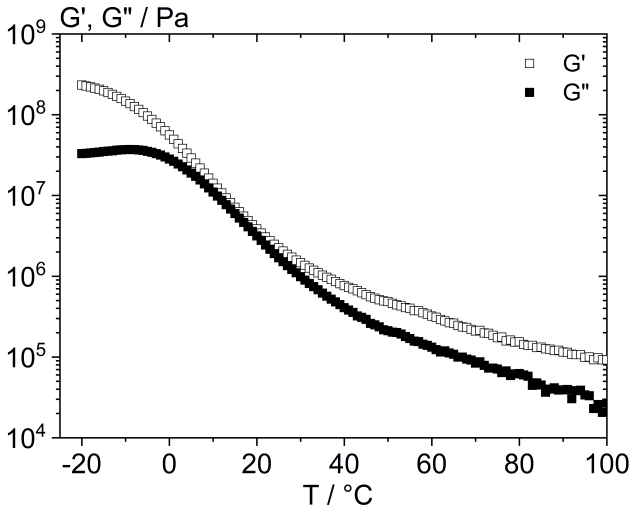

Figure 5.1: Storage (G') and loss (G") modulus of FAHP as a function of temperature. Measurements were performed at constant deformation γ=0.01 % and frequency f=0.1 Hz using films of 0.9 mm height.

5.4.2 Sample preparation

Water based cathode slurries were prepared at constant mixing conditions with a total solids volume fraction ϕ_p=24 vol% at a LFP to carbon black mass ratio of 48:1. The CMC concentration was varied between 1 vol% and 8 vol% referring to the dry electrode layer. First, CMC was dissolved and homogenized in 80 % of the total amount of water needed for the slurry using a 55 mm propeller mixing geometry at 1200 rpm for 25 min. LFP, followed by CB, was dispersed in the CMC-solution using a 50 mm dissolver disk at 2000 rpm for 35 min each. Finally, the remaining amount of water was added and mixed at 2000 rpm for 5 min. For slurries containing FAHP as secondary binder, the polymer suspension was added to the slurry directly after preparing the CMC solution and was homogenized at 1200 rpm for 10 min.

Slurries were coated on glass plates and aluminum foil for electrical conductivity and adhesive strength measurements, respectively, using a doctor blade (ZUA 2000, Zehnther GmbH, Switzerland) with a coating width of 60 mm and a coating gap of 300 μm. The wet films were dried at 80°C for 30 min and then cut into 25 mm width and 60 mm length specimen for the adhesive strength test. To obtain samples for cohesive strength testing, slurries were poured into a 26 mm x 49 mm x 11 mm (WxLxH) silicone mold and dried at 80°C over night. Subsequently, the dry layers were cut and grinded into samples of 2 mm width, 5 mm length and 5 mm height. Sandpaper with rough texture was used to shape the samples and fine sandpaper was applied to smooth the edges.

5.4.3 Sample characterization

Rheological measurements

Rotational steady shear measurements were carried out using a shear stress controlled rheometer (Physica, MCR 501, Anton Paar GmbH, Germany) equipped with a 25 mm plate-plate geometry. The shear stress dependent viscosity $\eta(\tau)$ and the yield stress τ_y were determined applying a stepwise, logarithmic shear stress ramp in the range τ=0.1 Pa to τ=1000 Pa at a gap width of 1 mm. The yield stress τ_y was determined using the tangent intersection point method [216, 217]. The critical stress at which the tangents applied to the linear and flow region of the stress dependent deformation curve cross is defined as τ_y. All measurements were performed at 20°C.

Electrical conductivity tests

The four-point resistivity test was conducted using a customized set-up equipped with four equally spaced measuring probes (S4D5G, Uwe Electronic GmbH, Germany). Five different currents were applied at three different positions of the 60 mm x 120 mm electrode layer. The corresponding voltage was used to calculate the average electrical conductivity according to Smits [218].

Mechanical properties

Mechanical tests were carried out using a universal testing machine (Texture Analyzer, TA.XT plus, Stable Micro Systems, UK) equipped with a 5 kg load cell force sensor (max. force: 50 N, force sensitivity: 1 mN).

The adhesive strength of electrode layers to the aluminum foil was investigated employing 90°-peel-tests based on the standard DIN 28510-1. Therefore, electrode layers with a film thickness between 80 μm and 100 μm were fixed to a measuring plate with the help of double-sided adhesive tape (Universal, Tesa SE., Germany). Subsequently, a 500 g plate was set on top of the electrode layer as a pre-compression step and removed before the measurement to ensure homogeneous contact between adhesive tape and layer. Measurements were performed at a constant peel velocity of 5 mms^{-1} and the measured tensile force F was expressed as line load F/25 mm, characterizing the adhesive strength.

The cohesive strength of thick electrode samples was studied using the compression test based on the standard DIN 51104. Samples were compressed using a steel plate at a constant velocity of 1 mms^{-1} until reaching the breaking point of the samples. Hereby, the maximum compression stress prior to failure $\sigma_{c,max}$ was used to characterize the cohesive strength in the electrode layer. In addition, tensile tests for pure polymers films were carried out at 20°C based on the standard DIN ISO EN 527-4.

Microstructure

The porosity of electrode layers was determined based on the Archimedes density according to the standard DIN 993-1 and DIN 993-18. Additionally, cross-section images of vacuum-infused electrode layers were investigated by means of scanning electron microscopy (SEM) using a LEO1530 microscope (Carl Zeiss AG, Oberkochen, Germany) to characterize their microstructure, particularly the orientation distribution of the needle-shaped $LiFePO_4$ particles.

5.5 Results and discussion

5.5.1 Rheological characterization of cathode slurries

The flow behavior of suspensions well below the maximum packing fraction of the particles is controlled by the viscosity of the disperse phase, the solvent viscosity η_s, the particle volume fraction ϕ_p, size and shape of the particles as well as the interparticle interactions. When attractive particle interactions dominate, the suspensions may exhibit a yield stress τ_y. The absolute value of this quantity is determined by the strength of particle attraction, the number of particle contacts as well as particle size. The high shear limiting viscosity $\eta(\dot{\gamma}\rightarrow\infty)=\eta_\infty$ i.e. when hydrodynamic interactions dominate over thermodynamic particle interactions, solely depends on ϕ_p and η_s. The latter parameter is governed by the type and amount of dissolved polymers. Accordingly, rheological data of $LiFePO_4$/CB slurries with varying amount of added CMC provide insight into the adsorption of the CMC molecules on the particle surface. The fraction of CMC adsorbed on the particles provides steric repulsion superimposing with van der Waals attraction forces and thus affects τ_y. The part of CMC molecularly dissolved in the disperse phase contributes to η_s and hence η_∞.

In the present study, rheological data is used to characterize the influence of CMC on dispersion of $LiFePO_4$ and CB particles in the slurry. Steady shear measurements were carried out to study the flow behavior of cathode slurries at constant solid volume fraction ϕ_p=24 vol% and fixed $LiFePO_4$ to CB ratio 48:1 but varying the CMC concentration ϕ_{CMC}. The viscosity $\eta(\dot{\gamma})$ of cathode slurries decreases with increasing CMC amount, reaching a minimum at a critical concentration and increases upon further addition of CMC (see supporting information).

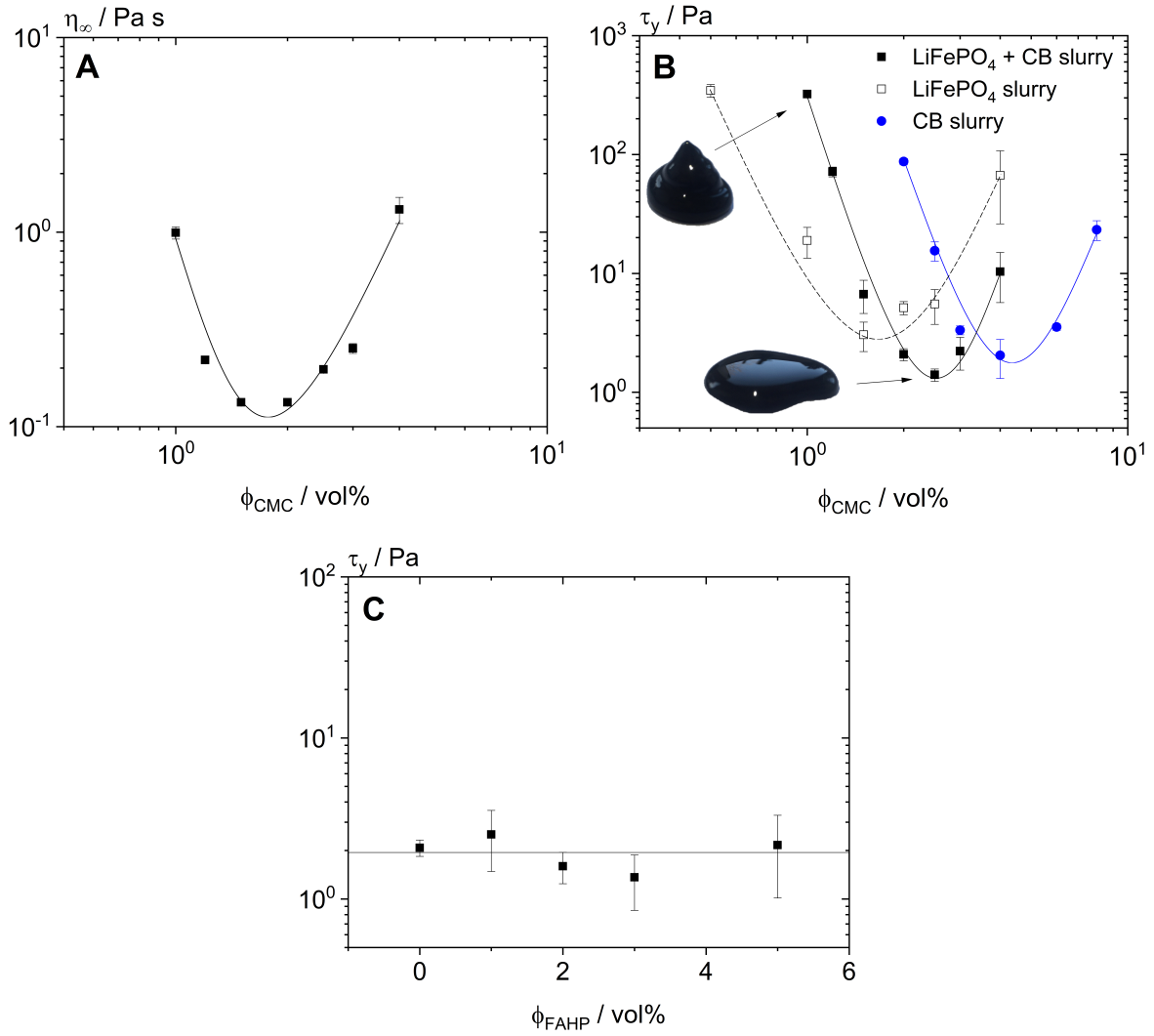

Figure 5.2: High shear viscosity $\eta_\infty=\eta(\dot{\gamma}=800\ s^{-1})$ against the CMC concentration of cathode slurries (A). Yield stress of cathode slurries with/without CB and of CB slurries as a function of ϕ_{CMC} (B). Yield stress of cathode slurries including CB at constant ϕ_{CMC}=2 vol% as a function of ϕ_{FAHP} (C). $LiFePO_4$ slurries and cathode slurries including $LiFePO_4$ and CB were investigated at a constant ϕ_p=24 vol% and constant $LiFePO_4$ to CB mass ratio 48:1. CB slurries were studied at constant ϕ_p=3.5 vol%. Note, ϕ_{CMC} and ϕ_{FAHP} refer to the polymer concentration in the dry electrode.

This effect can be observed more clearly by plotting the high shear viscosity $\eta_\infty=\eta(\dot{\gamma} = 800\ s^{-1})$ against ϕ_{CMC} as shown in Figure 5.2A. The high shear viscosity exhibits a pronounced minimum as a function of CMC concentration. This can be rationalized as follows: without CMC or at low CMC concentration, van der Waals attraction among particles dominates and aggregates are formed which are stable even when exposed to high shear forces. These aggregates immobilize part of the solvent and hence the ef-

fective particle volume fraction exceeds ϕ_p and this results in high values of η_∞. As more and more CMC adsorbs on the particles, electrosteric repulsion partly prevents aggregation and thus η_∞ decreases until the particles are fully dispersed or the particle surfaces are saturated with CMC. Further addition of CMC then leads to an increase in η_∞ due to the contribution of the dissolved polymer to the viscosity of the continuous phase η_s. Our results demonstrate that in the investigated cathode slurries CMC acts as a dispersing agent at low concentration but as a thickener at high polymer fraction. Note, a non-adsorbing polymer would cause a monotonic increase in η_∞ with increasing polymer concentration as a result of a progressive enhancement of η_s. A similar change in rheological properties upon addition of CMC was observed for graphite-based LiB anode slurries [139]. However, the implications of this effect on further electrode properties were not discussed.

The adsorption of CMC on the active material and conductive agent particle surface and hence its impact on particle dispersion also shows up in the yield stress of the slurry, i.e. the stress at which plastic deformation starts. Slurries comprising only $LiFePO_4$ or CB, respectively, were investigated to systematically understand the adsorption behavior of CMC on both particle species. Figure 5.2B displays the yield stress as function of ϕ_{CMC} for $LiFePO_4$ and CB based slurries as well as cathode slurries including both components. Note, slurries containing only CB as solid particles were characterized at a constant solid volume fraction ϕ_p=3.5 vol%. All slurries exhibit a pronounced minimum in τ_y vs. ϕ_{CMC} and the yield stress drops by about two orders of magnitude. The yield stress in such slurries is a signature of a percolating particle network self-assembling due to the pre-dominantly attractive particle interactions, its absolute value is determined by the strength of the attractive force and the number of particle contacts per volume. The initial decrease of τ_y with increasing ϕ_{CMC} is a consequence of the increasing electrosteric repulsion among particles due to the adsorbed CMC partially compensating the strong van der Waals attraction. The minimum of the $\tau_y(\phi_{CMC})$ curve corresponds to safely measurable absolute values $\tau_y \approx$1-2 Pa. This indicates that a weak particle network exists even in the presence of a CMC adsorption layer. From the radius of gyration R_g=153 nm for the CMC used here dissolved in water [219], we estimate a thickness of the CMC adsorption layer in a similar range which is not sufficient for a full stabilization of the $LiFePO_4$ particles with $x_{50,3}$=2.8 μm. The increase in τ_y upon further addition of CMC is attributed to a depletion attraction among particles induced by the non-adsorbing fraction of CMC molecules freely diffusing in the solvent. This is consistent with the increase in η_∞ observed in the same concentration range as discussed above (see Figure 5.2A).

FAHP as a particulate secondary polymeric binder was added to the cathode slurries to improve the adhesive strength between electrode layer and current collector. The rheological properties of these slurries were investigated to understand the influence of FAHP on the flow behavior. Therefore, cathode slurries at constant ϕ_p=24 vol% and $LiFePO_4$ to CB volume ratio were characterized at constant ϕ_{CMC}=2 vol% but varying FAHP concentration ϕ_{FAHP}. The chosen CMC concentration corresponds to

the critical concentration, at which rheological parameters yield a minimum, to ensure optimum particle dispersion. Figure 5.2C displays the yield stress as a function of the FAHP concentration and clearly shows that the addition of the secondary polymer has no effect on particle aggregation. Furthermore, η_∞ is also independent of ϕ_{FAHP} (see supporting information), demonstrating that this polymer added in form of cross-linked nanoparticles does not affect the flow behavior of the slurry. The contribution of the FAHP particles to the overall volume fraction is negligible in comparison to that of the $LiFePO_4$ and CB particles and moreover, it obviously does not affect the dispersion state of these components. To further confirm this, we prepared cathode slurries with ϕ_{FAHP}=1 vol% but varying CMC concentration. Within experimental error these slurries exhibited the same yield stress as the corresponding slurries without FAHP and the same is true for the high shear viscosity (see supporting information). These results confirm that FAHP neither affects particle network formation nor the flow behavior of the slurries. These properties are essentially controlled by CMC.

5.5.2 Electrical conductivity of cathode layers

Particle dispersion in the dry electrode layer strongly affects the electrical conductivity of the electrode and cell resistivity. The electrical conductivity of thin cathode layers made from the slurries investigated above will be discussed next. Figure 5.3A displays the electrical conductivity of cathode layers with and without CB as a function of ϕ_{CMC}. Cathode layers including CB yield, as expected, overall higher conductivity values than CB-free cathode layers, confirming that the addition of CB is crucial for cathodes electrical conductivity. The electrical conductivity of cathode layers including CB is almost three times higher than for cathode layers made from LFP alone. For cathode layers with or without CB, the electrical conductivity exhibits a maximum with increasing CMC concentration and decreases at higher ϕ_{CMC}. The CMC concentration, at which the maximum conductivity value is reached, correlates to the critical concentration, at which the minimum τ_{y} was obtained for corresponding cathode slurries. This clearly confirms that the CMC has a strong impact on particle distribution and microstructure of the wet slurry as well as the dry cathode layer. A similar effect of a polymeric additive on electrical properties of cathode layers has been observed earlier. Li et al. reported a minimum of the surface resistance upon variation of poly-4-styrene sulfonic acid (PSSA) concentration in $LiFePO_4$ based layers [130]. This effect was attributed to improved particle distribution due to electrosteric repulsion between particles with adsorbed PSSA. However, the minimum in surface resistance did not systematically correlate to the corresponding rheological findings. Furthermore, it is unclear whether the observed effect on surface resistance is directly caused by PSSA or by further interactions in the cathode slurry since several polymeric additives were used for sample preparation. Interestingly, the maximum value obtained here is nearly twice as high as for optimized layers including specially designed conduction-promoting agents [129].

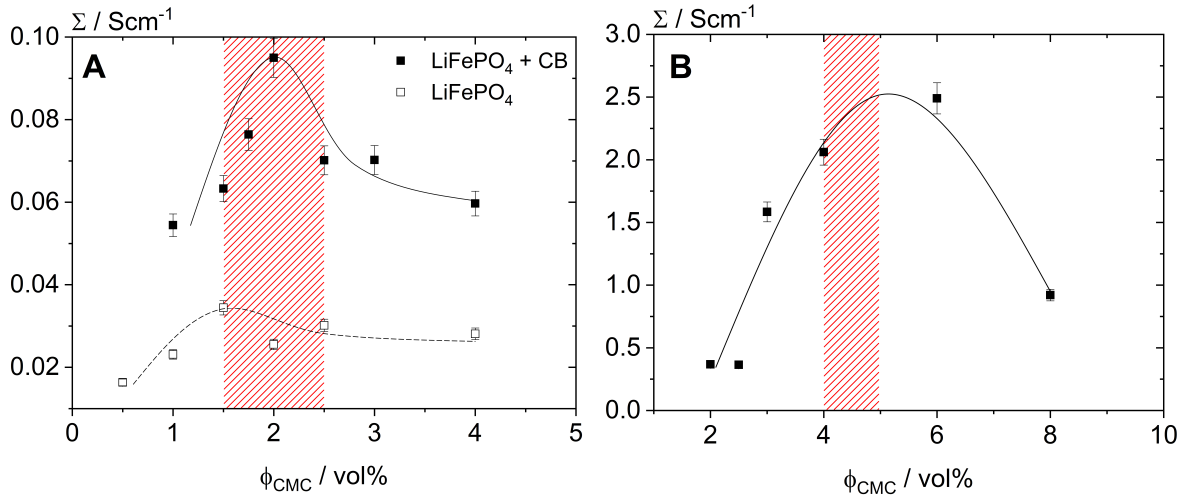

Figure 5.3: Electrical conductivity of dry cathode layers with and without CB (A) as well as of CB layers (B) as a function of ϕ_{CMC}. The CMC concentration range, in which the corresponding minimum value of τ_y is obtained, is marked in red. Lines are drawn to guide the eye. The standard deviation for conductivity data was determined for three independently prepared samples.

The influence of CMC concentration on the electrical conductivity of CB layers is shown in Figure 5.3B. As expected, the absolute conductivity values are significantly higher than that of cathode layers including $LiFePO_4$. Analog to layers containing $LiFePO_4$, the electrical conductivity increases with increasing ϕ_{CMC}, again reaching a maximum at a critical concentration, which correlates to the minimum of τ_y for corresponding CB slurries (see Figure 5.2B). Higher CMC concentrations lead to a decrease of electrical conductivity since the polymer not adsorbed to the particle surface is randomly distributed in the dry films. This obviously deteriorates and interrupts conductive pathways.

Figure 5.4A shows the electrical conductivity of dry cathode layers including CB at constant ϕ_{CMC}=2 vol% but varying ϕ_{FAHP}. Increasing FAHP concentration leads to a monotonic decrease of the electrical conductivity. Rheological characterization of corresponding cathode slurries did not show a change of yield stress upon variation of ϕ_{FAHP}, i.e. the FAHP particles hardly affect the network of $LiFePO_4$ and CB particles. Consequently, we conclude that, the decay in electrical conductivity must be attributed to the randomly distributed FAHP in the dry cathode layer, deteriorating electron transport.

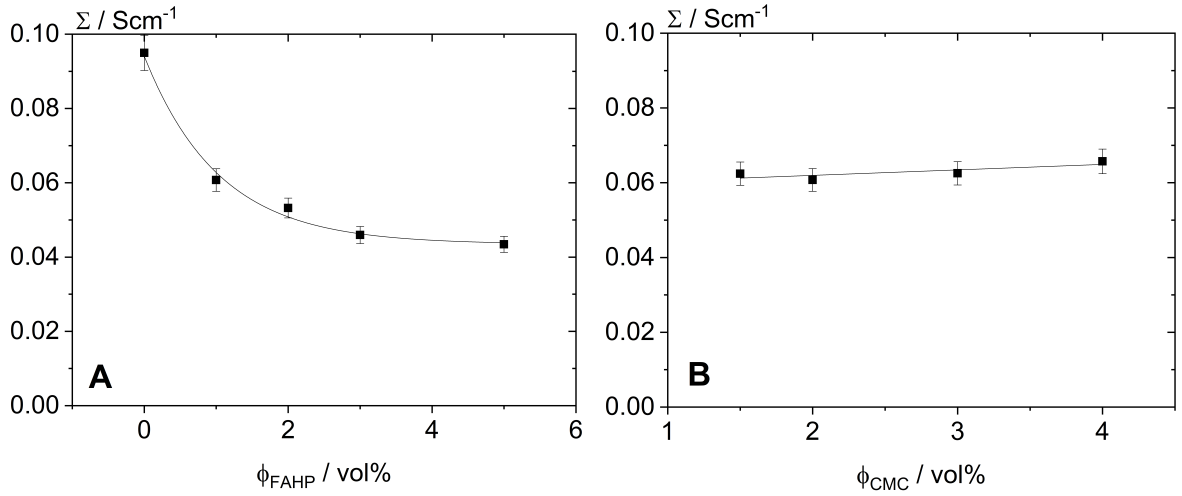

Figure 5.4: Electrical conductivity of dry cathode layers including CB at constant ϕ_{CMC}=2 vol% over ϕ_{FAHP} (A) as well as of dry cathode layers including CB at constant ϕ_{FAHP}=1 vol% as a function of ϕ_{CMC} (B). The standard deviation for conductivity data was determined for three independently prepared samples.

The electrical conductivity of cathode layers including CB and constant ϕ_{FAHP}=1 vol% hardly varies with ϕ_{CMC} as displayed in Figure 5.4B. Irrespective of CMC concentration, the addition of FAHP seems to deteriorate the conductive network. Even though the addition of FAHP exhibits no effect on rheological properties and hence the microstructure of cathode slurries, its presence in the dry layer affects the electrical properties adversely.

5.5.3 Mechanical properties of cathode layers

Adhesion

Peel tests performed for pure CMC films on aluminum foil yielded an average line load of 2.8 ± 0.8 Nm^{-1}, i.e. the intrinsic contribution of CMC to the adhesive force between electrode layer and current collector is limited by this value. The effect of polymer addition on the adhesive strength between cathode layers and aluminum foil was also determined using this method.

Figure 5.5 displays the measured line load of cathode layers as a function of ϕ_{CMC} as well as of cathode layers including ϕ_{CMC}=2 vol% as function of ϕ_{FAHP}. The line load of samples without FAHP is essentially independent of ϕ_{CMC} and on a technically inacceptable low level around 0.8 Nm^{-1}. Obviously, a second polymer is required to achieve a technically feasible level of adhesion. It should be noted that the presence of CB in the electrode layer has no effect on the line load irrespective of ϕ_{CMC} (see supporting information).

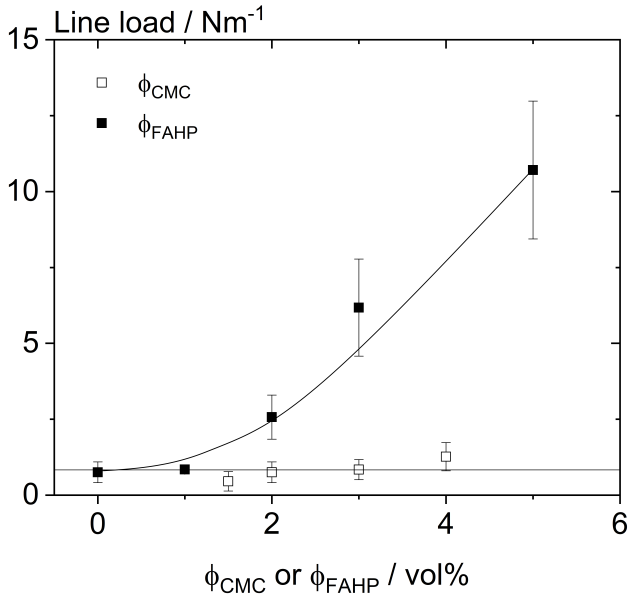

Figure 5.5: Line load for dry cathode layers without FAHP over ϕ_{CMC} as well as for cathode layers including constant ϕ_{CMC}=2 vol% as a function of ϕ_{FAHP}.

Here we have employed FAHP as secondary polymeric binder. The adhesive strength between pure FAHP films and aluminum foil is characterized by an average line load of 600 ± 50 Nm^{-1}, confirming the high potential of FAHP as adhesion promoter for battery electrode layers. As expected, higher ϕ_{FAHP} leads to higher values of the line load, indicating a substantial improvement of the adhesive strength between layer and current collector. The line load of the investigated samples increases monotonically with increasing ϕ_{FAHP}, reaching over 10 times the value of the reference sample without secondary polymer at ϕ_{FAHP}=5 vol%. Nevertheless, this value is still well below the theoretical limit assuming that 5 vol% of the contact area are covered with polymer. The improvement of adhesive strength due to addition of FAHP comes at cost of the electrical conductivity of the cathode layer (see Figure 5.4A). A FAHP concentration of 5 vol%, necessary to achieve an adhesive strength of 10 Nm^{-1}, results in a drop of electrical conductivity from 0.09 Scm^{-1} to 0.04 Scm^{-1}. However, both, electrical conductivity and adhesion strength values, still prove to be slightly higher than values reported for similar aqueous $LiFePO_4$-based cathode layers using carboxymethyl/chitosan, CMC/SBR or xanthan as polymeric binders [129, 132].

Cohesion

Previously we could show that compressive strength tests on thick anode layers yield reliable and reproducible results, rendering this method suitable for characterization of the cohesive strength of electrode layers. It should be noted that sample porosity has a strong impact on compressive strength. All samples investigated here, however,

were confirmed to have a porosity of 60 ± 2%, so this aspect does not need further consideration here.

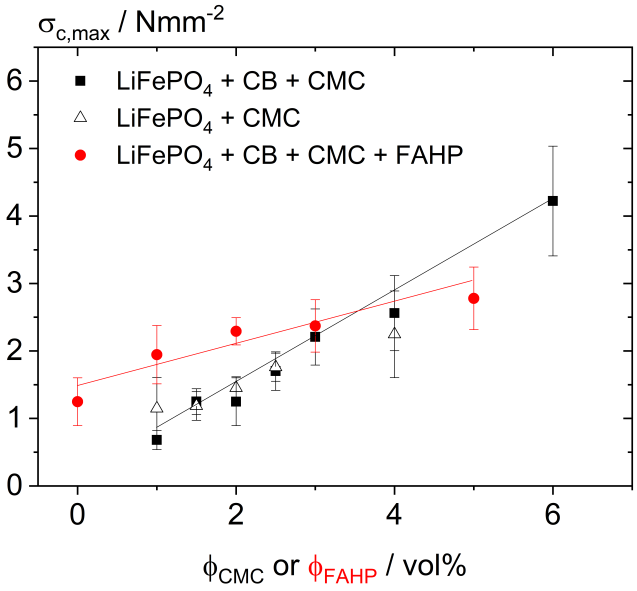

Figure 5.6: Maximum compressive strength of thick cathode layers with and without CB as a function of ϕ_{CMC} as well as of cathode layers including CB and ϕ_{CMC}=2 vol% as a function of ϕ_{FAHP}.

The cohesive strength of thick cathode layers was determined accordingly focusing on the effect of the added polymer. The intrinsic mechanical strength of the added polymers was determined employing tensile tests. Measurements at constant test conditions yield fracture stress values of 35.9 ± 5.2 Nmm^{-2} and 19.6 ± 3.6 Nmm^{-2} for FAHP and CMC films, respectively. Figure 5.6 shows the critical compressive stress at which the sample structure collapses as a function of ϕ_{CMC} for cathode layers with/without CB and as a function of ϕ_{FAHP} for cathode layers including CB and constant ϕ_{CMC}=2 vol%. The compressive strength increases almost linearly with increasing ϕ_{CMC} and CB has essentially no effect on the sample failure. This linear relationship apparently does not depend on whether the CMC is adsorbed on the particles or dissolved in the continuous phase of the slurry. Variation of FAHP concentration at fixed ϕ_{CMC}=2 vol% also yields a linear relationship between $\sigma_{c,max}$ and polymer concentration. Despite its higher intrinsic mechanical strength, however, the slope of the $\sigma_{c,max}$ vs. ϕ_{FAHP} regression line is only about half that of the $\sigma_{c,max}$ vs. ϕ_{CMC} curve. Furthermore, comparing data at a given total binder concentration ϕ_{CMC} or (ϕ_{CMC} + ϕ_{FAHP}) of e.g. 6 vol% yields an about 50 % higher $\sigma_{c,max}$ value for the layer including only CMC as binder relative to the layer including 2 vol% CMC and 4 vol% FAHP. Obviously, FAHP provides less cohesive strength compared to CMC than theoretically expected. We assume that this is related to the different effect of both binders on the microstructure, i.e. the state of dispersion and orientation of the particulate active material. As discussed above, CMC

dissolved in the aqueous phase and partly adsorbing on the surface of the $LiFePO_4$ or CB particles has a distinct effect on the microstructure of the slurry, while this is not the case for FAHP (see Figure 5.2). We hypothesize that CMC also has a strong effect on the structure of the dry electrode layer. This will be discussed in the next section based on image analysis of scanning electron micrographs.

Cathode microstructure

Porosity of cathode layers including only CMC or a combination of CMC and FAHP as binder system did not depend on polymer concentration and exhibited values in the range of 58% – 60% and 60% – 62%, respectively. SEM images of cathode layers were taken to investigate their microstructure in more detail. Therefore, individual $LiFePO_4$ particles and particle collectives were detected and their angle of orientation in relation to a centered coordinate system was analyzed. Figure 5.7A and B show SEM micrographs of cathode layers including ϕ_{CMC}=1.5 vol% and ϕ_{CMC}=6 vol%, respectively. The red lines denote the particle orientation in relation to the centered coordinate system marked in white. The particle frequency was then plotted over the angle of orientation for the corresponding cathode layers as shown in Figure 5.7C and D. Cathodes including low CMC concentration exhibit a random particle orientation, whereas corresponding cathodes with high CMC concentration show a clear particle alignment as indicated by broad and narrow distribution of the particle frequency, respectively. A similar behavior was found for cathode layers including FAHP and CMC as binder system. Cathode layers with 2 vol% CMC and 5 vol% FAHP exhibit a broad distribution of the particle orientation, indicating an isotropic layer microstructure (Figure 5.7E). In contrast, samples with ϕ_{CMC}=4 vol% and ϕ_{FAHP}=1 vol% exhibit a preferred particle orientation of 70° - 100° (Figure 5.7F). This aligned microstructure configuration seems to correlate to the high cohesion values obtained for corresponding cathode layers shown in Figure 5.6.

Compression tests showed a slight increase of cohesive strength when increasing ϕ_{FAHP}. However, the addition of FAHP has no influence on particle orientation (compare Figure 5.7C and E). We attribute the increment in cohesive strength upon addition of FAHP to the superior intrinsic mechanical properties of FAHP. However, CMC yields additional cohesive strength through particle alignment in the electrode, despite its minor mechanical strength compared to FAHP.

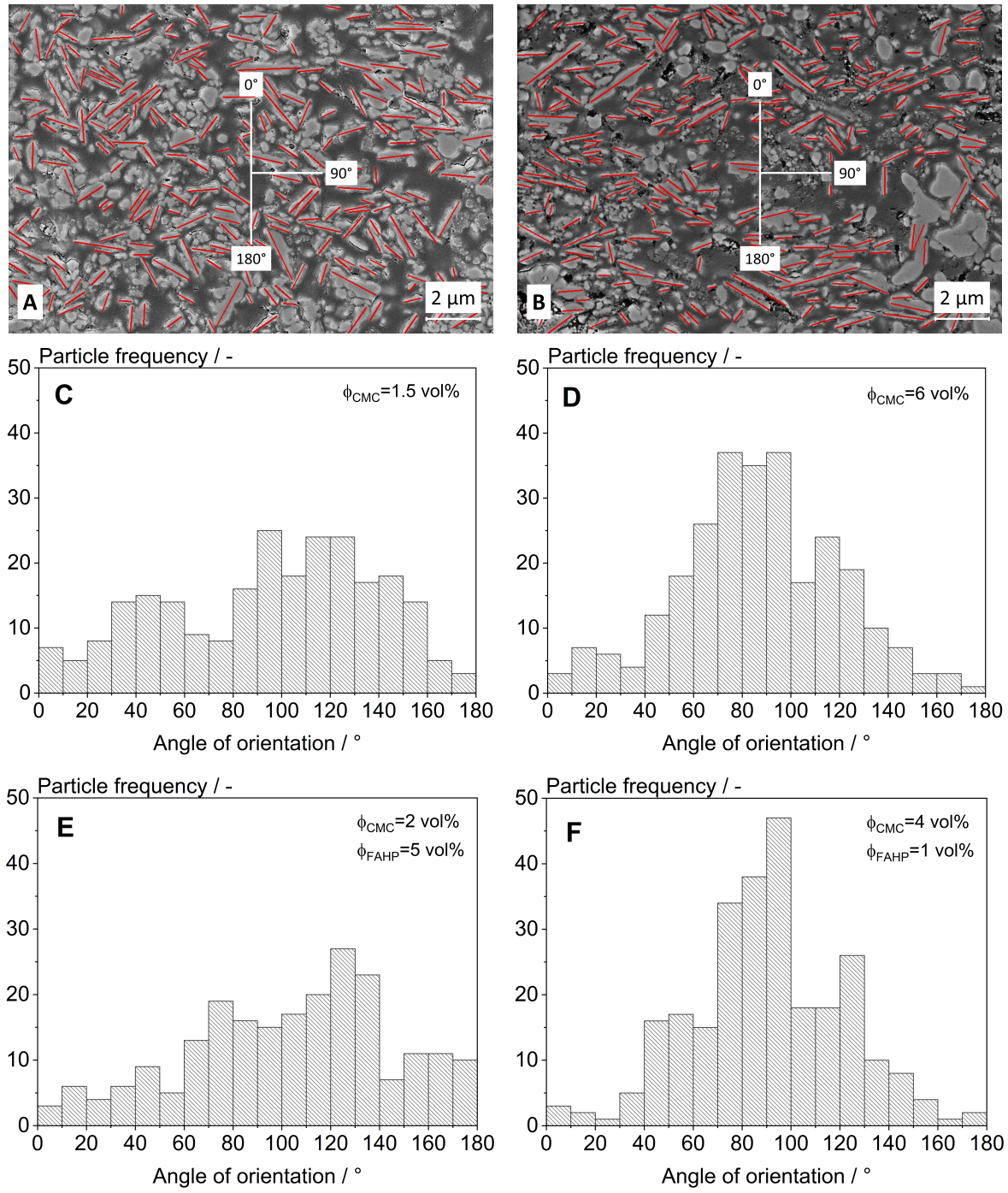

Figure 5.7: Particle orientation in electrode layers. SEM image of layer including ϕ_{CMC}=1.5 vol% (A) and ϕ_{CMC}=6 vol% (B). Particle frequency as a function of angle of orientation for electrode layers including ϕ_{CMC}=1.5 vol% and ϕ_{FAHP}=0 vol% (C), ϕ_{CMC}=6 vol% and ϕ_{FAHP}=0 vol% (D) ϕ_{CMC}=2 vol% and ϕ_{FAHP}=5 vol% (E) as well as ϕ_{CMC}=4 vol% and ϕ_{FAHP}=1 vol% (F).

5.6 Conclusions

In this study, we comprehensively studied the role of CMC and FAHP as polymeric binders for Li-ion battery cathodes made from water-based slurries of $LiFePO_4$ and CB. The volume fraction of active materials was kept constant and the concentration of CMC and FAHP was systematically varied in a wide range. We investigated not only the effect of these polymers on particle aggregation and flow behavior of the wet slurries, but also their impact on electrical conductivity, as well as adhesive and cohesive properties of dry layers and finally also the microstructure of these layers in terms of particle orientation obtained from SEM micrograph image analysis.

Shear rheometry revealed that the yield stress as well as the high shear viscosity exhibit a pronounced minimum at a critical CMC concentration. The decrease of τ_y and η_∞ at low ϕ_{CMC} is attributed to the adsorption of the polymer on the particle surface weakening the particle network present in the slurry due to the electrosteric repulsion partly compensating the strong van der Waals attraction among particles. In this concentration range CMC improves particle dispersion but even at the CMC concentration corresponding to the minimum in τ_y and η_∞ a weak percolating particle network exists. At higher CMC concentrations, when particle surfaces are saturated, the polymer dissolved in the continuous, aqueous phase leads to an increase in τ_y presumably caused by attractive depletion interactions among particles and to an increase of η_∞ due to the thickening capacity of the increasing fraction of polymer chains dissolved in the aqueous phase. In contrast to CMC, the FAHP added in form of crosslinked nanoparticles has no significant effect on active particle dispersion and flow behavior of the slurries, as expected.

Films including CB exhibit a much higher conductivity than those without this additive emphasizing the prominent role of this additive for the electrical properties of the battery electrodes. However, the electrical conductivity Σ of cathode layers significantly varies with type and amount of added binder. Upon variation of CMC concentration, Σ exhibits a pronounced maximum at a critical ϕ_{CMC} close to that at which η_∞ and τ_y of the slurry exhibit a minimum, i.e. when the optimum particle dispersion is reached. In contrast, conductivity monotonically decreases with increasing FAHP concentration probably reaching a limiting value for $\phi_{FAHP} > 5$ vol%.

As expected from the low intrinsic adhesion of CMC to aluminum, the adhesion of cathode layers including CMC as the only polymeric binder to the current collector is on a technically inacceptable, low level. FAHP, however, has a high affinity to aluminum and hence the adhesive strength of cathode layers to the current collector increases monotonically with increasing ϕ_{FAHP}. Absolute values 10 times higher than without that secondary polymer are reached for $\phi_{FAHP} > 5$ vol%, however, at the expense of a loss in electrical conductivity as discussed above and still the adhesion is weaker than theoretically expected based on the adhesive strength of the pure polymer.

We have systematically investigated the cohesive strength of cathode layers here for the first time based on compression tests performed on thick films with similar porosity and microstructure as the thin cathode layers. Compressive strength increases linearly with increasing ϕ_{CMC} or ϕ_{FAHP}. Despite its lower intrinsic cohesive strength, this increase in cathode layer cohesion is more pronounced with added CMC than with FAHP. Microstructural investigations based on image analysis of SEM micrographs revealed that CMC has a strong effect on particle orientation with pronounced particle alignment at high ϕ_{CMC}. On the other hand, a random particle orientation is found when FAHP is added, irrespective of concentration. This different impact of the investigated polymers on microstructure and particle orientation seems to be the origin of the strong contribution of CMC to the cohesive strength of the cathode layers.

5.7 Author contributions

The manuscript was written through contributions of all authors. All authors have given approval to the final version of the manuscript. These authors contributed as follows: R.G. contributed in the conceptualization, methodology, formal analysis, investigation, writing the original draft, and visualization, M.K. in the methodology, formal analysis, and investigation, and N.W. in writing - review and editing and supervision.

5.8 Acknowledgments

R. Gordon gratefully acknowledges financial support by the 100 prozent erneurbar Stiftung. We acknowledge support by the KIT-Publication Fund of the Karlsruhe Institute of Technology.

5.9 Supporting Information

Rheological characterization of cathode slurries

Figure 5.8 shows the viscosity of cathode slurries against the shear rate for different ϕ_{CMC}. The viscosity decreases with increasing CMC amount, reaching a minimum at a critical concentration and increasing with further addition of CMC. Figure 5.9 shows the high shear viscosity of cathode slurries including 2 vol% CMC over the FAHP concentration. The variation of ϕ_{FAHP} does not have a significant effect on the flow behavior of the slurry. Figure 5.10A and B display the high shear viscosity and yield stress, respectively, of cathode slurries with and without addition of FAHP as secondary polymer. Slurries including 1 vol% FAHP show similar high shear viscosity to those without the secondary polymer.

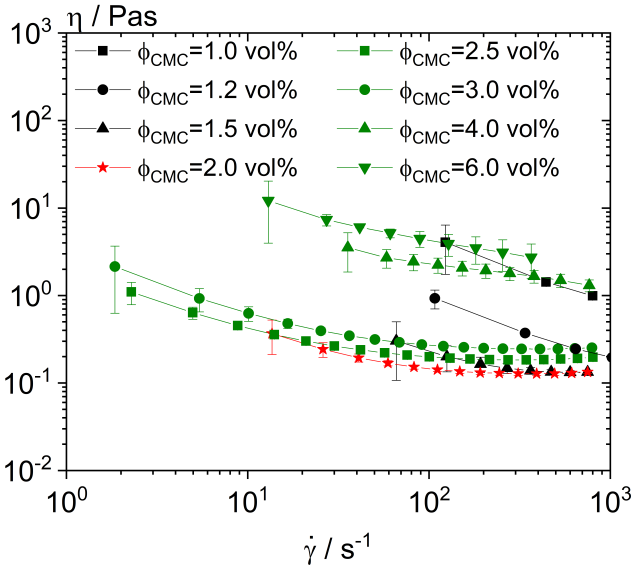

Figure 5.8: Viscosity as a function of shear rate for cathode slurries including different CMC concentrations at constant solid volume fraction ϕ_p=24 vol% and constant $LiFePO_4$ to CB mass ratio 48:1. Note, ϕ_{CMC} refers to the CMC concentration in the dry electrode.

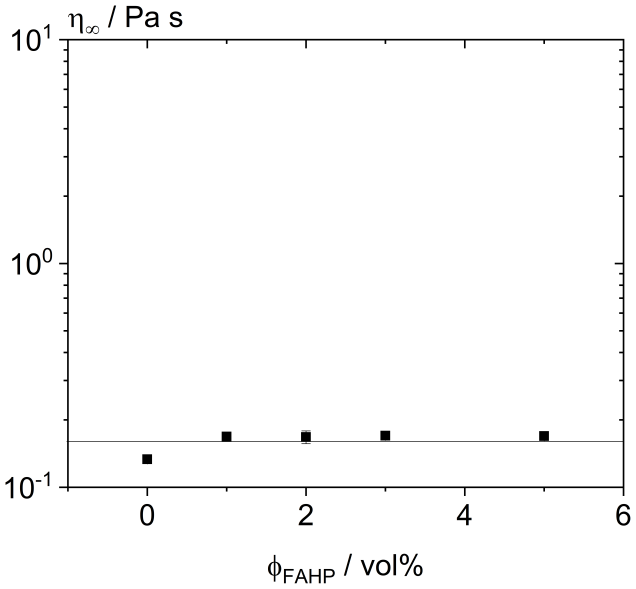

Figure 5.9: High shear viscosity $\eta_\infty=\eta(\dot{\gamma}=800\ s^{-1})$ as a function of FAHP concentration for cathode slurries including 2 vol% CMC at a constant volume fraction of ϕ_p=24 vol% and constant $LiFePO_4$ to CB mass ratio 48:1. Note, ϕ_{FAHP} refers to the FAHP concentration in the dry electrode.

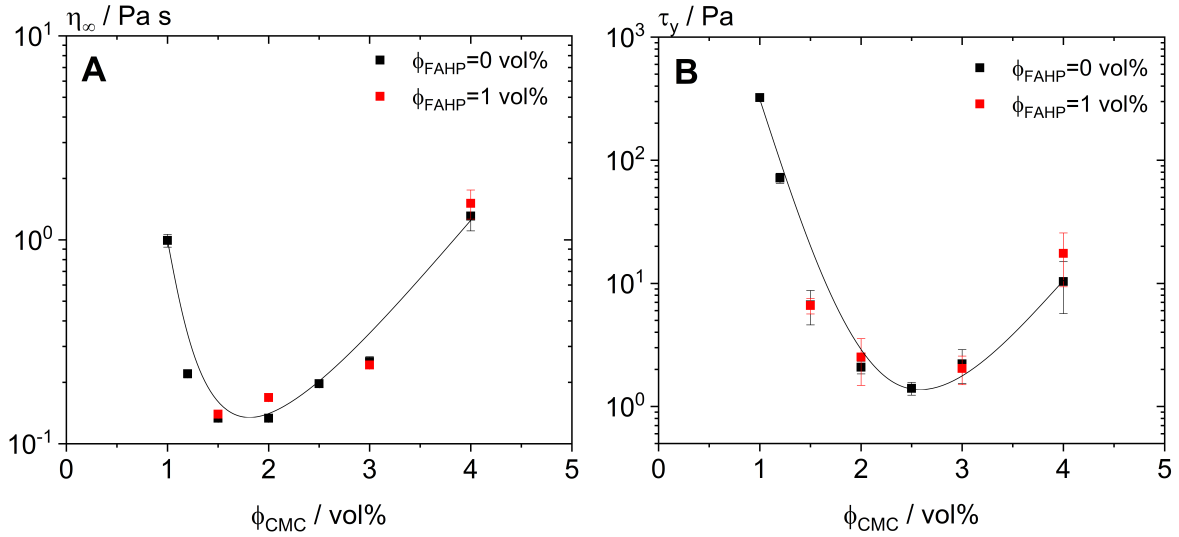

Figure 5.10: High shear viscosity $\eta_\infty = \eta(\dot{\gamma}=800\ s^{-1})$ (A) and yield stress (B) as a function of the CMC concentration for cathode slurries with and without FAHP at a constant volume fraction ϕ_p=24 vol% and constant $LiFePO_4$ to CB mass ratio 48:1. Note, ϕ_{CMC} and ϕ_{FAHP} refer to the polymer concentration in the dry electrode.

Mechanical properties of cathode layers - Adhesion

Figure 5.11 displays the line load of dry cathode layers with and without CB as a function of CMC concentration. The presence of CB in the electrode has no effect on the adhesive strength irrespective of ϕ_{CMC}.

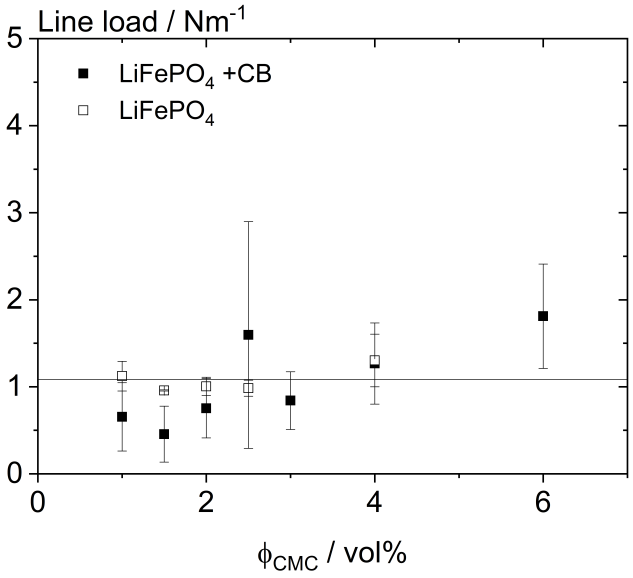

Figure 5.11: Line load of dry cathode layers with and without CB as a function of CMC concentration.

6 Effect of carboxymethyl cellulose on the flow behavior of lithium-ion battery anode slurries and the electrical as well as mechanical properties of corresponding dry layers

Full title:	Effect of carboxymethyl cellulose on the flow behavior of lithium-ion battery anode slurries and the electrical as well as mechanical properties of corresponding dry layers
Authors:	Ronald Gordon, Raquel Orias, Norbert Willenbacher
Status:	published [220]
Bibliographic data:	J Mater Sci (2020) 55:15867–15881; DOI: 10.1007/s10853-020-05122-3

6.1 Abstract

We present a holistic view on the role of polymeric binders in waterborne LiB anodes, including preparation and processing of wet slurries as well as microstructure, electrical conductivity and mechanical integrity of dry electrode layers. We focus on carboxymethyl cellulose (CMC), with respect to technical application the influence of soft, nano-particulate styrene-butadiene rubber (SBR) as secondary binder is also addressed. We discuss the influence of CMC concentration, molecular weight (M_w) and degree of substitution (DS) on flow behavior of anode slurries. Rheological data are not only relevant for processing, here we use them to characterize the adsorption of CMC on active material particles and dispersion of these particles in the slurry at technically relevant concentrations. The fraction of CMC adsorbed onto graphite particles increases with increasing M_w and decreasing DS. Electrical conductivity increases with M_w, i.e. with decreasing free polymer deteriorating conductive carbon black pathways. CMC does not contribute to the adhesion of electrode layers, irrespective of M_w, or DS, technically feasible adhesion is inferred by SBR. Cohesive strength of anode layers, determined here for the first time under well-defined mechanical load, increases with increasing M_w and decreasing DS, i.e. with increasing fraction of adsorbed CMC and corresponding improved particle dispersion. Strong adhesion and high electrical conductivity are correlated to an alignment of graphite particles as revealed by electron microscopy, presumably enabled by higher particle mobility in well-dispersed slurries. Accordingly, targeted choice of

CMC is a valuable means to control processing, electrical conductivity and mechanical strength of LiB electrodes.

6.2 Keywords

Lithium-ion battery, water-based anode, rheological properties, polymer adsorption, mechanical integrity, electrode microstructure.

6.3 Introduction

Lithium-ion batteries (LiB) play an important role as electrochemical energy storage systems. They combine high energy and power density, making them suitable for portable electronics, hybrid/full electric vehicles and grid applications [3–5, 16, 165]. So far, research mainly focused on the development of new electrochemically active materials to achieve high cell performance [118–120, 221, 222]. In contrast, little attention has been paid to the role of binders not only for processing but also for the performance of LiB. As electrochemically inactive material, poly (vinylidene fluoride) is one of the most widely used polymeric binders for LiB electrodes. Conventionally, these binders are dissolved in organic solvents, such as N-methyl-2-pyrrolidone (NMP) [223, 224]. Since organic solvents are typically environmentally unfriendly and flammable, safety concerns and high cost are associated to their use in LiB production, particularly for the upcoming high-volume mass production of electric vehicles. Therefore, water-based electrodes have been developed as promising environmentally benign alternative [225, 226].

Carboxymethyl cellulose (CMC) and styrene butadiene rubber (SBR) are often combined as additives for aqueous anode slurries to achieve high stability and processability as well as superior electrochemical cell performance [135, 227, 228, 228–230]. The present investigation focuses on CMC as binder. Additionally, nano-scale SBR particles are added during slurry preparation since this soft, rubber-like polymer is necessary to provide a technically feasible adhesion to the current collector. CMC is a linear, long-chain, water-soluble, anionic polysaccharide, consisting of two anhydroglucose units (β-linked glucopyranose residues) with three hydroxyl groups each. The hydrogen in the hydroxyl groups can be substituted by a carboxymethyl group (-OCH2COO-). The average number of substituted hydroxyl groups per anhydroglucose unit is defined as the degree of substitution (DS) and hence has a maximum of 3. Rheological properties of CMC solutions strongly depend on concentration, molecular weight (Mw), DS and pH [80–85]. This also shows up in the flow behavior of battery electrode slurries. Beyond that, however, the interaction with other components in these slurries has to be considered. Lee et al. investigated the effect of CMC DS on the dispersion of graphite particles and the resulting electrochemical performance of corresponding anodes [231]. CMC with lower DS adsorbed preferentially on graphite, dispersing the particles and stabilizing the slurry against sedimentation through repulsive electrosteric interparticle forces. As a result, longer cycle life and improved electrochemical cell performance was achieved using low substituted CMC. Other studies have shown the effect of polymeric binders on

particle dispersion, unveiling their influence on the electrical conductivity of electrode layers [140–142]. Proper binder to particle ratios and dispersion properties of the binder lead to the formation of a conducting network, enhancing the electron transport kinetics and yielding higher energy, power and life time performance.

Battery life time strongly depends on the mechanical integrity of the dry electrode. During lithium intercalation, the electrode must withstand mechanical stresses due to expansion and shrinkage of the electrochemically active material [143–145]. The volume fluctuations can induce a local delamination of the electrode layer from the current collector and cracking within the layer. Hence, considerable research work dealt with the determination of adhesive strength between electrode layer and substrate [91, 123, 124, 129, 146–150, 152, 229, 232–235]. However, the cohesive strength in the electrode layer has not received much attention yet. The scratch test has been used to characterize the mechanical strength or scratch resistance of electrodes [155, 215, 232]. Since in this test the electrode layer experiences tangential and normal forces, the measured load comprises information about the adhesive as well as the cohesive strength of the electrode. Chen et al. combined micro-scratch and digital image correlation techniques to decouple particle/particle cohesion from electrode-layer/current-collector adhesion and defined the coefficient of friction as a measure of cohesive strength [157]. Nevertheless, it remains elusive whether such local force measurements are representative for the cohesive strength of the electrode layer. Finally, indentation and tensile tests have been carried out to determine the mechanical properties of electrode layers [152–154,156]. These studies provided some understanding about how wet processing of the slurry affects porosity and mechanical properties of the dry layer. Still, the true contribution of the binder to the cohesive strength of electrode layers is not yet fully resolved.

In this study we present a holistic view on the role of polymeric binders for LiB anodes, including preparation and processing of wet slurries as well as the microstructure, electrical conductivity and mechanical integrity of dry electrode layers. We first investigate the influence of CMC concentration, molecular weight and degree of substitution on flow behavior of aqueous anode slurries. Rheological data are not only relevant to judge processing behavior, here we use them to characterize the degree of substitution of CMC on active material particles and the degree of dispersion of these particles in the slurry at technically relevant concentrations. The slurries are then cast on to glass plates and copper foils and dried to determine the electrical conductivity and the adhesive strength of the electrode layer, respectively. Furthermore, first cohesive strength data for thick anode layers comprising graphite, carbon black and CMC are presented. The adsorption behavior of CMC on the particle surface is discussed and correlated to the obtained results. Finally, we present data characterizing the cohesive strength of anode layers under well-defined mechanical load conditions for the first time and correlate these data to the electrode microstructure and its change with varying type and concentration of CMC, emphasizing its relevance for the mechanical integrity of the electrode layer beyond the mere presence of the polymeric binder. With respect to the typical composition of commercial LiB electrodes, the influence of two different SBR-binders on

the mechanical, structural and electrical properties mentioned above is also discussed.

6.4 Experimental

6.4.1 Materials

Commercially available flake-like, synthetic graphite particles (SLP50, Imerys Graphite & Carbon, Switzerland) with a volume-based average diameter $x_{50,3}$=23 μm, a specific surface area of 5.7 m^2g^{-1} and density of 2.25 gcm^{-3} are used as active material for the preparation of aqueous anode slurries. Carbon black (CB, C-Nergy Super C65, Imerys Graphite & Carbon, Switzerland) with a primary particle size $x_{50,3}$=32 nm, a specific surface area of 64.1 m^2g^{-1} and density of 1.8 gcm^{-3} was added as a conductivity agent. CB particles tend to agglomerate in the slurry reaching an average agglomerate size of 5 μm. Four types of sodium carboxymethyl cellulose (CMC, Sigma Aldrich, Germany) with average molecular weight (Mw) of 250 kDa and 700 kDa were used in this investigation. The latter had a degree of substitution (DS) of 0.9, whereas three different DS of 0.7, 0.9 and 1.2 were investigated for CMC with Mw=250 kDa. Additionally, CMC with Mw=400 kDa and DS=0.9 was purchased from Dow Wolff Cellulosics GmbH. Commercially available styrene butadiene rubber (SBR, TRD2001, JSR Micro NV., Belgium) as well as a modified version (TRD105A) were used as secondary binder. These polymers are supplied as aqueous dispersions of nanoparticles (particle volume fraction 48 vol% and 41 vol% for TRD2001 and TRD105A, respectively). According to manufacturer, TRD2001 exhibits a particle size of 170 nm and a glass transition temperature of -2°C, whereas TRD105A has a particle size of 95 nm and a glass transition temperature of -5°C. Small amplitude oscillatory shear experiments at fixed frequency and deformation covering a wide temperature range on dry SBR films did not show a cross-over of the storage (G') and loss (G") moduli at high temperatures, indicating high molecular weight of the polymers or even chemical cross-linking (see supporting information). Gravimetric measurements using toluene as solvent yielded a degree of cross-linking of 89.9 % ± 0.5 % and 81.5 % ± 0.4 % for TRD2001 and TRD105A, respectively.

6.4.2 Sample preparation

Anode slurries with a constant solid volume fraction ϕ_p = 20 vol% and a constant graphite to CB volume ratio of 46.5 were studied. The CMC concentration was varied in a range ϕ_{CMC} = 2.5 vol% - 4.0 vol% for different molecular weight and degree of substitution. Here, ϕ_{CMC} refers to the amount of polymer in the dry electrode layer. First, CMC was dissolved in distilled water and homogenized with a 55 mm propeller mixer at 1200 rpm for 30 min. Carbon black, followed by graphite particles, were dispersed in the aqueous CMC solution using a 50 mm dissolver disk at 1600 rpm for 5 min each. Only part of the total amount of water needed for the slurry was initially used to prepare the CMC solution in order to ensure particle deagglomeration and ideal slurry homogeneity. After addition of the solid particles, the remaining amount of water was added stepwise in four intervals of 5 min each until reaching the desired solids content [236]. For anode

slurries including SBR, the secondary polymer was added after dispersion of the solid particles and finally the desired solids content was adjusted by adding the appropriate amount of water. Slurries including both polymer binders were studied at fixed CMC concentration ϕ_{CMC}=2.5 vol% and constant Mw=700 kDa and DS=0.9 but varying SBR concentration in a range ϕ_{SBR}=1.0 vol% - 5.0 vol%.

Slurries were coated on glass plates and 10 μm thick copper foil (SE-Cu, Schlenk Metallfolien GmbH & Co. KG, Germany) for electrical conductivity and adhesive strength measurements, respectively. Therefore, a doctor blade (ZUA 2000, Zehntner GmbH, Switzerland) with a coating width of 60 mm and a coating gap of 300 μm was applied. Subsequently, the wet film was dried at 60°C for 30 min. Additionally, thick electrode layers were prepared for the determination of the cohesive strength in the dry electrode layer. Slurries were poured into a 26x49x11 mm3 (WxLxH) silicone mold and dried at 60°C for 24 h, during the first 3 h of drying an aluminum foil covered one third of the area to suppress the Marangoni effect. The dry layers were then cut and grinded into smaller samples with defined shape. First, the samples were brought into shape using sandpaper with rough texture and then smoothed applying fine sandpaper. Different sample shapes were used to determine the cohesive strength of the electrode layer depending on the applied load type as summarized in Table 6.1.

Table 6.1: Sample geometry for cohesion testing. All samples had a height of 1.5 mm.

Load type	**Sample width [mm]**	**Sample length [mm]**
Compression	5	5
Flexural	20	45
Tensile*	5	24
Torsion	9	35

*Dog bone test samples: width at the middle of the sample, length between device clamps.

6.4.3 Sample characterization

Rheological measurements

The flow behavior of the anode slurries was characterized applying rotational steady shear measurements. A stress controlled rheometer (Physica, MCR 501, Anton Paar GmbH, Germany) was used to determine the viscosity η in the shear stress range 0.1 Pa $< \tau <$ 1000 Pa. All measurements were performed with a 5 min waiting period before starting the measurement to ensure structure recovery using a 25 mm diameter plate-plate geometry and 1 mm gap width at 20°C.

Electrical conductivity tests

The four-point resistivity test was conducted on a self-manufactured set-up equipped with four measuring probes (S4D5G, Uwe Electronic GmbH, Germany). Measurements were carried out at five different positions of the 60mmx120mm anode layer applying five different currents and recording the corresponding voltage. An average value of the electrical conductivity was calculated for a probe spacing of 30 mm according to Smits [218].

Mechanical properties

The adhesive strength of the electrode layer to the copper foil was characterized using a 90°-peel-test based on the standard DIN 28510-1. A universal testing machine (Texture Analyzer TA.XT plus, Stable Micro Systems, UK) was used to peel off the copper foil. Specimen with a width of 25 mm and a length of 60 mm were fixed to the measuring plate with double-sided adhesive tape (Universal, Tesa SE, Germany). A 500 g plate was set on top of the electrode layer as a pre-compression step to ensure homogeneous contact between adhesive tape and electrode layer. All measurements were performed at a constant peel velocity of 5 mms^{-1} using a 5 kg load cell force sensor (max. force: 5 kg, force sensitivity: 0.1 g). The measured tensile force was normalized to the line width. This line load was used as a measure for adhesive strength.

The cohesive strength of the electrode layer was determined employing standard test methods for the characterization of mechanical properties. Compressive $\sigma_{c,max}$ and flexural strength $\sigma_{b,max}$ (4-point bending) measurements were conducted using a universal testing machine (Texture Analyzer TA.XT plus, Stable Micro Systems, UK) based on the standard DIN 51104 and DIN 843-1, respectively. Additionally, tensile strength $\sigma_{t,max}$ tests were carried out using custom-made measuring fixtures and DIN ISO EN 527-4 based sample geometries. Further, the torsional strength $\sigma_{tor,max}$ was obtained from dynamic mechanical analysis using a stress-controlled rheometer (Physica, MCR 301, Anton Paar GmbH, Germany) equipped with a 12 mm solid rectangular fixture (SRF 12). Therefore, oscillatory stress-sweep measurements were carried out at a constant frequency of 0.1 Hz until exceeding the destruction-free linear viscoelastic region, indicating the maximum torsional strength of the sample.

Microstructure

The porosity ϵ of the electrode layers was determined from the Archimedes density according to DIN EN 993-1 and DIN EN 993-18. Samples of dry electrodes were vacuum infused with epoxy resin, grinded with SiC paper and polished with a diamond suspension to investigate the microstructure of the electrode layers by means of scanning electron microscopy (SEM) using a LEO1530 microscope (Carl Zeiss AG, Germany).

6.5 Results and discussion

6.5.1 Rheological characterization

The viscosity η of anode slurries with and without CB as a function of the shear stress τ was compared to that of corresponding pure CMC solutions to characterize their flow behavior and the influence of solid particles on the rheological properties of the slurries. Figure 6.1 shows such flow curves for slurries including CMC with M_w = 700 kDa and DS = 0.9 at ϕ_{CMC} = 4 vol%. The CMC concentration refers to the amount of CMC in the dry electrode layer. The slurries show higher viscosity than the pure CMC solution. The relative viscosity η_{rel}=$\eta_{slurry}/\eta_{solution}$ for the slurry comprising graphite and CB is $\eta_{rel} \approx$ 2-3 throughout the investigated shear stress range as expected for well dispersed non-Brownian hard sphere suspensions with ϕ_p = 20 vol% [6]. For the slurry containing only graphite, the low shear viscosity is substantially higher ($\eta_{rel} \approx 10$), indicating incomplete dispersion of particles, i.e. agglomerates immobilizing part of the solvent still exist. At high shear stresses these agglomerates are broken up due to sufficient energy input and the viscosity of both slurries matches.

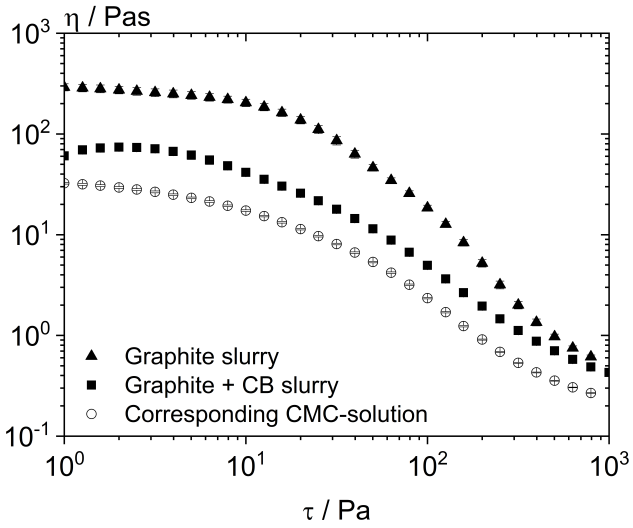

Figure 6.1: Viscosity as a function of shear stress for anode slurries with and without CB as well as the corresponding CMC solution. The particle loading of the slurries is ϕ_p=20 vol%. The aqueous CMC solution includes 4 vol% CMC with M_w=700 kDa and DS=0.9.

The influence of DS and Mw of CMC on the low shear (τ=1 Pa) and high shear (τ=500 Pa) viscosity of anode slurries was investigated at different CMC concentrations. The low shear viscosity provides information about the particle dispersion in the slurry, whereas the high shear viscosity at constant ϕ_p reflects the amount of CMC dissolved in the fluid phase. The low shear viscosity as well as the high shear viscosity values of anode slurries slightly increase with increasing DS at constant M_w, suggesting that a lower DS results in slightly better particle dispersion and lower amount of free

CMC in the fluid phase (see supporting information) as expected due to the higher degree of CMC adsorption on particle surfaces at low DS [231].

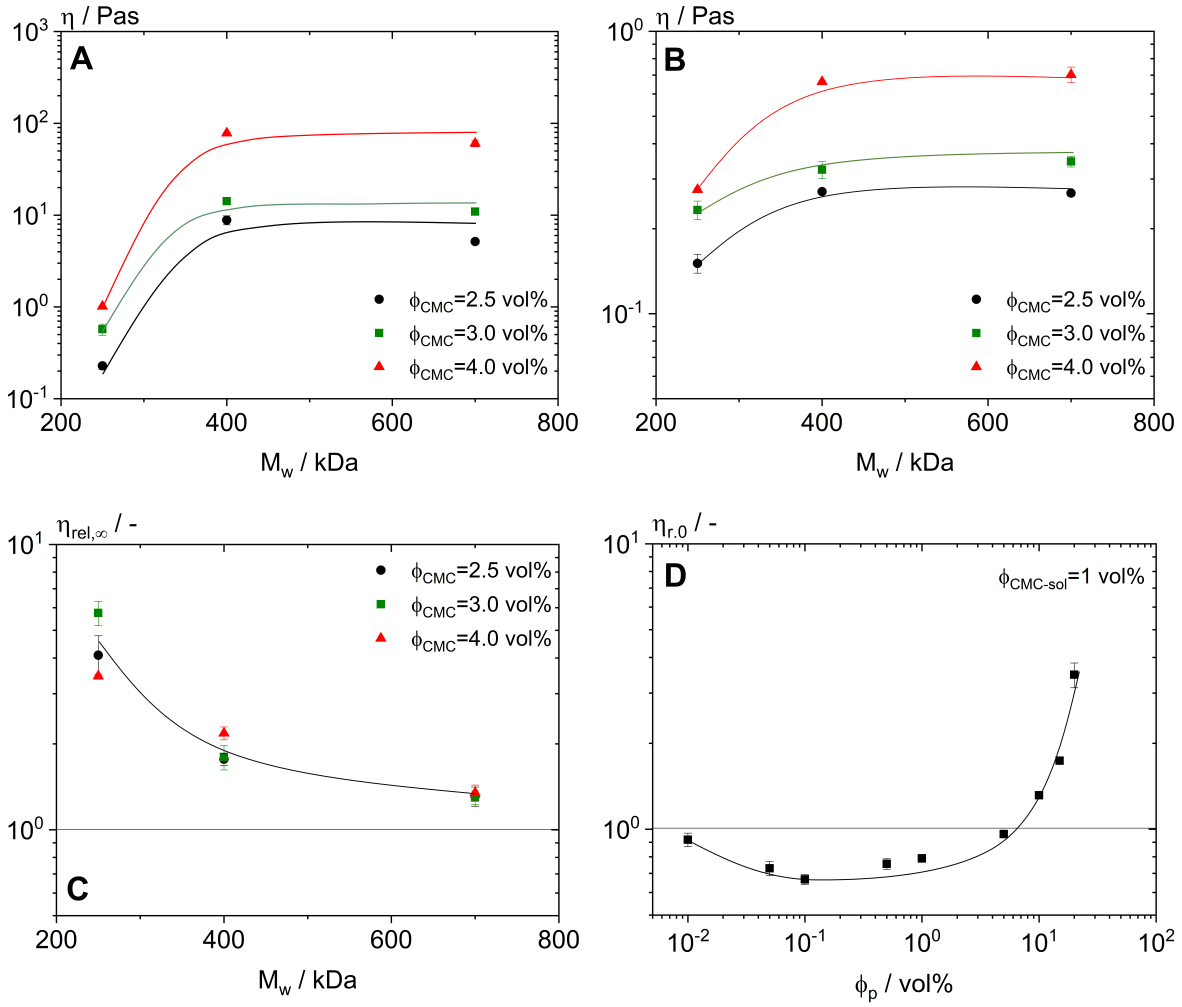

Figure 6.2: Viscosity of anode slurries at (A) low (τ=1 Pa) and (B) high (τ=500 Pa) shear stresses vs. molecular weight of added CMC (DS=0.9). (C) shows the relative high shear viscosity $\eta_{rel,\infty}$ calculated from the data shown in (B) and the corresponding viscosity data for the respective CMC solutions. Slurries with different amount of CMC but at constant ϕ_p=20 vol% were investigated. (D) Relative zero shear viscosity $\eta_{r,0}$ of graphite suspensions as function of particle loading ϕ_p. Graphite particles were suspended in an aqueous 1 vol% CMC solution with M_w=700 kDa and DS=0.9.

The low and high shear viscosity of slurries at different ϕ_{CMC} and constant DS = 0.9 is displayed as a function of M_w in Figure 6.2A and B, respectively. Instead of a monotonic increase of viscosity with M_w according to a superior thickening efficiency of longer polymer chains we find, that both low and high shear viscosity increases with

increasing M_w up to 400 kDa and then levels off for all investigated ϕ_{CMC} [237]. This result can be related to the adsorption behavior of CMC on graphite and CB particles. To gain better insight into the M_w dependence of CMC adsorption on the suspended particles, the relative viscosity at high shear stress (τ=500 Pa) $\eta_{rel,\infty}=\eta_{\infty,suspension}/\eta_{\infty,solvent}$ was plotted against M_w as shown in Figure 6.2C. The characterization of the CMC adsorption behavior using this rheological approach renders a significant advantage over common techniques like optical methods or adsorption isotherms, which require highly dilute systems. In contrast, rheological measurements enable the determination of CMC adsorption on the solid particles surface at technically relevant particle loadings. The relative high shear viscosity $\eta_{rel,\infty}$ monotonically decreases with increasing M_w, indicating a reduced fraction of free polymer in the solvent when using high M_w CMC. Consequently, the high shear viscosity of the slurry does not increase monotonically with M_w. Obviously, the effect of reduced free polymer in solution outweighs the slight increase in effective ϕ_p due to the CMC adsorption layer and the effect is independent of ϕ_{CMC} in the concentration range investigated here. It must be noted that the addition of SBR does not affect the flow behavior of the slurry. The contribution of the SBR nanoparticles to the overall particle volume fraction is negligible in relation to the active material.

To shed more light on the adsorption behavior of CMC on graphite particles a series of graphite suspensions with ϕ_p ranging from 10^{-2} to 20 vol% was investigated with respect to their zero-shear viscosity $\eta_{0,suspension}$ normalized to the zero-shear viscosity $\eta_{0,solvent}$ of the used solvent, an aqueous 1 vol% CMC (M_w = 700 kDa, DS = 0.9) solution. The selected CMC concentration allows for a conclusive investigation of the adsorption behavior since higher concentrations result in a weaker change in relative viscosity, since a high amount of CMC is dissolved in the continuous phase, whereas lower concentrations would aggravate assessment of reliable relative viscosity data. The zero-shear viscosity of the CMC-solution as well as the graphite suspensions was obtained as the limiting constant viscosity value obtained at vanishing shear stresses. The relative viscosity $\eta_{r,0}=\eta_{0,suspension}/\eta_{0,solvent}$ of these graphite suspensions as a function of particle concentration is shown in Figure 6.2D. This quantity exhibits a clear minimum around ϕ_p = 0.2 vol%, i.e. at a CMC to graphite volume ratio of 5 with a minimum value $\eta_{r,0} \approx 0.6$. In very dilute suspensions ($\phi_p \approx 10^{-2}$ vol%), however, $\eta_{r,0}$ approaches one, as expected. Interestingly, $\eta_{r,0}$ values are below 1 for $\phi_p < 5$ vol%. As confirmed by numerous theoretical and experimental studies the relative viscosity η_r of suspensions increases with increasing particle loading and $\eta_r > 1$ always holds [194–196, 238]. Therefore, another physical mechanism must control the low shear viscosity of the dilute graphite slurries investigated here. Li et al. showed a decrease of zeta potential for low concentrated graphite and CB suspensions upon addition of CMC, suggesting polymer adsorption on the particle surface [61]. Accordingly, the addition of graphite particles to the CMC solution decreases the polymer concentration in the fluid phase. The corresponding drop in $\eta_{0,suspension}$ is more pronounced than the weak increase in viscosity expected due to the added graphite, leading to relative viscosities below 1. At higher graphite concentration ($\phi_p > 5$ vol%), however, $\eta_{r,0}$ strongly increases because of the strong contribution of the particles to the suspensions viscosity. For ϕ_p = 20 vol%, $\eta_{r,0}$ is even somewhat higher

than 3, the value expected for non-Brownian hard sphere suspensions [6], and this is attributed to an increase in effective particle volume fraction due to the adsorbed CMC layer. In this concentration range the increase in $\eta_{0,\text{suspension}}$ with increasing particle concentration dominates over the drop in solvent viscosity due to the increasing fraction of CMC adsorbed to the particles when ϕ_p increases.

6.5.2 Electrical conductivity

Anode slurries were coated on glass plates and dried to investigate their electrical conductivity. Figure 6.3A shows corresponding data for layers including different CMC concentration and constant DS=0.9 as a function of M_w. Note, the conductivity is due to the formation of a conducive CB particle network [140, 141]. Anode layers including only graphite exhibit overall lower values and an analog dependence on CMC concentration, M_w and DS as the electrical conductivity of anodes comprising graphite and CB. Irrespective of CMC molecular weight, conductivity of the dry anode layers clearly decreases with increasing polymer concentration as expected since the polymer can deteriorate and interrupt conductive pathways. However, the polymer molecular weight obviously has a significant impact on conductivity too. At given ϕ_CMC, the absolute values obtained for the layers including the CMC with $M_w = 700$ kDa are about 50% higher than that for the layers prepared using CMC with $M_w = 250$ kDa. It is well known from literature and it is also obvious from our rheological investigations discussed above that the mass of polymer adsorbed to the particle surface increases with increasing molecular weight [239–241]. Consequently, the fraction of CMC randomly distributed in the dried samples decreases with increasing M_w and it seems this fraction deteriorates the electrical conductivity of the anode layers investigated here. This new insight into the adsorption behavior of CMC with different polymer chain-length and its relationship to particle dispersion and electrical conductivity offers a path to increase conductivity through targeted choice of CMC molecular architecture at constant ϕ_CMC. Hence, power and energy density of corresponding cells might be improved. Finally, it should be noted that the degree of substitution has no significant effect on dry anode layer conductivity irrespective of concentration or molecular weight of the added CMC (data not shown). This is in good agreement with rheological data indicating a weak effect of DS on low and high shear viscosity of the wet anode slurry.

Considering the high conductivity values of anodes including CMC at low concentration and high molecular weight, the influence of SBR type and concentration on the electrical conductivity of anode layers was investigated at constant ϕ_CMC=2.5 vol%, M_w=700 kDa and DS=0.9 (Figure 6.3B). Increasing ϕ_SBR leads to a monotonic decrease of electrical conductivity. Rheological data of corresponding wet slurries showed no significant effect of SBR on the flow behavior, i.e. variation of ϕ_SBR hardly affects particle dispersion and polymer adsorption. Hence, the decay in electrical conductivity is assumed to be a consequence of randomly distributed isolating polymer particles, blocking conductive pathways. Interestingly, anodes including TRD105A yield overall higher values than those of anodes based on TRD2001. This might be due to the smaller particle

size or due to proprietary differences in polymer architecture or specific electrical properties. Elucidating this is, however, beyond the scope of this work focusing on the role of CMC as binder for LiB electrodes.

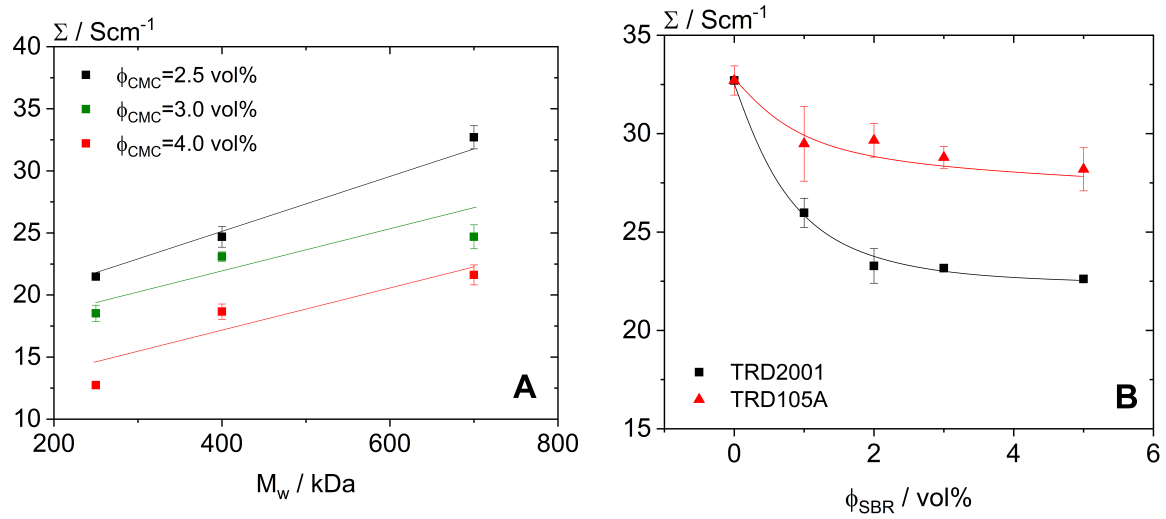

Figure 6.3: Electrical conductivity of dry electrode layers as a function of Mw including CMC at different concentrations and constant DS=0.9 (A) as well as of ϕ_{SBR} including CMC with constant ϕ_{CMC}=2.5 vol%, M_w=700 kDa and DS=0.9 but varying SBR-type.

6.5.3 Mechanical properties and electrode microstructure

Adhesion

The influence of CMC on the adhesive strength between electrode layer and copper foil was investigated using the 90°-peel test. In all cases complete detachment of the anode layer from the current collector was observed (see supporting information). Figure 6.4A shows the line load of the measured samples over DS at constant M_w=250 kDa, whereas Figure 6.4B displays line load data as function of M_w at constant DS=0.9, in both cases ϕ_{CMC} was varied between 2.5 vol% and 4 vol%. Considering the experimental uncertainty of the measurements there is no significant dependence of adhesive strength on M_w or DS. In all investigated cases, the adhesive strength between electrode layer and current collector lies between 0.6 and 1.8 Nm^{-1}, and it must be noticed that the obtained values are more than one order of magnitude lower than that for water-based anodes containing an additional latex or rubber as binder system in combination with CMC [91, 148, 242]. This clearly shows that CMC hardly contributes to adhesion and that the addition of a second polymer is essential for the bond strength between electrode layer and current collector. Peel tests performed for SBR films on copper foils showed an average line load of 948 ± 47 Nm^{-1} and 832 ± 53 Nm^{-1} for TRD2001 and TRD105A, respectively, whereas CMC films, irrespective of M_w and DS, yielded only an average of

2.3 ± 0.7 Nm^{-1}. Accordingly, the intrinsic contribution of SBR to the adhesion of a LiB electrode is dramatically higher than that of CMC. The addition of SBR significantly enhances the adhesion between anode layer and current collector, increasing linearly with incrementing ϕ_{SBR} (see supporting information). SBR concentrations above 3.0 vol% yield adhesive strength values typical for aqueous anode layers reported in the literature [91, 242] (Figure 6.4B).

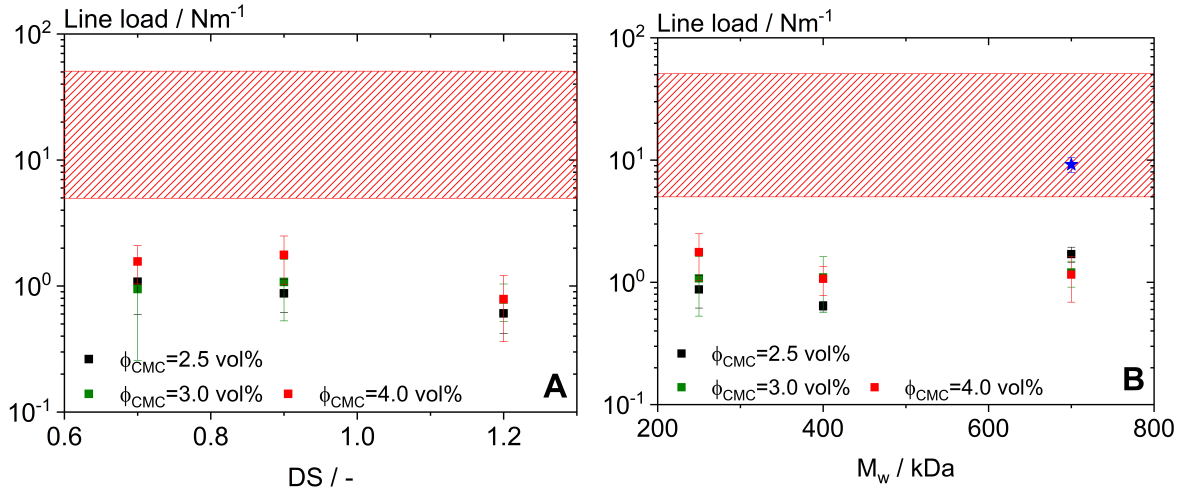

Figure 6.4: Adhesive strength of electrode layers including different CMC concentration as a function of (A) DS at constant M_w=250 kDa and (B) M_w at constant DS=0.9. Red hatched area denotes the line load of water-borne anode layers including graphite as active material and CMC as well as SBR as binder system [91,242]. The blue star in the red hatched area indicates the adhesive strength of anode layers including CMC with constant ϕ_{CMC}=2.5 vol%, M_w=700 kDa, DS=0.9 and TRD2001 at ϕ_{SBR}=3.0 vol%.

Cohesion

In this section the cohesive strength of thick electrode layers is discussed focusing on the effect of added CMC. Different well-defined mechanical load types were employed to determine the critical stress at which the structure collapses. Results for layers including different concentrations of CMC with M_w=250 kDa and DS=0.9 are summarized in Figure 6.5. Irrespective of load type the respective maximum stress increases almost linearly with increasing ϕ_{CMC}. The absolute value of σ_{max} depends on the nature of the load, i.e. it depends on whether the material is being pushed together, pulled apart, bent or twisted. The relative change in failure stress, however, is almost independent of load type. All test methods yield reliable and reproducible results and are therefore, suitable to characterize the cohesive strength of thick electrode layers. For the first time, cohesive and adhesive strength of electrode layers is determined independently. This should help to understand the delamination and cracking behavior due to cyclic

lithium intercalation. For sake of convenience we will discuss the compressive strength in the subsequent part of this section. The other methods yielded similar trends upon variation of sample composition (see supporting information).

The porosity of thick electrode layers, used to investigate the cohesive strength, was measured and compared to that of thin layers used for electrical conductivity and adhesion measurements. The overall porosity of all samples was between 55% and 58%, showing no particular influence of CMC concentration, M_w, or DS. Similar results were reported in the literature for other water-borne LiB anodes. Thus, a significant influence of the sample porosity on the measured cohesive strength of thick electrode layers can be disregarded. Additionally, SEM images of thin and thick electrode layers exhibit no recognizable difference in their microstructure (see supporting information). Accordingly, the measured cohesive strength of thick electrode layers, investigated in this work, is assumed to be representative for conventional electrode layers.

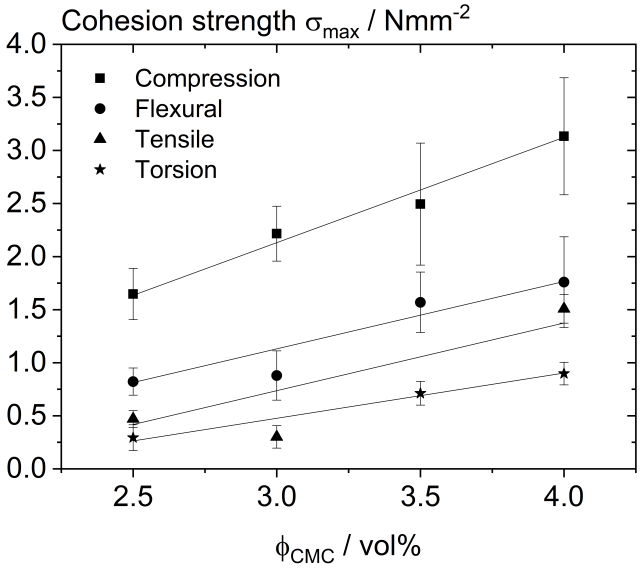

Figure 6.5: Maximum stress at break of thick electrode layers as a function of ϕ_{CMC} measured employing different load types. Samples including CMC with constant M_w=250 kDa and DS=0.9 were investigated.

Figure 6.6A displays the compressive strength of thick electrode layers including CMC with M_w=250 kDa as a function of DS and Figure 6.6B shows the compressive strength as a function of M_w at constant DS = 0.9. In both cases data were obtained at various ϕ_{CMC} between 2.5 vol% and 4 vol%. First, it should be noted that the cohesive strength of pure CMC films neither depends on M_w nor on DS as directly confirmed by tensile test results obtained for the CMC grades investigated here (see supporting information).

The cohesive strength of electrode layers, however, strongly depends on these molecular parameters. On one hand, it significantly decreases with increasing DS. This decay

is more pronounced at higher ϕ_{CMC}, and for DS = 1.2 the compressive strength hardly varies with ϕ_{CMC}. Adsorption isotherms for CMC on graphite particles show higher adsorption values for CMC with lower DS [231] corresponding to a lower solubility in water. Our results clearly show that this also has an effect on mechanical strength of the electrode layer and we assume that this is due to different particle dispersion and dry electrode layer microstructure depending on DS.

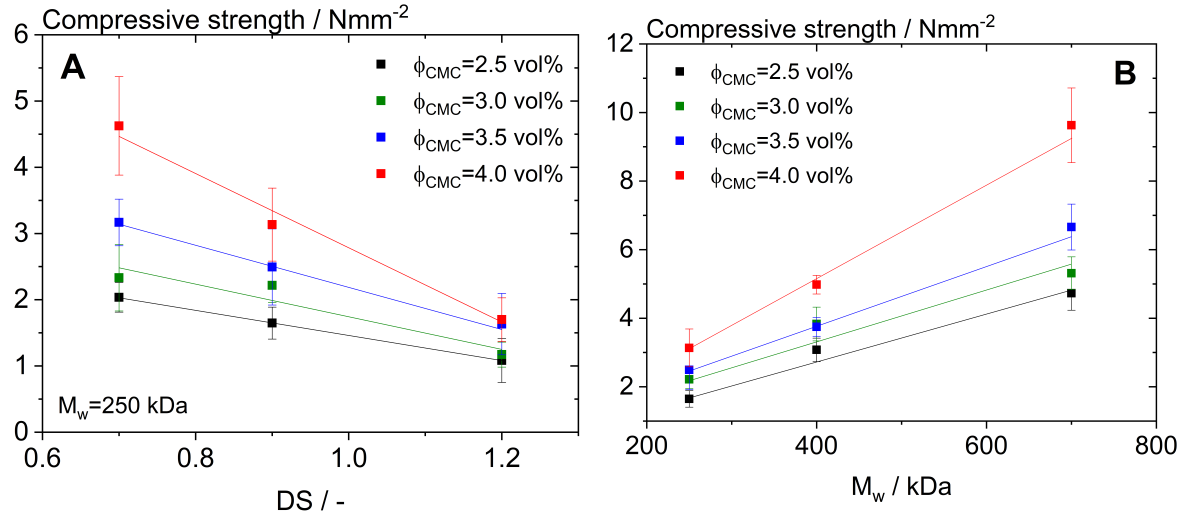

Figure 6.6: Maximum compressive strength of thick electrode layers including different CMC concentrations as a function of (A) DS at constant M_w=250 kDa and (B) M_w at constant DS=0.9.

On the other hand, the cohesive strength of the thick dry layers increases with increasing M_w, particularly at high ϕ_{CMC}. The high cohesive strength obtained at high M_w again seems to be related to the higher fraction of CMC adsorbed on the surface of the graphite particles (Figure 6.2C). We hypothesize that the CMC molecular weight and the related variation in adsorption to the graphite and CB particles has a strong impact on particle dispersion as already indicated by its impact on slurry viscosity and in turn on microstructure and mechanical strength of the dry layer. This will be discussed in the next section. These findings indicate that electrode cohesion can be significantly increased without increasing CMC concentration but through proper choice of molecular structure.

Finally, it should be noted that SBR does not contribute to the cohesive strength of thick anode layers irrespective of amount or type of added SBR (see supporting information). This is partly due to its lower intrinsic strength. Tensile tests performed on pure SBR films based on the standard DIN ISO EN 527-4 yielded intrinsic mechanical strength values of 4.3 ± 0.7 Nmm^{-2} and 9.2 ± 1.4 Nmm^{-2} for TRD2001 and TRD105A, respectively, whereas for CMC values > 15 Nmm^{-2} were obtained, irrespective of M_w and DS. In addition, previous work [199] indicated that the addition of nanoparticulate

secondary polymers hardly affects the electrode microstructure, which in turn controls the cohesive strength.

Microstructure

As already mentioned above, the porosity of all investigated samples was in the range between 55% and 58% irrespective of CMC concentration, M_w or DS. In more detail, SEM images of thick electrode layers were taken to investigate their microstructure. As shown by compression tests, a significant influence of M_w on the cohesive strength is obtained for ϕ_{CMC}=4.0 vol% and DS=0.9. Hence, SEM images of thick layers including 4 vol% CMC with M_w=250 kDa and M_w=700 kDa (DS=0.9 in both cases) were compared (Figure 6.7A and B). Electrodes including the low molecular-weight CMC show a random orientation of the flake-shaped graphite particles, whereas corresponding electrodes containing high molecular-weight CMC exhibit a clear particle alignment. Image processing was carried out for both images to quantify this observation. Individual particles and particle collectives were detected and their angle of orientation in relation to a centered coordinate system was noted, as marked in red (Figure 6.7A and B). The particle frequency as a function of the orientation angle for samples including CMC with M_w=250 kDa, M_w=400 kDa and M_w=700 kDa at constant DS=0.9 is shown in Figure 6.7C, D and E, respectively. For the M_w=250 kDa sample, image analysis yields a broad distribution of particle orientation i.e. a random isotropic layer structure. In contrast, high molecular-weight CMC (M_w=700 kDa)leads to particle alignment as confirmed by a narrow distribution of particle orientation. This kind of organized microstructure apparently correlates to the high cohesion values obtained for thick electrode layers based on M_w=700 kDa CMC. Anodes including CMC with M_w=400 kDa show an intermediate degree of particle orientation relative to those of anodes based on low and high M_w. This systematic change in particle alignment correlates to the linear increase of cohesive strength with increasing polymer chain-length, i.e. particle orientation.

Furthermore, SEM images of thick electrode layers including CMC at ϕ_{CMC} = 4 vol%, and constant M_w=250 kDa but varying DS (DS=0.7, DS=0.9, and DS=1.2) were compared to investigate the influence of DS on the microstructure of these layers. The corresponding histograms are shown in Figure 6.7C, F and G. Electrode layers based on low DS result in a narrow distribution of the particle orientation angles, indicating clear particle alignment. Intermediate DS leads to a weak particle alignment towards 100°, whereas higher DS results in randomly oriented particles, i.e. a broad uniform distribution of oriented angles. Analog with the results obtained for electrode layers comprising CMC with different M_w, the particle orientation in the electrode layer correlates to the cohesive strength when using different DS. These results demonstrate that the cohesive strength of electrode layers is determined by the microstructure formed due to the added CMC. This structure and hence the mechanical strength of the layers strongly depends on M_w and DS of the added CMC, although the intrinsic mechanical strength of CMC itself does not depend on these parameters. The high degree of particle alignment at high M_w and low DS is presumably promoted by the lower viscosity of the continuous phase of the corresponding slurry as a result of the higher fraction of CMC adsorbed on the particles.

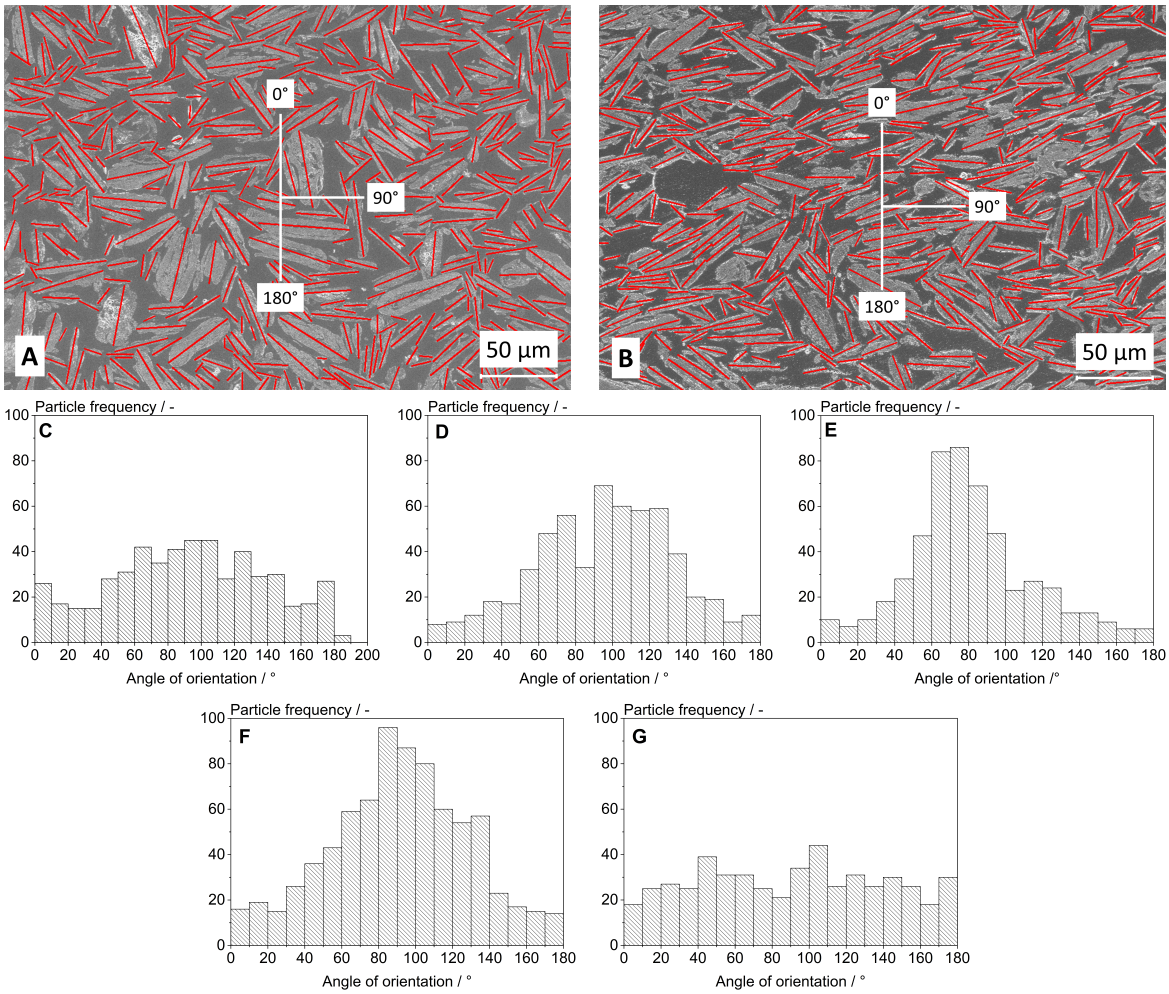

Figure 6.7: Microstructure of thick electrode layers. (A) SEM image of layer including ϕ_{CMC}=4 vol% CMC with DS=0.9 and M_w=250 kDa and (B) M_w=700 kDa. Histograms of particle frequency as a function of angle of orientation relative to the coordinate system indicated y the white line in (A) and (B) in the thick electrode layers including CMC with (C) M_w=250 kDa, (D) M_w=400 kDa and (E) M_w=700 kDa at constant DS=0.9 as well as (F) DS=0.7 and (G) DS=1.2 at constant M_w=250 kDa.

6.6 Conclusions

Here we investigated the effect of CMC, which is widely used as a binder and rheology control agent in waterborne LiB electrode slurries, on the flow behavior of anode slurries as well as on the electrical and mechanical properties and finally also the microstructure of the corresponding dry layers. CMC concentration, M_w and DS were systematically varied in a wide technically relevant range. In addition, the influence of SBR type and concentration on the features mentioned above was discussed. This holistic apporach establishes new insights into the polymer adsorption behavior on active particles at in-

dustrially relevant slurry concentrations as well as clear correlations between particle dispersion, layer microstructure as well as electrical conductivity and mechanical integrity of the electrode.

Shear rheometry revealed that both, low and high shear viscosity strongly increase with M_w up to 400 kDa and then level off irrespective of the amount of added CMC but, as expected, the absolute viscosity values monotonically increase with ϕ_{CMC}. Moreover, the relative high shear viscosity $\eta_{r,\infty}$ is essentially independent of ϕ_{CMC} but monotonically decreases with increasing M_w. We attribute this effect to the partial adsorption of CMC on the solid particles and the corresponding loss of polymer in the solvent. Obviously, the loss of dissolved polymer is more pronounced for higher M_w, as expected [239–241]. This phenomenon was further supported considering the relative viscosity of graphite suspension in a CMC solution covering a broad range of particle loading. The higher affinity of CMC to the graphite surface at lower DS also shows up in the rheological data. Finally, the addition of SBR does not affect the flow behavior of anode slurries.

The electrical conductivity decreased with increasing ϕ_{CMC} as expected, but strikingly conductivity substantially increased with increasing M_w at fixed ϕ_{CMC}. Since the fraction of adsorbed CMC increases with increasing M_w we hypothesize that the remaining free polymer deteriorates the formation of a percolating CB network and hence the conductivity of the dry anode layers. Accordingly, adding CMC with high M_w at constant ϕ_{CMC} results in an increase of electrical conductivity, which is associated to cell power and energy density. The weak changes of CMC adsorption with varying DS did not show up in dry layer conductivity. As expected, increasing SBR concentration also resulted in a monotonic decay of electrical conductivity.

The adhesive strength of dry layers including CMC as only binder component to copper foils is about two orders of magnitude lower than that of conventional, water-based anode layers including a secondary binder and hardly varies with ϕ_{CMC}, M_w or DS. Obviously, CMC does not contribute to the adhesive strength of LiB anode layers. Addition of SBR leads to a linear increase of adhesion at the interface, highlighting the role of rubber-like polymer binders.

The cohesive strength of dry electrode layers has to balance the mechanical stress during cyclic intercalation of Li-ions in the layers, and is supposed to be related to cracking and mechanical failure of battery electrodes. We investigated this phenomenon employing different load types to characterize the critical stress σ_{max} at which thick electrode layers break. As expected σ_{max} significantly increases with ϕ_{CMC} and all employed test methods yielded reliable results. Preliminary porosity measurements and SEM-images confirmed, that the microstructure of the thick layers was similar to that of the thin layers investigated regarding electrical conductivity and adhesive strength. Therefore, we consider the results of these cohesion tests relevant also for thin LiB electrode layers, rendering firs cohesion values for water-based anodes determined under well-defined

mechanical load conditions independent of electrode adhesive strength.

Although the mechanical strength of pure CMC films neither depends on M_w nor on DS, we found a strong dependence of compressive strength of electrode layers on both parameters: σ_{max} decreases with increasing DS but strongly increases with increasing M_w, i.e. with increasing fraction of adsorbed CMC. Apparently, the degree of CMC adsorption on graphite particles also must have a strong impact on the microstructure determining the mechanical strength of the dry layers. This change in microstructure was directly visualized using scanning electron microscopy. Image analysis of these micrographs revealed a strong orientation of graphite particles for layers including CMC with high M_w or low DS, i.e. when a larger fraction of CMC is adsorbed on the particle surface. This effect of CMC adsorption also seems to be decisive for the electrical conductivity of these layers. Contrary to its effect on adhesive strength, the addition of SBR has no influence on the cohesive strength.

In summary, the variation of CMC architecture (M_w, DS) and the corresponding change in adsorption on graphite particles not only affects the flow behavior and hence processing properties of the anode slurries but also the microstructure of the dry layers and hence their electrical conductivity as well as cohesive strength. The holistic study presented in this work renders a comprehensive and systematic understanding of the role of CMC in water-based anodes for LiB, unveiling clear correlations between polymer/particle interactions and resulting electrode properties. Accordingly, the targeted choice of CMC is supposed to be decisive not only for fabrication but also for electrical performance and long-term mechanical stability of LiB electrodes.

6.7 Acknowledgments

R. Gordon gratefully acknowledge financial support by the *100 prozent erneuerbar Stiftung*. Special thanks go to H. Balmer, H. Mild, A. Laghmani and A. García for their experimental assistance and data analysis.

6.8 Supporting Information

Materials

Small oscillatory shear measurements at fixed deformation and frequency covering a wide temperature range were performed for pure SBR films. (s. Figure 6.8). The storage (G') and loss (G") modulus do not exhibit a cross-over at higher temperatures, suggesting long polymer chains or chemical cross-linking.

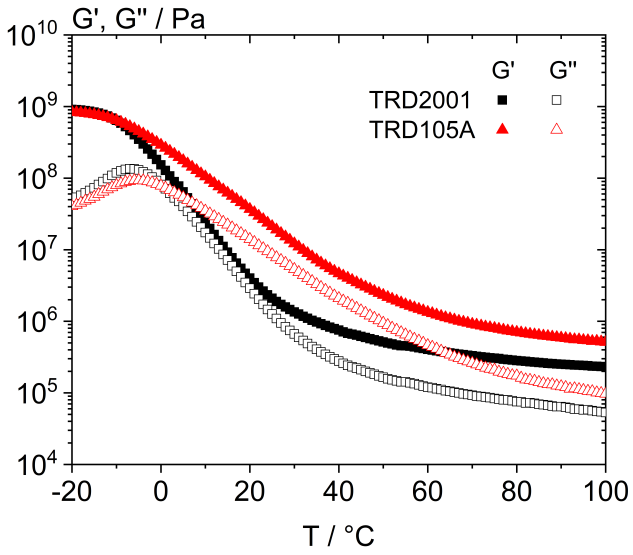

Figure 6.8: Storage (G') and loss (G") modulus of two SBR-types (TRD2001 and TRD105A) as a function of temperature. Measurements were carried out at constant deformation γ=0.01 % and frequency f=0.1 Hz using films of 1.0 mm height.

Rheological characterization

The viscosity η of anode slurries including different CMC concentration ϕ_{CMC} was investigated as a function of the degree of substitution DS but constant molecular weight M_w. Since the low shear viscosity provides information regarding the particle dispersion in the slurry and the high shear viscosity reflects the amount of CMC dissolved in the fluid phase, the influence of DS on the low shear (τ=1 Pa) and high shear (τ=500 Pa) viscosity was studied. Figure 6.9A shows a slight increase of the low shear viscosity with increasing DS, suggesting better particle distribution at low DS. Analog, the high shear viscosity slightly increases with increasing DS (s. Figure 6.9B), indicating lower amount of free CMC in the fluid phase when adding low DS CMC. This result is highlighted when plotting the relative high shear ($\eta_{rel,\infty}$) viscosity against DS (s. Figure 6.9C). The decrease of $\eta_{rel,\infty}$ with increasing CMC concentration indicates that a smaller fraction of CMC adsorbs on the particle surface as ϕ_{CMC} increases, the degree of substitution, however, does not affect the fraction of adsorbed CMC significantly.

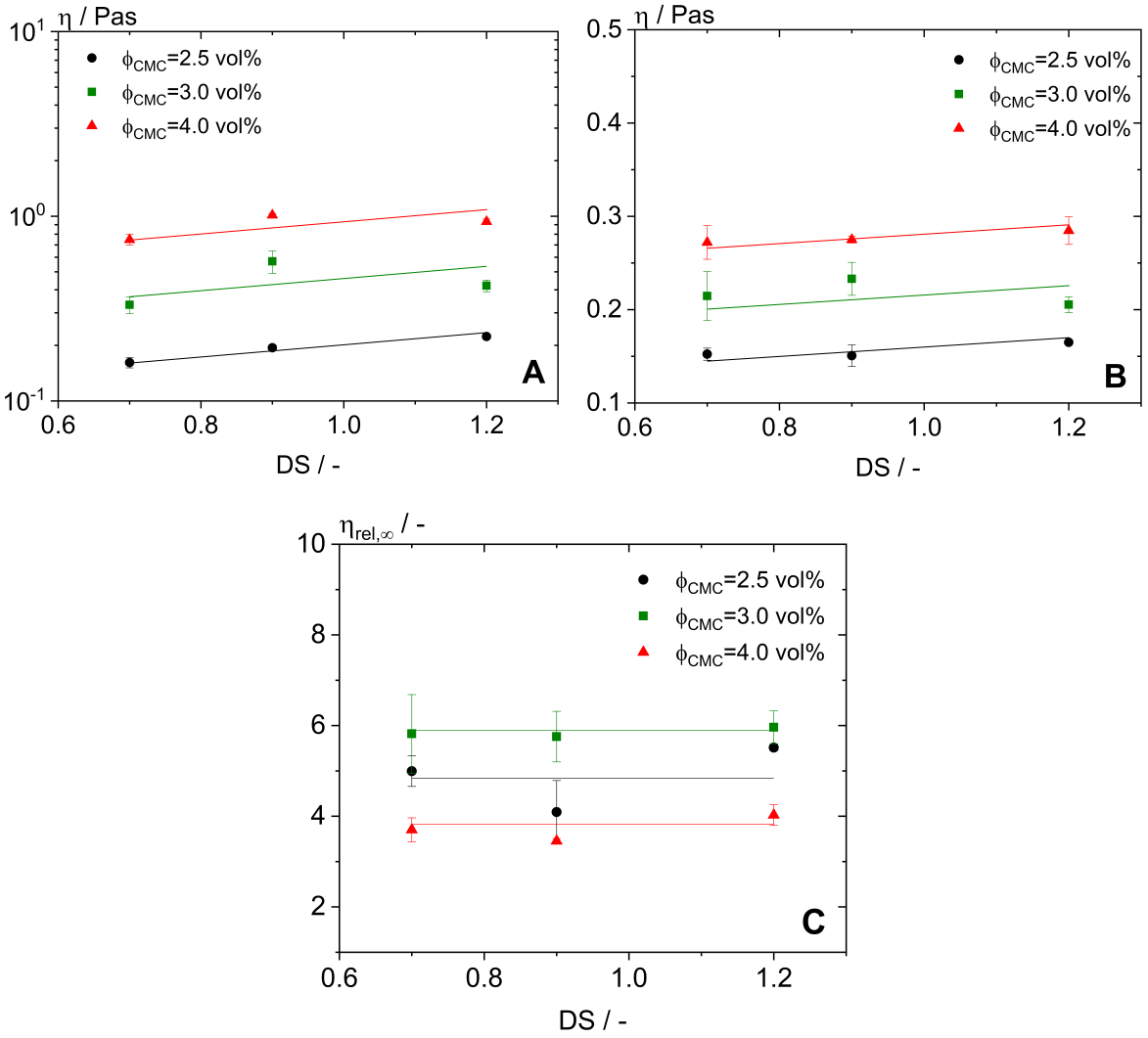

Figure 6.9: Viscosity of anode slurries at (A) low (τ=1 Pa) and (B) high (τ=500 Pa) shear stress as a function of degree of substitution of added CMC (M_w=250 kDa). (C) shows the relative high shear viscosity $\eta_{rel,\infty}$ calculated from the data shown in (B) and the corresponding viscosity of the respective CMC solution. Slurries with different amount of CMC but constant solid volume fraction ϕ_p=20 vol% were investigated. The CMC concentration refers to the amount of CMC in the dry layer.

Adhesion

Figure 6.10A displays an image of an anode layer prepared for the 90°-peel test examination. After the measurement the reliability of the experiment was supported with optical images, depicting complete detachment of the anode layer from the copper foil onto the double-sided adhesive tape (s. Figure 6.10B and C).

Peel-tests of anode layers at constant CMC concentration, molecular weight and DS but varying SBR concentration and type are shown in Figure 6.11. The adhesive strength increases linearly with increasing SBR concentration and anodes including TRD2001 yield overall slightly higher values than those of anodes based on the modified polymer.

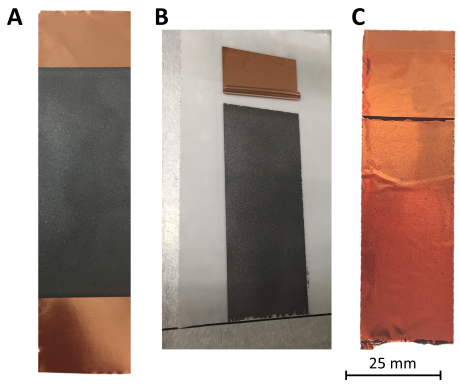

Figure 6.10: Optical images of an anode sample for adhesive strength testing before the measurement (A) and peeled-off anode layer on double-sided adhesive tape (B) as well as corresponding copper foil (C) after examination.

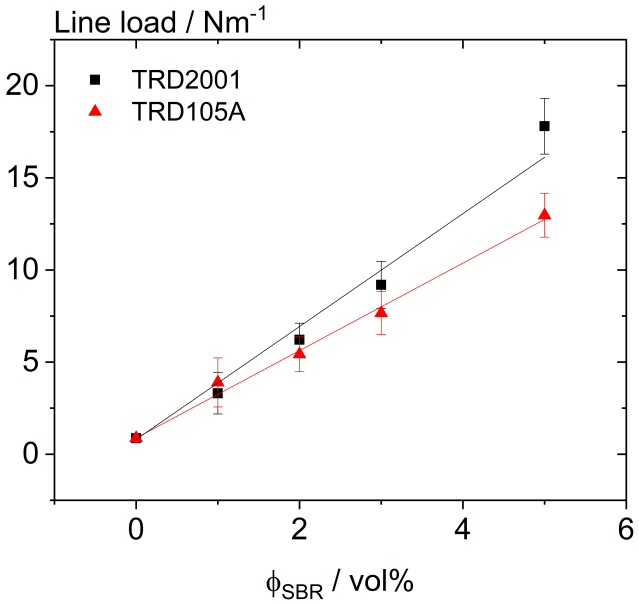

Figure 6.11: Line load as a function of SBR concentration for anode layers including TRD2001 and TRD105A as well as CMC at constant ϕ_{CMC}=2.5 vol%, M_w=700 kDa and DS=0.9.

Cohesion and microstructure

The cohesive strength of thick electrode layers was studied as a function of DS and M_w of added CMC using different load types (see Figure 6.12). The maximum failure stress at which the structure collapses was defined as the cohesive strength of the electrode layer.

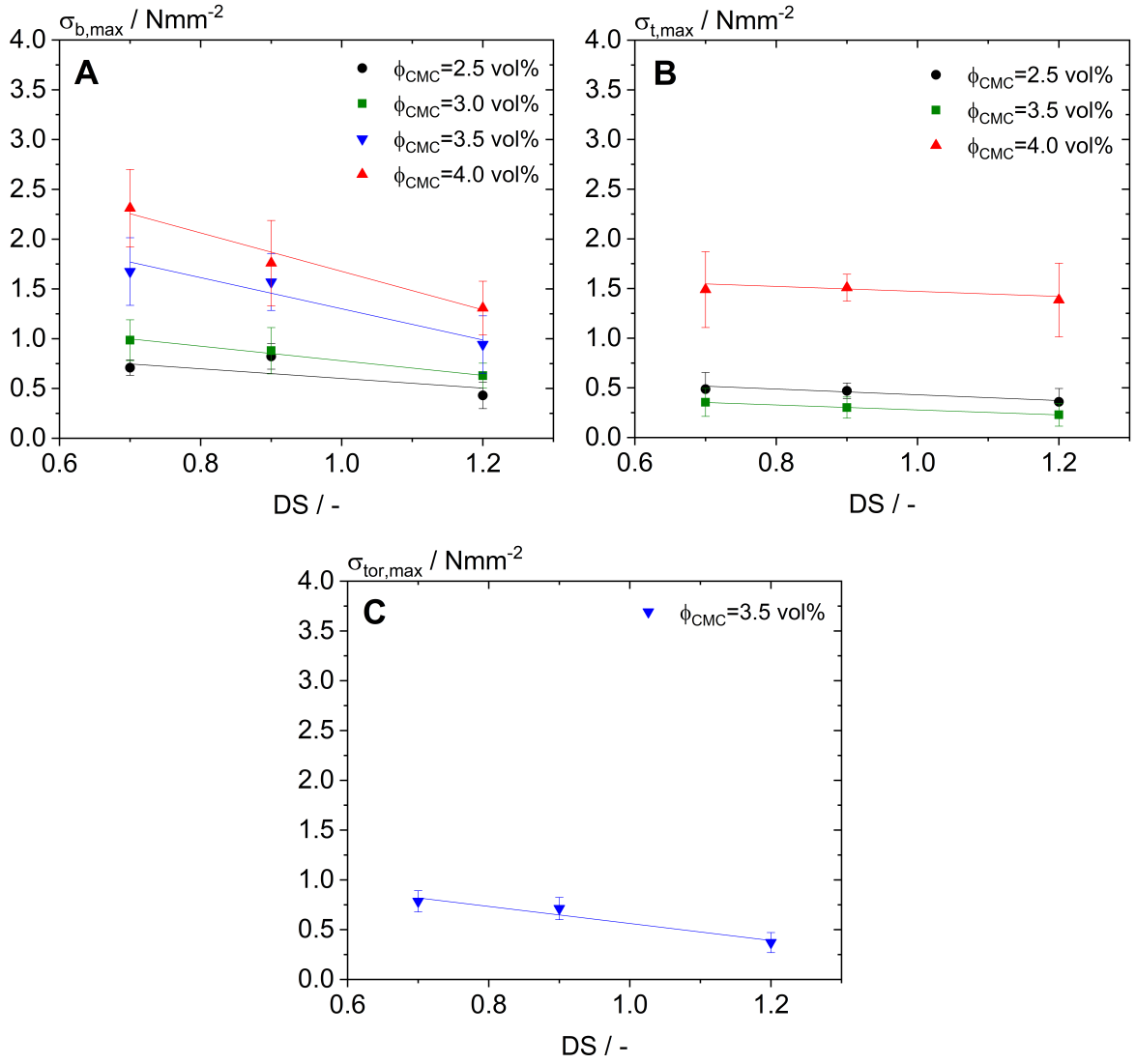

Figure 6.12: Maximum failure stress of thick electrode layers as function of DS but constant M_w=250 kDa using (A) flexural, (B) tensile and (C) torsional tests. Samples including different CMC concentrations were investigated employing flexural and tensile tests, whereas samples at ϕ_{CMC}=3.5 vol% were characterized using torsional tests.

Figure 6.12A, B and C show the maximum flexural, tensile and torsional strength

of thick electrode layers as a function of DS at constant M_w=250 kDa, respectively. Except for samples characterized using torsional tests, layers including different CMC concentration were studied. The cohesive strength decreases with increasing DS. In contrast, the cohesion values increase with increasing M_w but constant DS as shown in Figure 6.13.

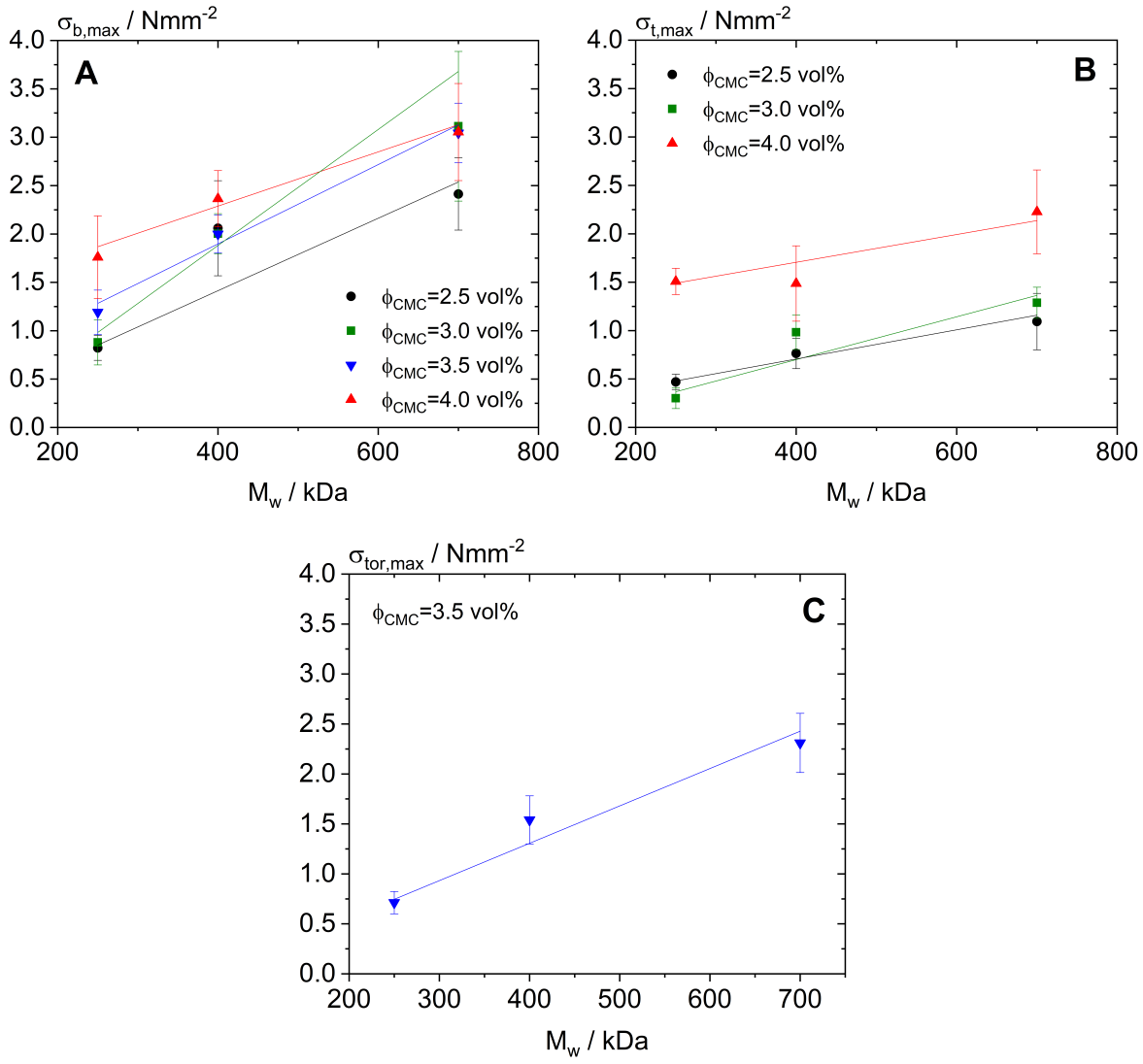

Figure 6.13: Maximum failure stress of thick electrode layers as function of Mw but constant DS=0.9 using (A) flexural, (B) tensile and (C) torsional tests. Samples including different CMC concentrations were investigated employing flexural and tensile tests, whereas samples at ϕ_{CMC}=3.5 vol% were characterized using torsional tests.

Even though the absolute value of the cohesion depends on the load type, the change in maximal failure stress as a function of DS and Mw is independent of the load type.

Figure 6.14A and B show scanning electron microscopy (SEM) images of a thick and corresponding thin electrode layer including CMC with M_w=250 kDa and DS=0.9 at ϕ_{CMC}=4 vol%, respectively. Porosity measurements yield similar values for the thick and thin layer. Moreover, no recognizable difference in electrode microstructure can be established from the micrographs, suggesting that the cohesion values obtained for thick layers are representative also for conventional thin layers.

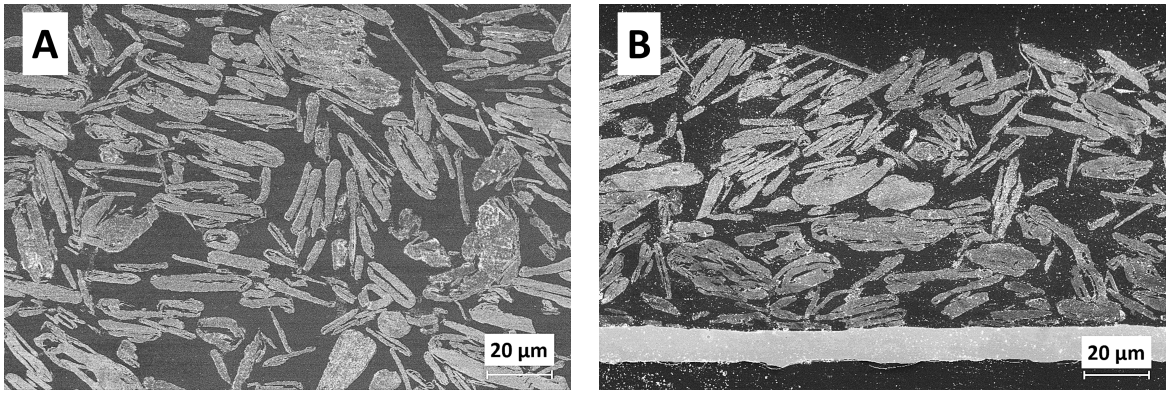

Figure 6.14: SEM micrographs of (A) thick and corresponding (B) thin electrode layer including ϕ_{CMC}=4 vol%, DS=0.9 and Mw=250 kDa.

The intrinsic mechanical strength of the added CMC was investigated employing tensile tests using dog-bone shaped polymer films. The intrinsic tensile strength neither depends on DS nor on M_w as shown in Figure 6.15.

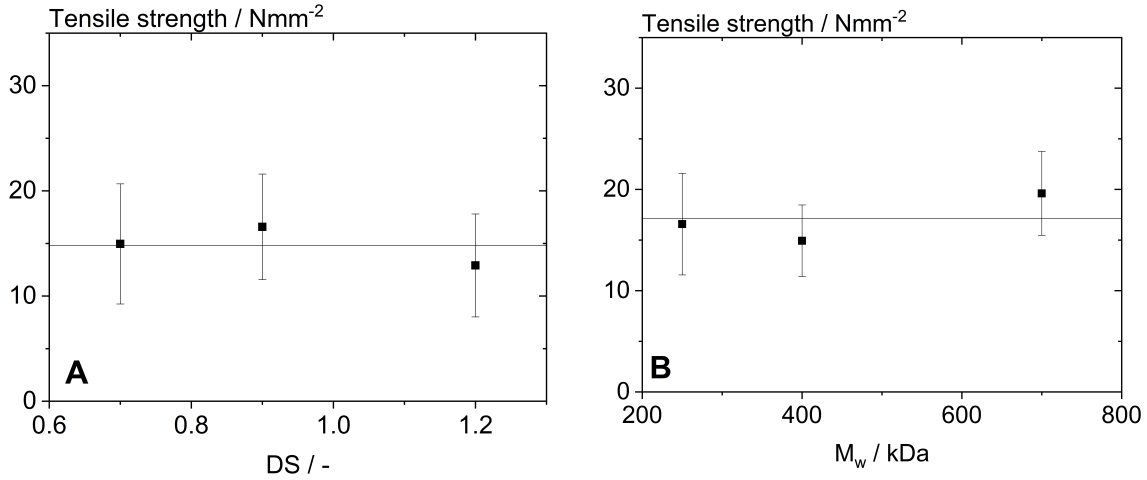

Figure 6.15: Intrinsic tensile strength of pure CMC films as a function of (A) DS but constant M_w=250 kDa and (B) M_w but constant DS=0.9.

Figure 6.16 shows the cohesive strength of thick anode layers including CMC with

constant concentration, M_w and DS but varying SBR concentration and type. The maximum failure stress does not depend on SBR type and concentration.

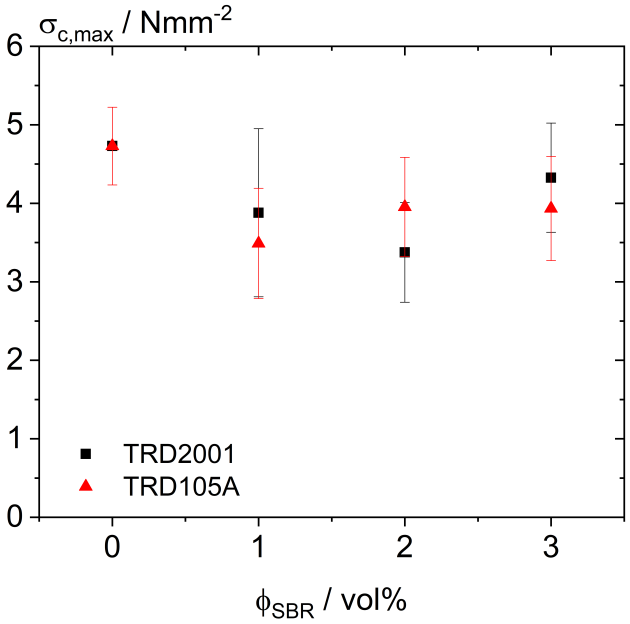

Figure 6.16: Maximum failure stress of thick electrode layers as function of SBR concentration for to different SBR types including CMC with constant ϕ_{CMC}=2.5 vol%, M_w=700 kDa and DS=0.9.

7 Summary

Lithium-ion batteries are the most promising energy storage technology set to revolutionize the energy industry, optimizing power consumption while decreasing environmental impact. LIB is the dominant technology for portable and medical devices as well as the battery of choice to power electric vehicles reshaping modern transportation. Even large-scale LIB technologies are being developed to link intermittent renewables such as solar and wind power with the electric grid aiming to transform the world's electricity system for the better. Thus, LIB are instrumental to shift from a society dependent on fossils to a renewable-fueled world.
After their first appearance in 1970 and commercialization in 1991, extensive research activities have been dealing with the development of LIB. In particular, studies focused on new electrochemically active materials to achieve higher power and energy densities. However, electrochemically inactive components such as polymeric binders have not been equally investigated, despite their key importance to the mechanical stability of the electrode. Furthermore, safety and environmental concerns demand the transition from systems based on organic solvents, associated to conventionally used polymers, to water-borne alternatives. This involves the application of innovative water-soluble polymeric binders. Thus, the development of water-based electrodes for LIB using suitable polymeric binders is of utmost importance.

This cumulative dissertation presented the results of experimental work focused on the role of polymeric binders in electrodes for lithium-ion batteries. Specifically, the effect of commonly used binders on environmentally benign, water-based graphite anodes and $LiFePO_4$ cathodes were thoroughly discussed. The main results were divided in three sections consisting of a peer-reviewed scientific paper, each.

In section 4, we introduced two different characterization methods to determine the sedimentation process of $LiFePO_4$ (LFP) and carbon black (CB) particles in opaque suspensions used for LIB electrodes. The presented methods render an alternative for typically used optical investigation techniques based on low particle concentration and high optical transparency of the sample. Noninvasive spin-echo-based magnetic resonance imaging (MRI) experiments were carried out at a particle mass fraction of ϕ_m=0.5 wt%. Intensity data from MR images was derived from the contrast in ^{1}H-MRI between particles and liquid. The evolution of the intensity profiles was described as the particle settling front and modeled by an exponentially decaying function to determine the sedimentation velocity of the studied particle classes. ^{1}H images uncovered the spatial distribution of the particles and corresponding agglomerates as well as the shape of the settling front, providing new detailed insights into the particle sedimentation process in opaque suspensions. Even though this method yielded reliable and reproducible results, reasonable limits must be outlined. Low-viscosity suspensions normally exhibit high particle settling velocities, which represent high acquisition rates, i.e. lower MRI measuring timescales. This could prove to be challenging for conclusive image definition. In contrast, high particle mass fractions could lead to high viscosities, increasing the

measuring time to unpractical time frames. Moreover highly concentrated suspensions could result in higher signal intensity distortion, hindering data analysis. Supplementing the MRI experiments, the increase in mass fraction over time due to sedimentation of particles at high, technically relevant concentrations (ϕ_{m}=10, 30, 50 wt%) was studied gravimetrically using a self-manufactured sedimentation balance. The decay of the measured mass concentration over time described by this method is in good agreement with the time-dependent, exponential decay of the sedimentation velocity obtained by the MRI method. Diluted LFP suspensions showed higher particle settling velocities at short measuring times, whereas high particle concentrations and associated higher suspension viscosity lead to overall lower sedimentation velocities. Regarding the industrial application of the investigated opaque suspensions, the settling behavior of a highly concentrated (ϕ_{m}=58 wt%), water-based cathode slurry, including LFP, CB, dispersants and rheology control agents as well as a rubber-like polymer was studied, showing reliable and reproducible results. Even though, a similar sedimentation behavior was obtained, the addition of polymers serving as particle dispersing agent and thickener for the continuous phase slows down sedimentation significantly. Accordingly, the presented methods yield a complementing combination to characterize the sedimentation behavior of opaque suspensions with different particle loading for LIB.

The role of carboxymethyl cellulose (CMC) and a fluorine/acrylate hybrid polymer (FAHP) as polymeric binders in water-based $LiFePO_4$ cathodes for LIB was thoroughly investigated in section 5. Solid particle volume fraction and mass ratio between $LiFePO_4$ and CB were kept constant and the concentration of CMC and FAHP was systematically varied in a wide range. Rheological data of wet cathode slurries exhibited a pronounced minimum at a critical CMC concentration ϕ_{CMC}. The initial decrease in yield stress τ_{y} and high shear viscosity η_{∞} was attributed to the adsorption of polymer on the solid particle surface improving particle dispersion due to the electrosteric repulsion counteracting the van der Waals attraction. After particle surface saturation, further addition of CMC lead to higher fractions of dissolved CMC in the aqueous phase, which, in turn, causes an attractive depletion interaction among particles and a stronger thickening effect as indicated by the increase in τ_{y} and η_{∞}, respectively. In contrast to the variation of ϕ_{CMC}, the addition of FAHP has no significant influence on particle dispersion and flow behavior of the slurries. Interestingly, the electrical conductivity exhibits a pronounced maximum at a critical ϕ_{CMC} close to that at which τ_{y} and η_{∞} of the slurry exhibit a minimum, indicating optimum particle dispersion and confirming the impact of CMC on the particle network in the wet slurry as well as on the microstructure of corresponding dry layers. Increasing FAHP concentration ϕ_{FAHP}, on the other hand, leads to a monotonic decrease of conductivity. Adhesion tests show low intrinsic adhesion of CMC to the aluminum foil. Accordingly, the adhesive strength of cathode layers including CMC as the only binder is on a technically inacceptable, low level and is irrespective of ϕ_{CMC}. However, adhesion monotonically increases with increasing ϕ_{FAHP} due to its high affinity to aluminum and hence absolute values 10 times higher than without this polymer are reached for $\phi_{\mathrm{FAHP}} > 5$ vol%. Even though the increase in adhesion comes at the expense of a loss in electrical conductivity, both parameters excel reported values

for similar water-based $LiFePO_4$ cathodes using alternative polymeric binders. Furthermore, we systematically investigated the cohesive strength of cathodes layers for the first time based on compression tests carried out on thick films with similar microstructure and porosity as corresponding thin layers. These experiments yield a linear increase of cohesive strength with increasing ϕ_{CMC} and ϕ_{FAHP}. Despite its lower intrinsic mechanical strength, this increase in cathode cohesion is, remarkably, more pronounced with added CMC than with FAHP. Scanning electron microscopy (SEM) micrographs and accompanying image analysis revealed a strong effect of CMC on particle orientation at high ϕ_{CMC}. In contrast, a random particle orientation was obtained upon variation of ϕ_{FAHP}. Consequently, particle alignment governed by polymer type and concentration seem to control the mechanical integrity of the cathode layer.

Section 6 thoroughly discuss the effect of CMC concentration, molecular weight M_w and degree of substitution DS on rheological properties of aqueous graphite-based anode slurries as well as electrical conductivity, mechanical integrity and microstructure of corresponding dry electrodes. In addition, the influence of styrene butadiene rubber (SBR) as secondary binder on the mentioned electrode properties was also addressed. Rheological data were used to discuss not only the flow behavior of aqueous anode slurries but also adsorption behavior of CMC on particle surface and the particle degree of dispersion at technically relevant conditions. As expected, the absolute viscosity values monotonically increase with increasing ϕ_{CMC}. Low and high shear viscosity increase with M_w and levels off for M_w>400 kDa, whereas the relative high shear viscosity $\eta_{r,\infty}$ monotonically decreases with increasing polymer chain-length irrespective of ϕ_{CMC}. Accordingly, the fraction of adsorbed CMC on particle surface increases with increasing M_w, decreasing the amount of dissolved CMC in the solvent. This was supported by the relationship between relative zero shear viscosity $\eta_{r,0}$ and particle loading ϕ_p for graphite suspensions at constant ϕ_{CMC}, elucidating the adsorption behavior of CMC on graphite particle surface. The addition of SBR does not affect the flow behavior of anode slurries. Interestingly, the electrical conductivity of corresponding dry layers strongly increases with increasing M_w at constant ϕ_{CMC}, whereas DS has no significant effect on conductivity. As indicated by rheological data, longer polymer chains lead to higher fractions of adsorbed polymer, decreasing the amount of randomly distributed polymer and alleviating electrical isolation. Thus, electrical conductivity can be improved through targeted choice of CMC. As expected, increasing ϕ_{CMC} as well as ϕ_{SBR} results in a monotonic decay of electrical conductivity due to the remaining free polymer in the layer, deteriorating electron pathways. CMC hardly contributes to the adhesive strength of anode layers irrespective of ϕ_{CMC}, M_w or DS as suggested by 90°-peel tests. In contrast, addition of SBR leads to a linear increase of adhesion, confirming the role of the secondary polymer. We investigated the electrode cohesive strength employing different well-defined load types to characterize the critical stress σ_{max} at which electrode layers break, yielding reproducible and reliable results and rendering first cohesion data for water-based graphite anodes. Cohesive strength decreases with DS but substantially increases with increasing M_w, even though the intrinsic mechanical strength of CMC is independent of this characteristics. SEM micrographs and image analysis revealed

a strong orientation of graphite particles for anodes including CMC with high M_w or low DS. Accordingly, the degree of CMC adsorption on graphite particles, determined by polymer molecule architecture and chain-length, has a strong impact on electrode microstructure and, in turn, on mechanical integrity.

In summary, this dissertation renders a comprehensive and systematic study through a holistic approach on the role of polymeric binders in water-based electrodes for LIB, unveiling clear relationships between polymer properties and resulting electrode characteristics. The presented findings offer further understanding regarding flow behavior and hence processing properties of electrode slurries but also new insights into the effect of polymer adsorption and particle dispersion on electrical conductivity of dry layers as well as conclusive correlations between microstructure formation and mechanical integrity of the electrode. This work provides the basis to fine-tune slurry processing behavior and optimize electrode mechanical properties at minimal polymer consumption, targeting polymers with specific characteristics. Consequently, optimal electrochemical performance and superior mechanical cycle stability of LIB cells might be achieved. Regarding these final and decisive cell features, preliminary results of the electrochemical behavior of cells including selected electrode compositions can be found in the next section.

8 Outlook

This work systematically elucidates the effect of commonly used polymeric binders on flow behavior of aqueous electrode slurries as well as electrical and mechanical properties of corresponding dry electrodes, unveiling a close relationship between polymer-particle/particle-particle interactions and electrode microstructure ultimately defining electron transport kinetics and electrode mechanical integrity. Still, the impact of these findings on the electrochemical performance as well as mechanical degradation and battery lifetime of the battery must be addressed. Very first preliminary results are presented below.

Selected anodes and cathodes investigated in this work were punched to 12 mm round electrodes, which were previously calendered to an average loading of 4 $mgcm^{-2}$ and 8 $mgcm^{-2}$ for anodes and cathodes, respectively. The porosity was adjusted through the calendering-step, reducing it from 52 % and 61 % to 26 % and 49 % for anodes and cathodes, respectively. Coin-type battery cells were assembled and cycled in temperature-controlled chambers at 25° using the CCCV charging approach on a Maccor 4000 Series automated test system (Maccor Inc., USA) at Institute of Nanotechnology (INT), Joint Laboratory BELLA, KIT/BASF. The rate capability of half-cells including selected anode compositions investigated here paired with elemental lithium as counter-electrode was examined at different current rates (C-rates) regarding the effect of CMC concentration ϕ_{CMC}, molecular weight M_w and degree of substitution DS as well as of SBR type (see Figure 8.1). Half-cells including the investigated anodes exhibit overall outstanding discharge capacity values, considering the graphite theoretical specific capacity of 372 $mAhg^{-1}$, yielding near 100% coulombic efficiency throughout the entire measuring interval. As shown in section 6.5.2, the electrical conductivity of dry anode layers decreases with increasing ϕ_{CMC} due to the randomly distributed CMC in the electrode layer, deteriorating and interrupting conductive pathways. Accordingly, higher capacities should be obtained for electrodes with higher conductivity considering the relationships between cell capacity and ion/electron kinetics. This reasoning is confirmed as indicated by the higher absolute values of discharge capacity for cells including anodes with lower CMC fraction (see Figure 8.1A). Contrary to our findings of higher electrical conductivity values at higher M_w and suggesting an analog behavior of corresponding cell capacity, lower discharge capacities are obtained for cells including anodes with higher M_w as shown in Figure 8.1B. Cells including anodes with different DS yield no significant impact of this CMC characteristic on discharge capacity considering the measurement uncertainty (see Figure 8.1C), agreeing with our previous results indicating no effect of DS on electrical conductivity. Finally, anodes including two different SBR types (TRD2001 and TRD105A) exhibit no notable influence on the discharge capacity of the cell under variation of C-rate compared to cells including anodes without SBR as displayed in Figure 8.1D despite the fact that corresponding SBR-based anode layers show significantly lower electrical conductivity values.

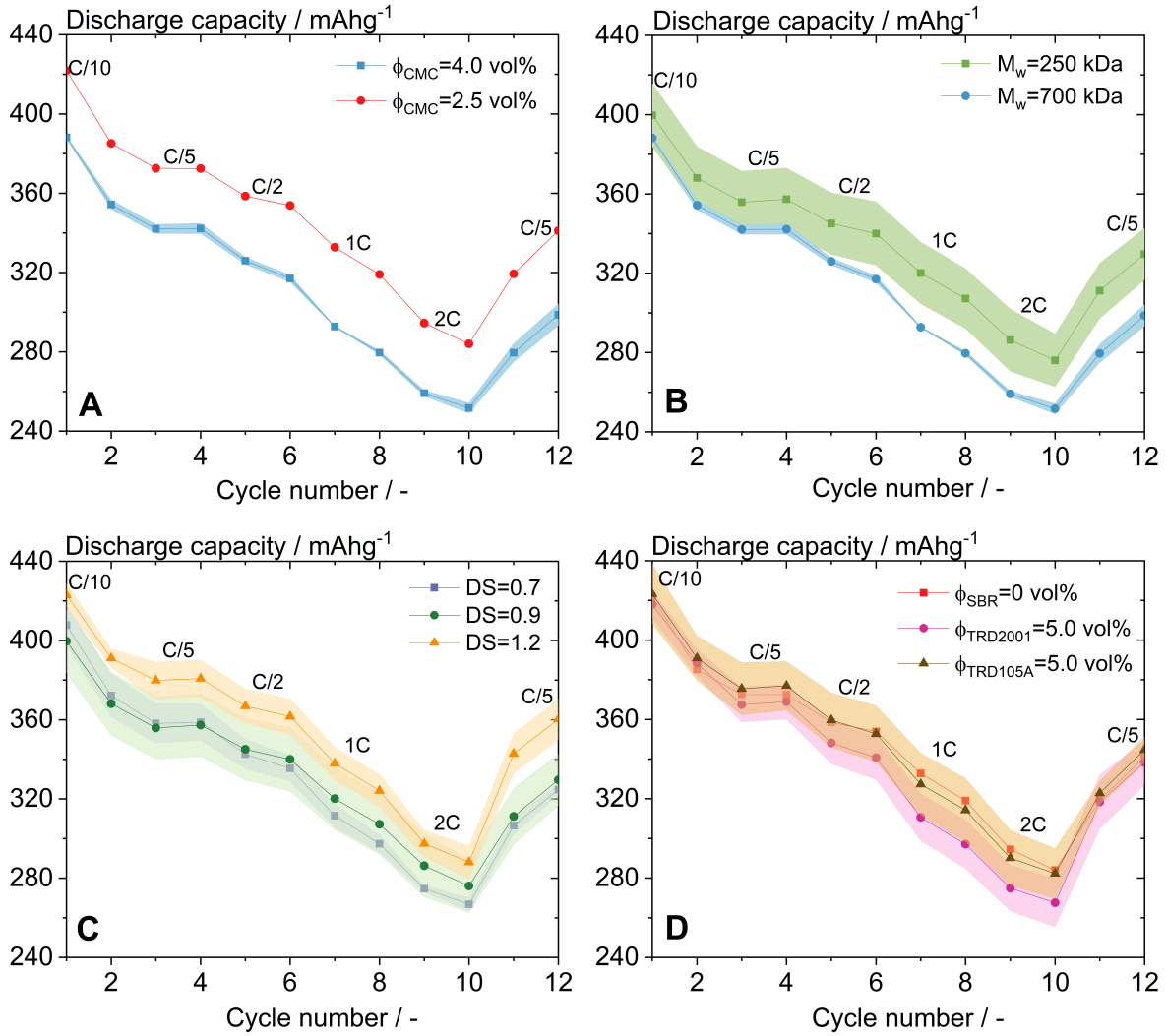

Figure 8.1: Discharge capacity as a function of cycle number at different C-rates for half-cells including anodes with different ϕ_{CMC} at constant M_w=700 kDa and DS=0.9 (A), different M_w at constant ϕ_{CMC}=4.0 vol% and DS=0.9 (B), different DS at constant ϕ_{CMC}=4.0 vol% and M_w=250 kDa (C) as well as different SBR type at constant ϕ_{CMC}=2.5 vol%, M_w=700 kDa and DS=0.9 (D).

For further characterization of the electrochemical behavior of anode half-cells, long-term cycling tests should be carried out to analyze the role of the binder at longer service life. The effects of volume fluctuations due to Li-intercalation on the mechanical integrity of the electrode can only be studied at higher cycle life. This examination would enable the correlation between mechanical properties determined by electrode microstructure and long-term cycle stability of the cell.

On the other hand, coin-type battery cells including selected cathode compositions

investigated in this work paired with elemental lithium were assembled and cycled analog to the anode-based half-cells. Figure 8.2A shows the discharge capacity of cells including cathodes with different polymer concentration and type. As expected, cells comprising cathodes with only CMC as polymer binder exhibit higher initial discharge capacities for lower ϕ_{CMC} since corresponding electrode layers yield higher electrical conductivity values due to the lower amount of CMC distributed in the layer. However, capacity decreases rapidly from cycle 23 on and monotonically decays with a higher slope than that of the capacity curve of cells including cathodes with higher ϕ_{CMC}. This behavior is attributed to the superior cohesive strength of cathodes with higher CMC fractions, mitigating mechanical stresses due to lithiation-driven volume changes. This hypothesis is supported by the significantly higher overall discharge capacity values throughout the investigated cycle life obtained for cells based on cathodes with CMC and FAHP at ϕ_{FAHP}=5 vol% as secondary binder. This complementing binder system provides cohesive as well as adhesive strength to the cathode, leading to clearly higher cycle stability of the corresponding cell. These results are in good agreement with the expected electrochemical behavior derived from the presented findings with respect to the effect of the polymers studied here on the electrical and mechanical properties as well as their microstructure. It must be noted, that two different electrolytes were used for these coin-cells since FAHP was not compatible with the commonly used electrolyte. Thus, the higher absolute discharge capacity of cathodes including FAHP compared to that of cathodes including only CMC is probably associated to the different electrolyte properties. It is assumed that the overall values over the investigated cycle range of the CMC-based cathodes would be shifted to similar initial discharge capacity values of cathodes including FAHP. The rate capability test of the cells performed between cycle 12 and 21 yields overall good cell stability and capacity recovery upon current variation (see Figure 8.2B). Further, initial coulombic efficiencies of over 97% were obtained.

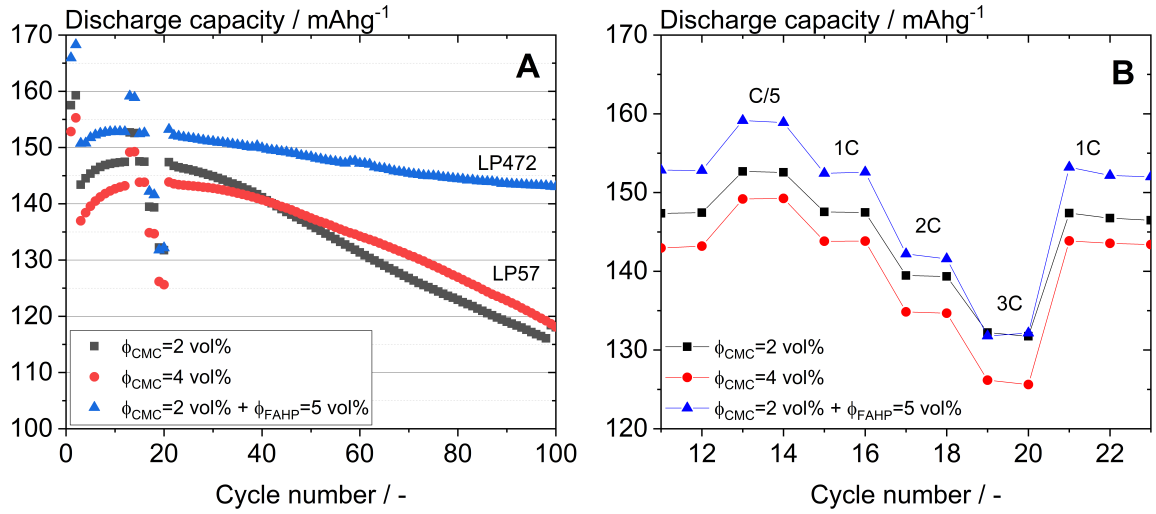

Figure 8.2: Discharge capacity as a function of cycle number (A) and corresponding rate capability (B) for half-cells including cathodes with different ϕ_{CMC} at constant M_w=700 kDa and DS=0.9 as well as with FAHP as secondary binder at constant ϕ_{CMC}=2 vol%, M_w=700 kDa and DS=0.9.

In addition to the half-cell investigation, coin-type full-cells including three selected anode compositions and all three studied cathode variations were assembled and cycled. The long-term discharge capacity and the rate capability of the cells was plotted for one anode composition against the investigated cathodes as well as for one cathode system against the selected anode variations to simplify the interpretation of the results. Figure 8.3 exemplary shows the discharge capacity as function of cycle number as well as the corresponding rate capability between cycle 12 and 21 of full-cells including the investigated cathodes paired with an anode comprising ϕ_{CMC}=2.5 vol%, M_w=700 kDa, DS=0.9 and $\phi_{TRD105A}$=5 vol%. The remaining plots of the studied cells can be found in the appendix section of this work. Considering the nature of the studied systems, i.e. water-based $LiFePO_4$-cathodes, all cells exhibit remarkably high discharge capacities and outstanding long-term cycle stability, yielding capacity retention values above 94% after 250 cycles. At constant anode composition, cell discharge capacity increases with increasing ϕ_{CMC} in the cathode. The overall highest capacity values are obtained for cells including cathodes based on the combination of CMC and FAHP as binder system. A trend can be recognized in relation to the findings from the cathode half-cells study and the relationship between electrochemical behavior and mechanical integrity of corresponding electrodes. The rate capability also yields a more stable performance for cells including cathodes associated with higher mechanical strength. These trends can be observed for analog cells comprising anodes with different composition as well (see appendix). It should be noted that the discharge capacities of full-cells are not visibly dependent on the anode composition (see appendix). It can, therefore, be assumed that the discharge capacity of the investigate full-cells is independent of the selected anode.

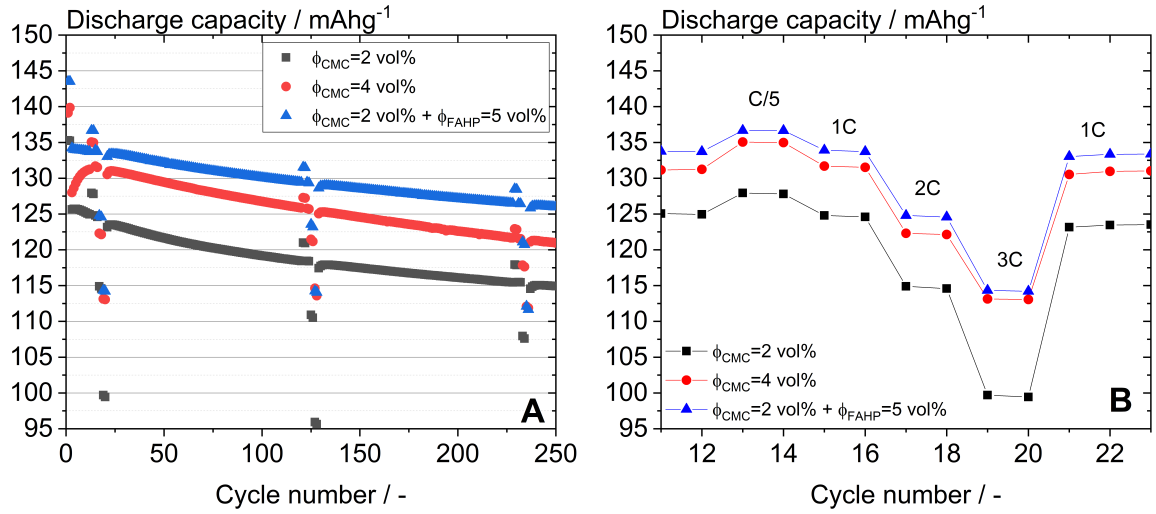

Figure 8.3: Discharge capacity as a function of cycle number (A) and corresponding rate capability (B) for full-cells including cathodes with different ϕ_{CMC} at constant M_w=700 kDa and DS=0.9 as well as with FAHP as secondary binder at constant ϕ_{CMC}=2 vol%, M_w=700 kDa and DS=0.9 paired with an anode with constant ϕ_{CMC}=2.5 vol%, M_w=700 kDa, DS=0.9 and $\phi_{TRD105A}$=5 vol%.

This preliminary half- and full-cells investigation offers a first insight into the role of polymeric binders in water-based electrodes for LIB, particularly into the relationship between electrochemical performance of battery cells and corresponding electrode properties such as electrical conductivity, mechanical integrity and microstructure. However, future work, which should take up the topic presented here, must conduct further research concerning the electrochemical behavior to allow for a detailed correlation between electrode properties and cell performance, focusing on the polymer role. In addition to long-term cycling tests for anode half-cells, cyclic voltametry measurements to elucidate kinetic-driven processes inside the electrode as well as impedance spectroscopy examinations to track processes leading to resistance build-up should be carried out. More importantly, a post-mortem characterization of aged battery cells applying physico-chemical analysis techniques such as scanning electron microscopy (SEM), transmission electron microscopy (TEM), energy-dispersive X-ray spectroscopy (EDX), X-ray photoelectron spectroscopy (XPS) or inductively coupled plasma optical emission spectrometry (ICP-OES) must be performed to identify degradation mechanisms and their correlation with the applied polymeric system. Finally, the electrode composition regarding electrode loading as well as components fraction and ratio could be optimize to further improve the resulting battery performance and facilitate the introduction of fully water-based electrodes to the battery industrial sector.

Based on the knowledge deduced from the results presented in this thesis as well as earlier work [243, 244], a novel electrode architecture could be fabricated using staged

electrode layers rendering a tailor-made binder concept to achieve superior electrode performance at reduced polymer fraction. The findings outlined in this work imply that a multimodal molecular weight distribution of CMC will provide high stability and good processing behavior of the electrode slurry as well as strong cohesion in the dry electrode layer at a low polymer consumption, whereas rubber-like polymeric binders provide sufficient adhesive strength. Low molecular-weight CMC can stabilize particles against agglomeration at low polymer concentration, whereas high molecular-weight CMC can control the slurry flow behavior and improve the cohesive strength of the dry layer. A lab-scale slot-die coater may be used to apply an electrode double-layer (wet-on-wet). A thin layer including SBR may be deposited directly on the current collector and a second layer without SBR but optimized type and amount of CMC may be applied on top (see Figure 8.4A). SBR is avoided in this layer because its contribution to the cohesive strength comes at the expense of electrical conductivity as shown in this thesis (see Figure 6.3B). In addition, staged electrodes including two layers differing not only in SBR content but also in porosity can be fabricated. This can be achieved using the capillary suspension concept [243, 244]. A conventionally prepared slurry including SBR may be applied on the current collector to achieve a dense layer of active material with good adhesive properties and on top a SBR-free slurry including the same active ingredients stabilized by octanol as an immiscible, secondary fluid may be applied (see Figure 8.4B). This stabilization concept results in a higher porosity of the dry layer beneficial for Li-ion transport during electrochemical cycling.

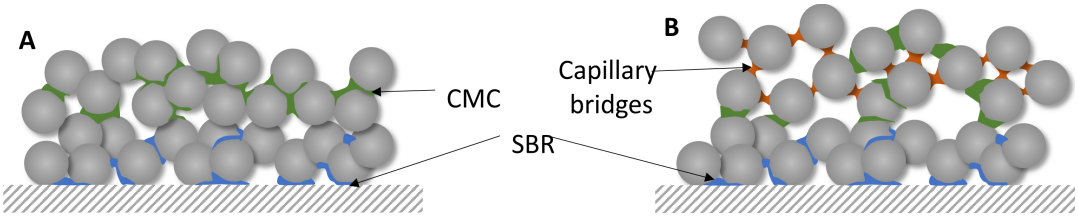

Figure 8.4: Schematic illustration of staged electrodes consisting of a thin layer including SBR directly on the current collector and a second layer without SBR but optimized type and amount of CMC (A) as well as a thin layer including SBR and on top a SBR-free layer based on the capillary suspension concept including CMC as binder for cohesive strength and octanol as a secondary fluid controlling porosity (B).

9 Appendix

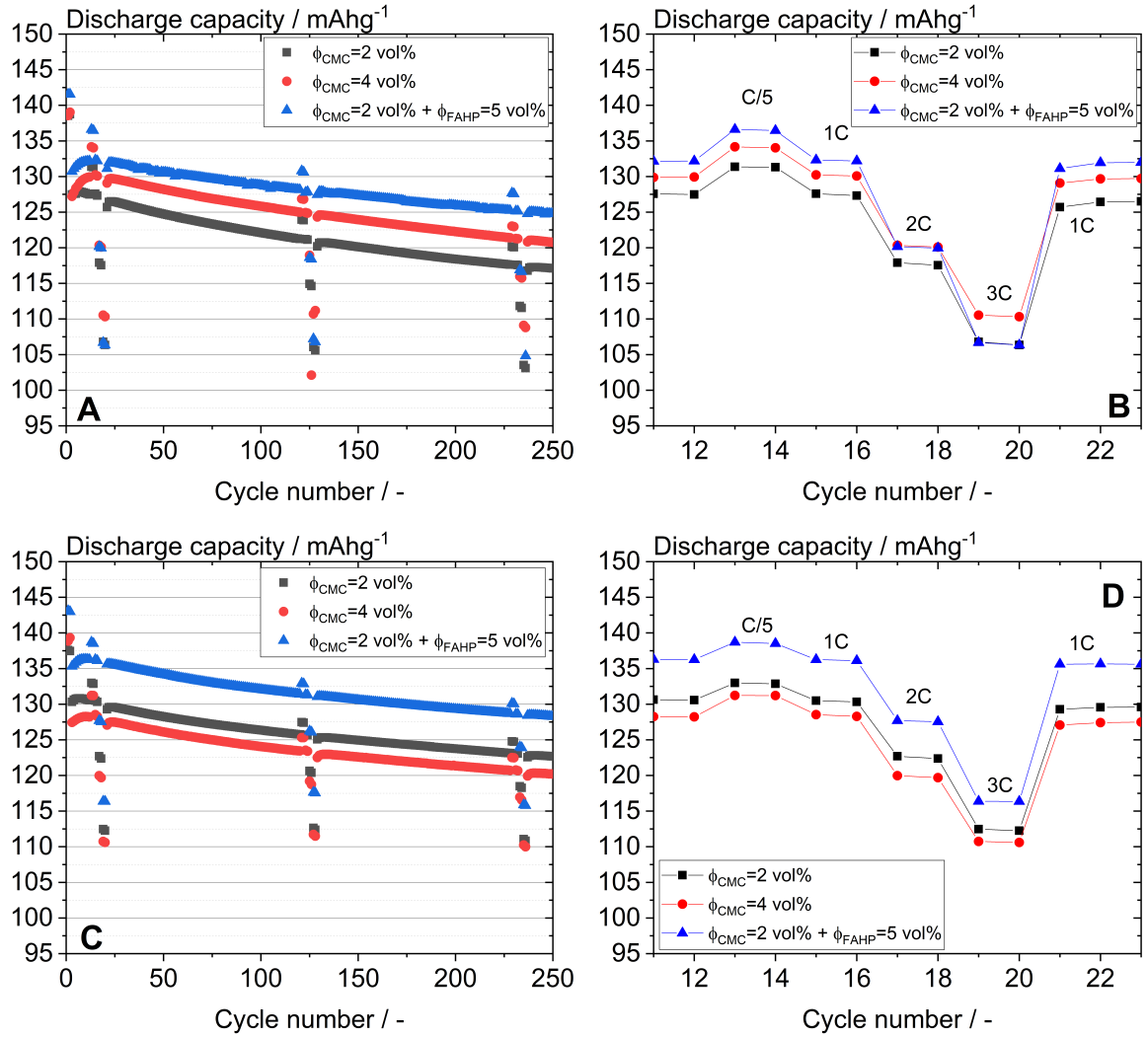

Figure 9.1: Discharge capacity as a function of cycle number and corresponding rate capability for full-cells including cathodes at different ϕ_{CMC} at constant M_w=700 kDa and DS=0.9 as well as with FAHP as secondary binder at constant ϕ_{CMC}=2 vol%, M_w=700 kDa and DS=0.9 paired with an anode with ϕ_{CMC}=4 vol%, M_w=700 kDa and DS=0.9 (A, B) and an anode with ϕ_{CMC}=4 vol%, M_w=250 kDa and DS=0.7 (C, D).

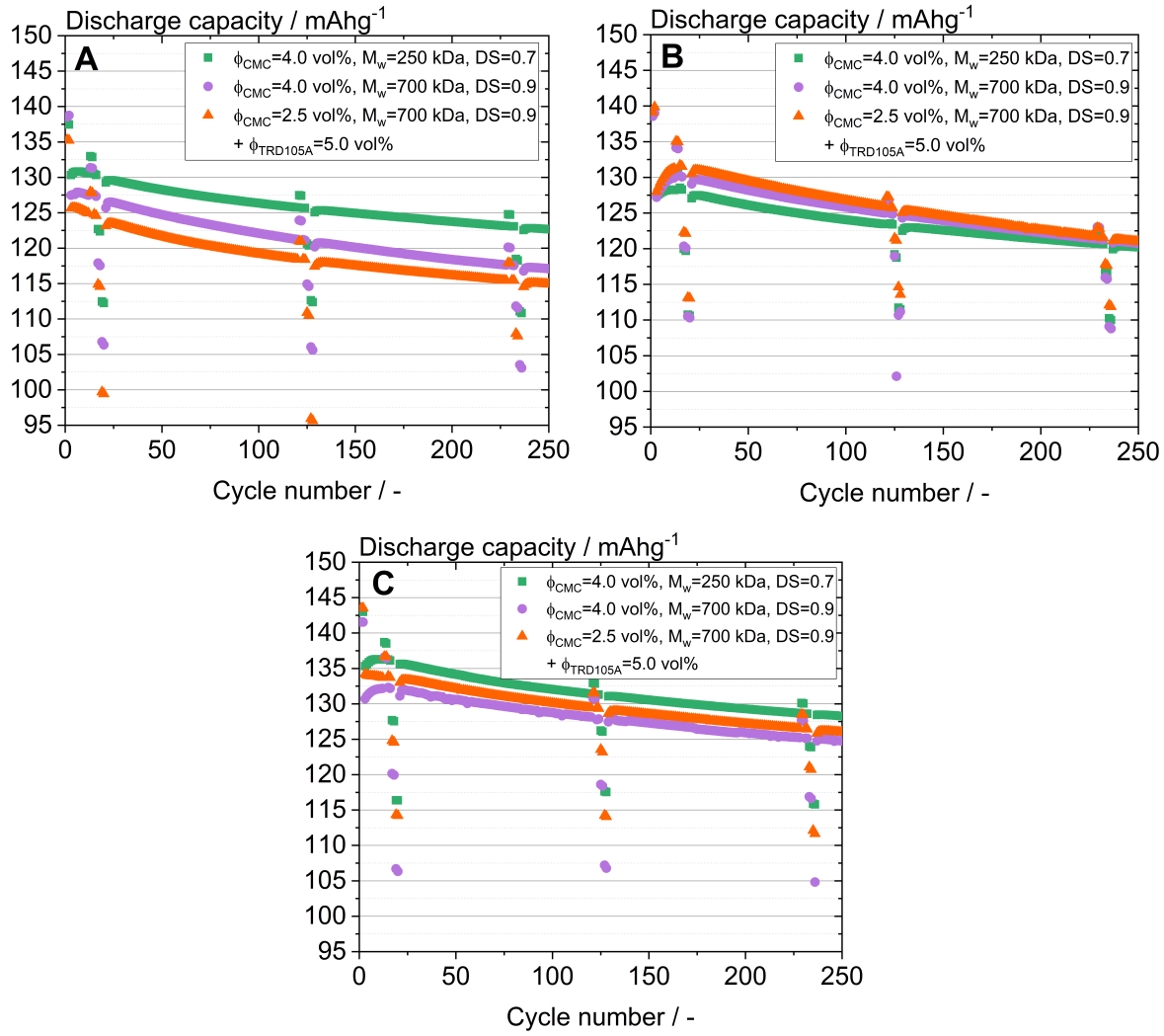

Figure 9.2: Discharge capacity as a function of cycle number for full cells including anodes with ϕ_{CMC}=4 vol%, M_w=250 kDa and DS=0.7; ϕ_{CMC}=4 vol%, M_w=700 kDa and DS=0.9; ϕ_{CMC}=2 vol%, M_w=700 kDa and DS=0.9 in addition to $\phi_{TRD105A}$=5 vol% paired with cathodes including CMC with M_w=700 kDa, DS=0.9 and ϕ_{CMC}=2 vol% (A), ϕ_{CMC}=4 vol% (B) as well as ϕ_{CMC}=2 vol% + ϕ_{FAHP}=5 vol% (C).

References

[1] D. Larcher and J. M. Tarascon, "Towards greener and more sustainable batteries for electrical energy storage," *Nature Chemistry*, vol. 7, no. 1, pp. 19–29, 2015.

[2] B. Dunn, H. Kamath, and J.-M. Tarascon, "Electrical Energy Storage for the Grid: A Battery of Choices," *Science*, vol. 334, pp. 928–935, nov 2011.

[3] X. Luo, J. Wang, M. Dooner, and J. Clarke, "Overview of current development in electrical energy storage technologies and the application potential in power system operation," *Applied Energy*, vol. 137, pp. 511–536, 2015.

[4] D. Deng, "Li-ion batteries: Basics, progress, and challenges," *Energy Science and Engineering*, vol. 3, no. 5, pp. 385–418, 2015.

[5] G. E. Blomgren, "The Development and Future of Lithium Ion Batteries," *Journal of The Electrochemical Society*, vol. 164, no. 1, pp. A5019–A5025, 2017.

[6] J. Mewis and N. J. Wagner, *Colloidal Suspension Rheology*. Cambridge: Cambridge University Press, 2011.

[7] W. B. Russel, D. A. Saville, and W. R. Schowalter, *Colloidal Dispersions*. Cambridge University Press, dec 1989.

[8] H. C. Hamaker, "The London-van der Waals attraction between spherical particles," *Physica*, vol. 4, no. 10, pp. 1058–1072, 1937.

[9] A. V. Vrij, "Polymers At Interfaces And The Interactions in Colloidal Dispersions," *Pure and Applied Chemistry*, vol. 48, no. 4, pp. 471–483, 1976.

[10] H. N. Lekkerkerker and R. Tuinier, *Colloids and the Depletion Interaction*, vol. 833 of *Lecture Notes in Physics*. Dordrecht: Springer Netherlands, 2011.

[11] D. Welch, M. P. Lettinga, M. Ripoll, Z. Dogic, and G. A. Vliegenthart, "Trains, tails and loops of partially adsorbed semi-flexible filaments," *Soft Matter*, vol. 11, no. 38, pp. 7507–7514, 2015.

[12] B. Kronberg, K. Holmberg, and B. Lindman, *Surface Chemistry of Surfactants and Polymers*. Chichester, UK: John Wiley & Sons, Ltd, oct 2014.

[13] T. Tadros, "Interaction forces between particles containing grafted or adsorbed polymer layers," *Advances in Colloid and Interface Science*, vol. 104, pp. 191–226, jul 2003.

[14] J.-M. Tarascon and M. Armand, "Issues and challenges facing rechargeable lithium batteries," in *Materials for Sustainable Energy*, pp. 171–179, Co-Published with Macmillan Publishers Ltd, UK, oct 2001.

[15] B. Scrosati and J. Garche, "Lithium batteries: Status, prospects and future," *Journal of Power Sources*, vol. 195, no. 9, pp. 2419–2430, 2010.

[16] N. Nitta, F. Wu, J. T. Lee, and G. Yushin, "Li-ion battery materials: Present and future," *Materials Today*, vol. 18, no. 5, pp. 252–264, 2015.

[17] J. Gao, S. Q. Shi, and H. Li, "Brief overview of electrochemical potential in lithium ion batteries," *Chinese Physics B*, vol. 25, no. 1, 2015.

[18] X. Han, L. Lu, Y. Zheng, X. Feng, Z. Li, J. Li, and M. Ouyang, "A review on the key issues of the lithium ion battery degradation among the whole life cycle," *eTransportation*, vol. 1, p. 100005, 2019.

[19] M. S. Islam and C. A. Fisher, "Lithium and sodium battery cathode materials: Computational insights into voltage, diffusion and nanostructural properties," *Chemical Society Reviews*, vol. 43, no. 1, pp. 185–204, 2014.

[20] M. Winter, J. O. Besenhard, M. E. Spahr, and P. Novák, "Insertion Electrode Materials for Rechargeable Lithium Batteries," *Advanced Materials*, vol. 10, pp. 725–763, jul 1998.

[21] M. S. Whittingham, "Lithium batteries and cathode materials," *Chemical Reviews*, vol. 104, no. 10, pp. 4271–4301, 2004.

[22] A. K. Padhi, "Phospho-olivines as Positive-Electrode Materials for Rechargeable Lithium Batteries," *Journal of The Electrochemical Society*, vol. 144, no. 4, p. 1188, 1997.

[23] A. Yamada, S. C. Chung, and K. Hinokuma, "Optimized LiFePO[sub 4] for Lithium Battery Cathodes," *Journal of The Electrochemical Society*, vol. 148, no. 3, p. A224, 2001.

[24] D. D. MacNeil, Z. Lu, Z. Chen, and J. R. Dahn, "A comparison of the electrode/electrolyte reaction at elevated temperatures for various Li-ion battery cathodes," *Journal of Power Sources*, vol. 108, no. 1-2, pp. 8–14, 2002.

[25] N. Iltchev, Y. Chen, S. Okada, and J. I. Yamaki, "LiFePO4 storage at room and elevated temperatures," *Journal of Power Sources*, vol. 119-121, pp. 749–754, 2003.

[26] K. Striebel, J. Shim, V. Srinivasan, and J. Newman, "Comparison of LiFePO[sub 4] from Different Sources," *Journal of The Electrochemical Society*, vol. 152, no. 4, p. A664, 2005.

[27] W. J. Zhang, "Structure and performance of LiFePO4 cathode materials: A review," *Journal of Power Sources*, vol. 196, no. 6, pp. 2962–2970, 2011.

[28] A. S. Andersson and J. O. Thomas, "The source of first-cycle capacity loss in LiFePO4," *Journal of Power Sources*, vol. 97, no. 98, pp. 498–502, 2001.

[29] C. Wang and J. Hong, "Ionic/Electronic Conducting Characteristics of LiFePO[sub 4] Cathode Materials," *Electrochemical and Solid-State Letters*, vol. 10, no. 3, p. A65, 2007.

[30] P. P. Prosini, C. Cento, M. Carewska, and A. Masci, "Electrochemical performance of Li-ion batteries assembled with water-processable electrodes," *Solid State Ionics*, vol. 274, no. July, pp. 34–39, 2015.

[31] H. Huang, S.-C. Yin, and L. F. Nazar, "Approaching Theoretical Capacity of LiFePO[sub 4] at Room Temperature at High Rates," *Electrochemical and Solid-State Letters*, vol. 4, no. 10, p. A170, 2001.

[32] M. Thackeray, "An unexpected conductor," *Nature Materials*, vol. 1, no. 2, pp. 81–82, 2002.

[33] S. Y. Chung, J. T. Bloking, and Y. M. Chiang, "Electronically conductive phospho-olivines as lithium storage electrodes," *Nature Materials*, vol. 1, no. 2, pp. 123–128, 2002.

[34] F. Croce, A. D' Epifanio, J. Hassoun, A. Deptula, T. Olczac, and B. Scrosati, "A Novel Concept for the Synthesis of an Improved LiFePO[sub 4] Lithium Battery Cathode," *Electrochemical and Solid-State Letters*, vol. 5, no. 3, p. A47, 2002.

[35] S.-Y. Chung and Y.-M. Chiang, "Microscale Measurements of the Electrical Conductivity of Doped LiFePO[sub 4]," *Electrochemical and Solid-State Letters*, vol. 6, no. 12, p. A278, 2003.

[36] P. S. Herle, B. Ellis, N. Coombs, and L. F. Nazar, "Nano-network electronic conduction in iron and nickel olivine phosphates," *Nature Materials*, vol. 3, no. 3, pp. 147–152, 2004.

[37] C. Delacourt, P. Poizot, S. Levasseur, and C. Masquelier, "Size Effects on Carbon-Free LiFePO[sub 4] Powders," *Electrochemical and Solid-State Letters*, vol. 9, no. 7, p. A352, 2006.

[38] Y. S. Hu, Y. G. Guo, R. Dominko, M. Gaberscek, J. Jamnik, and J. Maier, "Improved electrode performance of porous LiFePO4 using RuO 2 as an oxidic nanoscale interconnect," *Advanced Materials*, vol. 19, no. 15, pp. 1963–1966, 2007.

[39] I. Bilecka, A. Hintennach, M. D. Rossell, D. Xie, P. Novák, and M. Niederberger, "Microwave-assisted solution synthesis of doped LiFePO4 with high specific charge and outstanding cycling performance," *Journal of Materials Chemistry*, vol. 21, no. 16, pp. 5881–5890, 2011.

[40] X. Qi, B. Blizanac, A. Dupasquier, M. Oljaca, J. Li, and M. Winter, "Understanding the influence of conductive carbon additives surface area on the rate performance of LiFePO4 cathodes for lithium ion batteries," *Carbon*, vol. 64, pp. 334–340, 2013.

[41] K. Mizushima, P. Jones, P. Wiseman, and J. Goodenough, "LixCoO2: A new cathode material for batteries of high energy density," *Solid State Ionics*, vol. 3-4, pp. 171–174, aug 1981.

[42] R. Yazami, N. Lebrun, M. Bonneau, and M. Molteni, "High performance LiCoO2 positive electrode material," *Journal of Power Sources*, vol. 54, no. 2, pp. 389–392, 1995.

[43] S. Yamada, M. Fujiwara, and M. Kanda, "Synthesis and properties of LiNiO2 as cathode material for secondary batteries," *Journal of Power Sources*, vol. 54, pp. 209–213, apr 1995.

[44] M. Broussely, F. Perton, P. Biensan, J. Bodet, J. Labat, A. Lecerf, C. Delmas, A. Rougier, and J. Pérès, "LixNiO2, a promising cathode for rechargeable lithium batteries," *Journal of Power Sources*, vol. 54, pp. 109–114, mar 1995.

[45] H. Arai, "Reversibility of LiNiO2 cathode," *Solid State Ionics*, vol. 95, pp. 275–282, mar 1997.

[46] R. Chen, "Cathodic Behavior of Alkali Manganese Oxides from Permanganate," *Journal of The Electrochemical Society*, vol. 144, no. 4, p. L64, 1997.

[47] R. J. Gummow, "An Investigation of Spinel-Related and Orthorhombic LiMnO[sub 2] Cathodes for Rechargeable Lithium Batteries," *Journal of The Electrochemical Society*, vol. 141, no. 5, p. 1178, 1994.

[48] I. J. Davidson, R. S. McMillan, J. J. Murray, and J. E. Greedan, "Lithium-ion cell based on orthorhombic LiMnO2," *Journal of Power Sources*, vol. 54, no. 2, pp. 232–235, 1995.

[49] R. Gummow, A. de Kock, and M. Thackeray, "Improved capacity retention in rechargeable 4 V lithium/lithium-manganese oxide (spinel) cells," *Solid State Ionics*, vol. 69, pp. 59–67, apr 1994.

[50] Z. Liu, A. Yu, and J. Y. Lee, "Synthesis and characterization of LiNi1-x-yCoxMnyO2 as the cathode materials of secondary lithium batteries," *Journal of Power Sources*, vol. 81-82, no. 2, pp. 416–419, 1999.

[51] T. Ohzuku and Y. Makimura, "Layered lithium insertion material of LiCo1/3Ni1/3Mn1/3O2 for lithium-ion batteries," *Chemistry Letters*, no. 7, pp. 642–643, 2001.

[52] K. Shaju, G. Subba Rao, and B. Chowdari, "Performance of layered Li(Ni1/3Co1/3Mn1/3)O2 as cathode for Li-ion batteries," *Electrochimica Acta*, vol. 48, pp. 145–151, nov 2002.

[53] N. Tran, L. Croguennec, C. Labrugère, C. Jordy, P. Biensan, and C. Delmas, "Layered Li1+x(Ni0.425Mn0.425Co0.15)1-xO2 Positive Electrode Materials for Lithium-Ion Batteries," *Journal of The Electrochemical Society*, vol. 153, no. 2, p. A261, 2006.

[54] D. Aurbach, E. Zinigrad, H. Teller, and P. Dan, "Factors Which Limit the Cycle Life of Rechargeable Lithium (Metal) Batteries," *Journal of The Electrochemical Society*, vol. 147, no. 4, p. 1274, 2000.

[55] L. Cheng, H.-J. Liu, J.-J. Zhang, H.-M. Xiong, and Y.-Y. Xia, "Nanosized Li[sub 4]Ti[sub 5]O[sub 12] Prepared by Molten Salt Method as an Electrode Material for Hybrid Electrochemical Supercapacitors," *Journal of The Electrochemical Society*, vol. 153, no. 8, p. A1472, 2006.

[56] D. Liu, C. Ouyang, J. Shu, J. Jiang, Z. Wang, and L. Chen, "Theoretical study of cation doping effect on the electronic conductivity of Li4Ti5O12," *Physica Status Solidi (B) Basic Research*, vol. 243, no. 8, pp. 1835–1841, 2006.

[57] W. J. Zhang, "A review of the electrochemical performance of alloy anodes for lithium-ion batteries," *Journal of Power Sources*, vol. 196, no. 1, pp. 13–24, 2011.

[58] M. Ge, X. Fang, J. Rong, and C. Zhou, "Review of porous silicon preparation and its application for lithium-ion battery anodes," *Nanotechnology*, vol. 24, no. 42, 2013.

[59] X. Su, Q. Wu, J. Li, X. Xiao, A. Lott, W. Lu, B. W. Sheldon, and J. Wu, "Silicon-Based nanomaterials for lithium-ion batteries: A review," *Advanced Energy Materials*, vol. 4, no. 1, 2014.

[60] Q. Zhang, H. Chen, L. Luo, B. Zhao, H. Luo, X. Han, J. Wang, C. Wang, Y. Yang, T. Zhu, and M. Liu, "Harnessing the concurrent reaction dynamics in active Si and Ge to achieve high performance lithium-ion batteries," *Energy and Environmental Science*, vol. 11, no. 3, pp. 669–681, 2018.

[61] J. Yang, Y. Wang, W. Li, L. Wang, Y. Fan, W. Jiang, W. Luo, Y. Wang, B. Kong, C. Selomulya, H. K. Liu, S. X. Dou, and D. Zhao, "Amorphous TiO2 Shells: A Vital Elastic Buffering Layer on Silicon Nanoparticles for High-Performance and Safe Lithium Storage," *Advanced Materials*, vol. 29, no. 48, pp. 1–7, 2017.

[62] R. Dominko, M. Gaberscek, J. Drofenik, M. Bele, S. Pejovnik, and J. Jamnik, "The role of carbon black distribution in cathodes for Li ion batteries," *Journal of Power Sources*, vol. 119-121, pp. 770–773, 2003.

[63] R. Dominko, M. Gaberšček, J. Drofenik, M. Bele, and J. Jamnik, "Influence of carbon black distribution on performance of oxide cathodes for Li ion batteries," *Electrochimica Acta*, vol. 48, no. 24, pp. 3709–3716, 2003.

[64] S. Kuroda, N. Tobori, M. Sakuraba, and Y. Sato, "Charge-discharge properties of a cathode prepared with ketjen black as the electro-conductive additive in lithium ion batteries," *Journal of Power Sources*, vol. 119-121, pp. 924–928, 2003.

[65] H. C. Shin, W. I. Cho, and H. Jang, "Electrochemical properties of carbon-coated LiFePO4 cathode using graphite, carbon black, and acetylene black," *Electrochimica Acta*, vol. 52, no. 4, pp. 1472–1476, 2006.

[66] X. Li, F. Kang, X. Bai, and W. Shen, "A novel network composite cathode of LiFePO4/multiwalled carbon nanotubes with high rate capability for lithium ion batteries," *Electrochemistry Communications*, vol. 9, no. 4, pp. 663–666, 2007.

[67] J. Moskon, R. Dominko, R. Cerc-Korosec, M. Gaberscek, and J. Jamnik, "Morphology and electrical properties of conductive carbon coatings for cathode materials," *Journal of Power Sources*, vol. 174, no. 2, pp. 683–688, 2007.

[68] Y. Liu, X. Li, H. Guo, Z. Wang, W. Peng, Y. Yang, and R. Liang, "Effect of carbon nanotube on the electrochemical performance of C-LiFePO4/graphite battery," *Journal of Power Sources*, vol. 184, no. 2, pp. 522–526, 2008.

[69] F. Y. Su, C. You, Y. B. He, W. Lv, W. Cui, F. Jin, B. Li, Q. H. Yang, and F. Kang, "Flexible and planar graphene conductive additives for lithium-ion batteries," *Journal of Materials Chemistry*, vol. 20, no. 43, pp. 9644–9650, 2010.

[70] B. Zhang, Y. Yu, Y. Liu, Z. D. Huang, Y. B. He, and J. K. Kim, "Percolation threshold of graphene nanosheets as conductive additives in Li4Ti5O12 anodes of Li-ion batteries," *Nanoscale*, vol. 5, no. 5, pp. 2100–2106, 2013.

[71] H. Bockholt, W. Haselrieder, and A. Kwade, "Intensive Dry and Wet Mixing Influencing the Structural and Electrochemical Properties of Secondary Lithium-Ion Battery Cathodes," *ECS Transactions*, vol. 50, no. 26, pp. 25–35, 2013.

[72] V. Wenzel, R. S. Moeller, and H. Nirschl, "Influence of Mixing Technology and the Potential to Modify the Morphological Properties of Materials used in the Manufacture of Lithium-Ion Batteries," *Energy Technology*, vol. 2, no. 2, pp. 176–182, 2014.

[73] W. Bauer, D. Nötzel, V. Wenzel, and H. Nirschl, "Influence of dry mixing and distribution of conductive additives in cathodes for lithium ion batteries," *Journal of Power Sources*, vol. 288, pp. 359–367, 2015.

[74] H. Bockholt, W. Haselrieder, and A. Kwade, "Intensive powder mixing for dry dispersing of carbon black and its relevance for lithium-ion battery cathodes," *Powder Technology*, vol. 297, pp. 266–274, 2016.

[75] D. Bresser, D. Buchholz, A. Moretti, A. Varzi, and S. Passerini, "Alternative binders for sustainable electrochemical energy storage-the transition to aqueous

electrode processing and bio-derived polymers," *Energy and Environmental Science*, vol. 11, no. 11, pp. 3096–3127, 2018.

[76] V. Haufroid, V. K. Jaeger, S. Jeggli, R. Eisenegger, A. Bernard, D. Friedli, D. Lison, and P. Hotz, "Biological monitoring and health effects of low-level exposure to N-methyl-2-pyrrolidone: A cross-sectional study," *International Archives of Occupational and Environmental Health*, vol. 87, no. 6, pp. 663–674, 2014.

[77] G. Berckmans, M. Messagie, J. Smekens, N. Omar, L. Vanhaverbeke, and J. V. Mierlo, "Cost projection of state of the art lithium-ion batteries for electric vehicles up to 2030," *Energies*, vol. 10, no. 9, 2017.

[78] M. Valvo, A. Liivat, H. Eriksson, C. W. Tai, and K. Edström, "Iron-Based Electrodes Meet Water-Based Preparation, Fluorine-Free Electrolyte and Binder: A Chance for More Sustainable Lithium-Ion Batteries?," *ChemSusChem*, vol. 10, no. 11, pp. 2431–2448, 2017.

[79] T. Heinze and A. Koschella, "Carboxymethyl ethers of cellulose and starch - A review," *Macromolecular Symposia*, vol. 223, pp. 13–39, 2005.

[80] W. M. Kulicke, A. H. Kull, W. Kull, H. Thielking, J. Engelhardt, and J. B. Pannek, "Characterization of aqueous carboxymethylcellulose solutions in terms of their molecular structure and its influence on rheological behaviour," *Polymer*, vol. 37, no. 13, pp. 2723–2731, 1996.

[81] U. Kästner, H. Hoffmann, R. Dönges, and J. Hilbig, "Structure and solution properties of sodium carboxymethyl cellulose," *Colloids and Surfaces A: Physicochemical and Engineering Aspects*, vol. 123-124, pp. 307–328, may 1997.

[82] C. W. Hoogendam, A. de Keizer, M. A. Cohen Stuart, B. H. Bijsterbosch, J. G. Batelaan, and P. M. van der Horst, "Adsorption Mechanisms of Carboxymethyl Cellulose on Mineral Surfaces," *Langmuir*, vol. 14, no. 14, pp. 3825–3839, 1998.

[83] R. Barbucci, A. Magnani, and M. Consumi, "Swelling behavior of carboxymethylcellulose hydrogels in relation to cross-linking, pH, and charge density," *Macromolecules*, vol. 33, no. 20, pp. 7475–7480, 2000.

[84] D. Truzzolillo, F. Bordi, C. Cametti, and S. Sennato, "Counterion condensation of differently flexible polyelectrolytes in aqueous solutions in the dilute and semidilute regime," *Physical Review E - Statistical, Nonlinear, and Soft Matter Physics*, vol. 79, no. 1, pp. 1–9, 2009.

[85] C. G. Lopez, S. E. Rogers, R. H. Colby, P. Graham, and J. T. Cabral, "Structure of sodium carboxymethyl cellulose aqueous solutions: A SANS and rheology study," *Journal of Polymer Science, Part B: Polymer Physics*, vol. 53, no. 7, pp. 492–501, 2015.

[86] K. M. Kim, W. S. Jeon, I. J. Chung, and S. H. Chang, "Effect of mixing sequences on the electrode characteristics of lithium-ion rechargeable batteries," *Journal of Power Sources*, vol. 83, no. 1-2, pp. 108–113, 1999.

[87] C.-C. Li and Y.-S. Lin, "Interactions between organic additives and active powders in water-based lithium iron phosphate electrode slurries," *Journal of Power Sources*, vol. 220, pp. 413–421, dec 2012.

[88] J. C. Tsai, F. Y. Tsai, C. A. Tung, H. W. Hsieh, and C. C. Li, "Gelation or dispersion of LiFePO4 in water-based slurry?," *Journal of Power Sources*, vol. 241, pp. 400–403, 2013.

[89] H. Nakajima, T. Kitahara, Y. Higashinaka, and Y. Nagata, "Effect of Electrode Mixing Conditions on the Performance of Lithium-Ion Batteries Analyzed by Fast Fourier Transform Electrochemical Impedance Spectroscopy," *ECS Transactions*, vol. 64, pp. 87–95, apr 2015.

[90] S. Lim, K. H. Ahn, and M. Yamamura, "Latex migration in battery slurries during drying," *Langmuir*, vol. 29, no. 26, pp. 8233–8244, 2013.

[91] M. Baunach, S. Jaiser, S. Schmelzle, H. Nirschl, P. Scharfer, and W. Schabel, "Delamination behavior of lithium-ion battery anodes: Influence of drying temperature during electrode processing," *Drying Technology*, vol. 34, no. 4, pp. 462–473, 2016.

[92] S. Jaiser, M. Müller, M. Baunach, W. Bauer, P. Scharfer, and W. Schabel, "Investigation of film solidification and binder migration during drying of Li-Ion battery anodes," *Journal of Power Sources*, vol. 318, pp. 210–219, 2016.

[93] S. Jaiser, N. Sanchez Salach, M. Baunach, P. Scharfer, and W. Schabel, "Impact of drying conditions and wet film properties on adhesion and film solidification of lithium-ion battery anodes," *Drying Technology*, vol. 35, no. 15, pp. 1807–1817, 2017.

[94] S. Jaiser, J. Kumberg, J. Klaver, J. L. Urai, W. Schabel, J. Schmatz, and P. Scharfer, "Microstructure formation of lithium-ion battery electrodes during drying – An ex-situ study using cryogenic broad ion beam slope-cutting and scanning electron microscopy (Cryo-BIB-SEM)," *Journal of Power Sources*, vol. 345, pp. 97–107, 2017.

[95] H. Zheng, J. Li, X. Song, G. Liu, and V. S. Battaglia, "A comprehensive understanding of electrode thickness effects on the electrochemical performances of Li-ion battery cathodes," *Electrochimica Acta*, vol. 71, pp. 258–265, 2012.

[96] H. Y. Tran, G. Greco, C. Täubert, M. Wohlfahrt-Mehrens, W. Haselrieder, and A. Kwade, "Influence of electrode preparation on the electrochemical performance of LiNi0.8Co0.15Al0.05O2composite electrodes for lithium-ion batteries," *Journal of Power Sources*, vol. 210, no. July, pp. 276–285, 2012.

[97] J. Smekens, R. Gopalakrishnan, N. Van den Steen, N. Omar, O. Hegazy, A. Hubin, and J. Van Mierlo, "Influence of electrode density on the performance of Li-ion batteries: Experimental and simulation results," *Energies*, vol. 9, no. 2, pp. 1–12, 2016.

[98] S. Yoo, C. Hong, K. T. Chong, and N. Seul, "Analysis of pouch performance to ensure impact safety of lithium-ion battery," *Energies*, vol. 12, no. 15, pp. 1–10, 2019.

[99] C. D. Rahn and C. Y. Wang, *Battery Systems Engineering*. 2013.

[100] S. S. Choi and H. S. Lim, "Factors that affect cycle-life and possible degradation mechanisms of a Li-ion cell based on LiCoO2," *Journal of Power Sources*, vol. 111, no. 1, pp. 130–136, 2002.

[101] M. Broussely, P. Biensan, F. Bonhomme, P. Blanchard, S. Herreyre, K. Nechev, and R. J. Staniewicz, "Main aging mechanisms in Li ion batteries," *Journal of Power Sources*, vol. 146, no. 1-2, pp. 90–96, 2005.

[102] K. Jalkanen, J. Karppinen, L. Skogström, T. Laurila, M. Nisula, and K. Vuorilehto, "Cycle aging of commercial NMC/graphite pouch cells at different temperatures," *Applied Energy*, vol. 154, pp. 160–172, 2015.

[103] C. R. Birkl, M. R. Roberts, E. McTurk, P. G. Bruce, and D. A. Howey, "Degradation diagnostics for lithium ion cells," *Journal of Power Sources*, vol. 341, pp. 373–386, 2017.

[104] M. N. Richard and J. R. Dahn, "Accelerating rate calorimetry studies of the effect of binder type on the thermal stability of a lithiated mesocarbon microbead material in electrolyte," *Journal of Power Sources*, vol. 83, no. 1-2, pp. 71–74, 1999.

[105] D. D. MacNeil, "Comparison of the Reactivity of Various Carbon Electrode Materials with Electrolyte at Elevated Temperature," *Journal of The Electrochemical Society*, vol. 146, no. 10, p. 3596, 1999.

[106] A. M. Andersson, M. Herstedt, A. G. Bishop, and K. Edström, "The influence of lithium salt on the interfacial reactions controlling the thermal stability of graphite anodes," *Electrochimica Acta*, vol. 47, no. 12, pp. 1885–1898, 2002.

[107] M. C. Smart, "Irreversible Capacities of Graphite in Low-Temperature Electrolytes for Lithium-Ion Batteries," *Journal of The Electrochemical Society*, vol. 146, no. 11, p. 3963, 1999.

[108] T. Waldmann, M. Wilka, M. Kasper, M. Fleischhammer, and M. Wohlfahrt-Mehrens, "Temperature dependent ageing mechanisms in Lithium-ion batteries - A Post-Mortem study," *Journal of Power Sources*, vol. 262, pp. 129–135, 2014.

[109] J. Vetter, P. Novák, M. R. Wagner, C. Veit, K. C. Möller, J. O. Besenhard, M. Winter, M. Wohlfahrt-Mehrens, C. Vogler, and A. Hammouche, "Ageing mechanisms in lithium-ion batteries," *Journal of Power Sources*, vol. 147, no. 1-2, pp. 269–281, 2005.

[110] M. M. Kabir and D. E. Demirocak, "Degradation mechanisms in Li-ion batteries: a state-of-the-art review," *International Journal of Energy Research*, vol. 41, pp. 1963–1986, nov 2017.

[111] S. C. Nagpure, B. Bhushan, and S. S. Babu, "Multi-Scale Characterization Studies of Aged Li-Ion Large Format Cells for Improved Performance: An Overview," *Journal of The Electrochemical Society*, vol. 160, no. 11, pp. A2111–A2154, 2013.

[112] A. Mukhopadhyay and B. W. Sheldon, "Deformation and stress in electrode materials for Li-ion batteries," *Progress in Materials Science*, vol. 63, no. January, pp. 58–116, 2014.

[113] S. Ramdon and B. Bhushan, "Nanomechanical characterization and mechanical integrity of unaged and aged Li-ion battery cathodes," *Journal of Power Sources*, vol. 246, pp. 219–224, 2014.

[114] K. E. Aifantis, S. A. Hackney, and R. V. Kumar, eds., *High Energy Density Lithium Batteries*. Wiley, apr 2010.

[115] R. Korthauer, *Handbuch Lithium-Ionen-Batterien*. Berlin, Heidelberg: Springer Berlin Heidelberg, 2013.

[116] M. S. Whittingham, "Electrical Energy Storage and Intercalation Chemistry," *Science*, vol. 192, pp. 1126–1127, jun 1976.

[117] T. Yoshino, Akira; Sanechika, Kenichi; Nakajima, "Secondary battery," 1987.

[118] C. Liu, F. Li, M. Lai-Peng, and H. M. Cheng, "Advanced materials for energy storage," *Advanced Materials*, vol. 22, no. 8, pp. 28–62, 2010.

[119] F. Cheng, J. Liang, Z. Tao, and J. Chen, "Functional materials for rechargeable batteries," *Advanced Materials*, vol. 23, no. 15, pp. 1695–1715, 2011.

[120] T. B. Schon, B. T. McAllister, P. F. Li, and D. S. Seferos, "The rise of organic electrode materials for energy storage," *Chemical Society Reviews*, vol. 45, no. 22, pp. 6345–6404, 2016.

[121] J. H. Lee, U. Paik, V. A. Hackley, and Y. M. Choi, "Effect of poly(acrylic acid) on adhesion strength and electrochemical performance of natural graphite negative electrode for lithium-ion batteries," *Journal of Power Sources*, vol. 161, no. 1, pp. 612–616, 2006.

[122] A. Magasinski, B. Zdyrko, I. Kovalenko, B. Hertzberg, R. Burtovyy, C. F. Huebner, T. F. Fuller, I. Luzinov, and G. Yushin, "Toward efficient binders for Li-ion battery Si-based anodes: Polyacrylic acid," *ACS Applied Materials and Interfaces*, vol. 2, no. 11, pp. 3004–3010, 2010.

[123] Z. Zhang, T. Zeng, Y. Lai, M. Jia, and J. Li, "A comparative study of different binders and their effects on electrochemical properties of LiMn2O4cathode in lithium ion batteries," *Journal of Power Sources*, vol. 247, pp. 1–8, 2014.

[124] D. Shin, H. Park, and U. Paik, "Cross-linked poly(acrylic acid)-carboxymethyl cellulose and styrene-butadiene rubber as an efficient binder system and its physicochemical effects on a high energy density graphite anode for Li-ion batteries," *Electrochemistry Communications*, vol. 77, pp. 103–106, 2017.

[125] D. E. Yoon, C. Hwang, N. R. Kang, U. Lee, D. Ahn, J. Y. Kim, and H. K. Song, "Dependency of Electrochemical Performances of Silicon Lithium-Ion Batteries on Glycosidic Linkages of Polysaccharide Binders," *ACS Applied Materials and Interfaces*, vol. 8, no. 6, pp. 4042–4047, 2016.

[126] D. V. Carvalho, N. Loeffler, G. T. Kim, M. Marinaro, M. Wohlfahrt-Mehrens, and S. Passerini, "Study of water-based lithium titanate electrode processing: The role of pH and binder molecular structure," *Polymers*, vol. 8, no. 8, pp. 1–9, 2016.

[127] M. Sun, H. Zhong, S. Jiao, H. Shao, and L. Zhang, "Investigation on carboxymethyl chitosan as new water soluble binder for LiFePO4 cathode in Li-ion batteries," *Electrochimica Acta*, vol. 127, pp. 239–244, 2014.

[128] K. Prasanna, T. Subburaj, Y. N. Jo, W. J. Lee, and C. W. Lee, "Environment-friendly cathodes using biopolymer chitosan with enhanced electrochemical behavior for use in lithium ion batteries," *ACS Applied Materials and Interfaces*, vol. 7, no. 15, pp. 7884–7890, 2015.

[129] H. Zhong, A. He, J. Lu, M. Sun, J. He, and L. Zhang, "Carboxymethyl chitosan/conducting polymer as water-soluble composite binder for LiFePO4cathode in lithium ion batteries," *Journal of Power Sources*, vol. 336, pp. 107–114, 2016.

[130] C.-C. Li, X.-W. Peng, J.-T. Lee, and F.-M. Wang, "Using Poly(4-Styrene Sulfonic Acid) to Improve the Dispersion Homogeneity of Aqueous-Processed LiFePO[sub 4] Cathodes," *Journal of The Electrochemical Society*, vol. 157, no. 4, p. A517, 2010.

[131] Y. K. Jeong, T. W. Kwon, I. Lee, T. S. Kim, A. Coskun, and J. W. Choi, "Millipede-inspired structural design principle for high performance polysaccharide binders in silicon anodes," *Energy and Environmental Science*, vol. 8, no. 4, pp. 1224–1230, 2015.

[132] J. He, H. Zhong, J. Wang, and L. Zhang, "Investigation on xanthan gum as novel water soluble binder for LiFePO4cathode in lithium-ion batteries," *Journal of Alloys and Compounds*, vol. 714, pp. 409–418, 2017.

[133] M. H. Ryou, J. Kim, I. Lee, S. Kim, Y. K. Jeong, S. Hong, J. H. Ryu, T. S. Kim, J. K. Park, H. Lee, and J. W. Choi, "Mussel-inspired adhesive binders for high-performance silicon nanoparticle anodes in lithium-ion batteries," *Advanced Materials*, vol. 25, no. 11, pp. 1571–1576, 2013.

[134] J. Liu, J.-T. Li, Q.-S. Huang, L. Deng, L. Huang, Y.-Q. Lu, Z.-Y. Wu, T. Zhang, and S.-G. Sun, "Multiple hydrogel alginate binders for Si anodes of lithium-ion battery," *Electrochimica Acta*, vol. 245, pp. 371–378, 2017.

[135] J. Li, R. B. Lewis, and J. R. Dahn, "Sodium Carboxymethyl Cellulose," *Electrochemical and Solid-State Letters*, vol. 10, no. 2, p. A17, 2007.

[136] W. Porcher, B. Lestriez, S. Jouanneau, and D. Guyomard, "Design of Aqueous Processed Thick LiFePO[sub 4] Composite Electrodes for High-Energy Lithium Battery," *Journal of The Electrochemical Society*, vol. 156, no. 3, p. A133, 2009.

[137] S. F. Lux, F. Schappacher, A. Balducci, S. Passerini, and M. Winter, "Low Cost, Environmentally Benign Binders for Lithium-Ion Batteries," *Journal of The Electrochemical Society*, vol. 157, no. 3, p. A320, 2010.

[138] F. Y. Tsai, J. H. Jhang, H. W. Hsieh, and C. C. Li, "Dispersion, agglomeration, and gelation of LiFePO4 in water-based slurry," *Journal of Power Sources*, vol. 310, pp. 47–53, 2016.

[139] S. Lim, S. Kim, K. H. Ahn, and S. J. Lee, "The effect of binders on the rheological properties and the microstructure formation of lithium-ion battery anode slurries," *Journal of Power Sources*, vol. 299, pp. 221–230, 2015.

[140] D. Guy, B. Lestriez, R. Bouchet, and D. Guyomard, "Critical Role of Polymeric Binders on the Electronic Transport Properties of Composites Electrode," *Journal of The Electrochemical Society*, vol. 153, no. 4, p. A679, 2006.

[141] B. Lestriez, "Functions of polymers in composite electrodes of lithium ion batteries," *Comptes Rendus Chimie*, vol. 13, no. 11, pp. 1341–1350, 2010.

[142] G. Liu, H. Zheng, X. Song, and V. S. Battaglia, "Particles and Polymer Binder Interaction: A Controlling Factor in Lithium-Ion Electrode Performance," *Journal of the Electrochemical Society*, vol. 159, no. 3, pp. A214–A221, 2012.

[143] P. Arora, "Capacity Fade Mechanisms and Side Reactions in Lithium-Ion Batteries," *Journal of The Electrochemical Society*, vol. 145, no. 10, p. 3647, 1998.

[144] F. Hao and D. Fang, "Reducing diffusion-induced stresses of electrode-collector bilayer in lithium-ion battery by pre-strain," *Journal of Power Sources*, vol. 242, pp. 415–420, 2013.

[145] E. K. Rahani and V. B. Shenoy, "Role of Plastic Deformation of Binder on Stress Evolution during Charging and Discharging in Lithium-Ion Battery Negative Electrodes," *Journal of the Electrochemical Society*, vol. 160, no. 8, pp. A1153–A1162, 2013.

[146] L. Chen, X. Xie, J. Xie, K. Wang, and J. Yang, "Binder effect on cycling performance of silicon/carbon composite anodes for lithium ion batteries," *Journal of Applied Electrochemistry*, vol. 36, no. 10, pp. 1099–1104, 2006.

[147] H. K. Park, B. S. Kong, and E. S. Oh, "Effect of high adhesive polyvinyl alcohol binder on the anodes of lithium ion batteries," *Electrochemistry Communications*, vol. 13, no. 10, pp. 1051–1053, 2011.

[148] B. Son, M. H. Ryou, J. Choi, T. Lee, H. K. Yu, J. H. Kim, and Y. M. Lee, "Measurement and analysis of adhesion property of lithium-ion battery electrodes with SAICAS," *ACS Applied Materials and Interfaces*, vol. 6, no. 1, pp. 526–531, 2014.

[149] W. Haselrieder, B. Westphal, H. Bockholt, A. Diener, S. Höft, and A. Kwade, "Measuring the coating adhesion strength of electrodes for lithium-ion batteries," *International Journal of Adhesion and Adhesives*, vol. 60, pp. 1–8, 2015.

[150] K. Kim, S. Byun, I. Cho, M. H. Ryou, and Y. M. Lee, "Three-Dimensional Adhesion Map Based on Surface and Interfacial Cutting Analysis System for Predicting Adhesion Properties of Composite Electrodes," *ACS Applied Materials and Interfaces*, vol. 8, no. 36, pp. 23688–23695, 2016.

[151] A. M. Gaikwad and A. C. Arias, "Understanding the Effects of Electrode Formulation on the Mechanical Strength of Composite Electrodes for Flexible Batteries," *ACS Applied Materials and Interfaces*, vol. 9, no. 7, pp. 6390–6400, 2017.

[152] C. R. Hernandez, A. Etiemble, T. Douillard, D. Mazouzi, Z. Karkar, E. Maire, D. Guyomard, B. Lestriez, and L. Roué, "A Facile and Very Effective Method to Enhance the Mechanical Strength and the Cyclability of Si-Based Electrodes for Li-Ion Batteries," *Advanced Energy Materials*, vol. 8, no. 6, pp. 1–13, 2018.

[153] S. Babinec, H. Tang, A. Talik, S. Hughes, and G. Meyers, "Composite cathode structure/property relationships," *Journal of Power Sources*, vol. 174, no. 2, pp. 508–514, 2007.

[154] H. Zheng, L. Zhang, G. Liu, X. Song, and V. S. Battaglia, "Correlationship between electrode mechanics and long-term cycling performance for graphite anode in lithium ion cells," *Journal of Power Sources*, vol. 217, pp. 530–537, 2012.

[155] B. R. Lee and E. S. Oh, "Effect of molecular weight and degree of substitution of a sodium-carboxymethyl cellulose binder on Li4Ti5O12anodic performance," *Journal of Physical Chemistry C*, vol. 117, no. 9, pp. 4404–4409, 2013.

[156] D. Antartis, S. Dillon, and I. Chasiotis, "Effect of porosity on electrochemical and mechanical properties of composite Li-ion anodes," *Journal of Composite Materials*, vol. 49, no. 15, pp. 1849–1862, 2015.

[157] J. Chen, J. Liu, Y. Qi, T. Sun, and X. Li, "Unveiling the Roles of Binder in the Mechanical Integrity of Electrodes for Lithium-Ion Batteries," *Journal of the Electrochemical Society*, vol. 160, no. 9, pp. A1502–A1509, 2013.

[158] R. Balbierer, R. Gordon, S. Schuhmann, N. Willenbacher, H. Nirschl, and G. Guthausen, "Sedimentation of lithium–iron–phosphate and carbon black particles in opaque suspensions used for lithium-ion-battery electrodes," *Journal of Materials Science*, vol. 54, no. 7, pp. 5682–5694, 2019.

[159] S. B. Chikkannanavar, D. M. Bernardi, and L. Liu, "A review of blended cathode materials for use in Li-ion batteries," *Journal of Power Sources*, vol. 248, pp. 91–100, 2014.

[160] H. Wu and Y. Cui, "Designing nanostructured Si anodes for high energy lithium ion batteries," *Nano Today*, vol. 7, no. 5, pp. 414–429, 2012.

[161] T. D. Bogart, A. M. Chockla, and B. A. Korgel, "High capacity lithium ion battery anodes of silicon and germanium," *Current Opinion in Chemical Engineering*, vol. 2, no. 3, pp. 286–293, 2013.

[162] L. A. Berla, S. W. Lee, I. Ryu, Y. Cui, and W. D. Nix, "Robustness of amorphous silicon during the initial lithiation/delithiation cycle," *Journal of Power Sources*, vol. 258, pp. 253–259, 2014.

[163] Z. Zeng, N. Liu, Q. Zeng, Y. Ding, S. Qu, Y. Cui, and W. L. Mao, "Elastic moduli of polycrystalline Li15Si4 produced in lithium ion batteries," *Journal of Power Sources*, vol. 242, pp. 732–735, 2013.

[164] J. Xu, S. Dou, H. Liu, and L. Dai, "Cathode materials for next generation lithium ion batteries," *Nano Energy*, vol. 2, no. 4, pp. 439–442, 2013.

[165] S. Goriparti, E. Miele, F. De Angelis, E. Di Fabrizio, R. Proietti Zaccaria, and C. Capiglia, "Review on recent progress of nanostructured anode materials for Li-ion batteries," *Journal of Power Sources*, vol. 257, pp. 421–443, 2014.

[166] X. Zuo, J. Zhu, P. Müller-Buschbaum, and Y. J. Cheng, "Silicon based lithium-ion battery anodes: A chronicle perspective review," *Nano Energy*, vol. 31, no. October 2016, pp. 113–143, 2017.

[167] Z. Chen, G. T. Kim, D. Chao, N. Loeffler, M. Copley, J. Lin, Z. Shen, and S. Passerini, "Toward greener lithium-ion batteries: Aqueous binder-based LiNi 0.4 Co 0.2 Mn 0.4 O 2 cathode material with superior electrochemical performance," *Journal of Power Sources*, vol. 372, no. September, pp. 180–187, 2017.

[168] J. O. Thomas, A. S. Andersson, B. Kalska, and L. Haggstrom, "Lithium extraction/insertion in LiFePO4: an X-ray diffraction and Mossbauer spectroscopy study," *Solid State Ionics*, vol. 130, pp. 41–52, 2000.

[169] P. Prosini, "Determination of the chemical diffusion coefficient of lithium in LiFePO4," *Solid State Ionics*, vol. 148, pp. 45–51, may 2002.

[170] B. Kenney, K. Darcovich, D. D. MacNeil, and I. J. Davidson, "Modelling the impact of variations in electrode manufacturing on lithium-ion battery modules," *Journal of Power Sources*, vol. 213, pp. 391–401, 2012.

[171] J. Li, B. L. Armstrong, C. Daniel, J. Kiggans, and D. L. Wood, "Optimization of multicomponent aqueous suspensions of lithium iron phosphate (LiFePO4) nanoparticles and carbon black for lithium-ion battery cathodes," *Journal of Colloid and Interface Science*, vol. 405, pp. 118–124, 2013.

[172] W. M. Lu, K. L. Tung, C. H. Pan, and K. J. Hwang, "The effect of particle sedimentation on gravity filtration," *Separation Science and Technology*, vol. 33, no. 12, pp. 1723–1746, 1998.

[173] M. A. Turney, M. K. Cheung, R. L. Powell, and M. J. McCarthy, "Hindered settling of rod-like particles measured with magnetic resonance imaging," *AIChE Journal*, vol. 41, no. 2, pp. 251–257, 1995.

[174] R. Bürger, W. Wendland, and F. Concha, "Model Equations for Gravitational Sedimentation-Consolidation Processes," *ZAMM*, vol. 80, pp. 79–92, feb 2000.

[175] J. Acosta-Cabronero and L. D. Hall, "Measurements by MRI of the settling and packing of solid particles from aqueous suspensions," *AIChE Journal*, vol. 55, pp. 1426–1433, jun 2009.

[176] E. V. Morozov, O. V. Shabanova, and O. V. Falaleev, "MRI Comparative Study of Container Geometry Impact on the PMMA Spheres Sedimentation," *Applied Magnetic Resonance*, vol. 44, no. 5, pp. 619–636, 2013.

[177] B. Zabava, N. Ungureanu, V. Vladut, M. Dinca, G. Voicu, and Ionescu M., "Experimental Study of the Sedimentation of Solid," *Annals of the University of Craiova-Agriculture, Montanology*, vol. XLVI, no. November, pp. 611–617, 2016.

[178] M. Lehtimäki, J. Keskinen, and K. Janka, "Sedimentation Method in Calibrating Optical Particle Counters," *Aerosol Science and Technology*, vol. 12, pp. 711–715, jan 1990.

[179] D. Lerche, "Dispersion stability and particle characterization by sedimentation kinetics in a centrifugal field," *Journal of Dispersion Science and Technology*, vol. 23, no. 5, pp. 699–709, 2002.

[180] N. Azema, "Sedimentation behaviour study by three optical methods - granulometric and electrophoresis measurements, dispersion optical analyser," *Powder Technology*, vol. 165, no. 3, pp. 133–139, 2006.

[181] T. Detloff, T. Sobisch, and D. Lerche, "Particle size distribution by space or time dependent extinction profiles obtained by analytical centrifugation (concentrated systems)," *Powder Technology*, vol. 174, no. 1-2, pp. 50–55, 2007.

[182] S. P. Rwei, F. H. Ku, and K. C. Cheng, "Dispersion of carbon black in a continuous phase: Electrical, rheological, and morphological studies," *Colloid and Polymer Science*, vol. 280, no. 12, pp. 1110–1115, 2002.

[183] M. Kawaguchi, M. Okuno, and T. Kato, "Rheological properties of carbon black suspensions in a silicone oil," *Langmuir*, vol. 17, no. 20, pp. 6041–6044, 2001.

[184] S. Bobroff and R. J. Phillips, "Nuclear magnetic resonance imaging investigation of sedimentation of concentrated suspensions in non-Newtonian fluids," *Journal of Rheology*, vol. 42, no. 6, pp. 1419–1436, 1998.

[185] M. A. Turney, M. K. Cheung, M. J. McCarthy, and R. L. Powell, "Magnetic resonance imaging study of sedimenting suspensions of noncolloidal spheres," *Physics of Fluids*, vol. 7, no. 5, pp. 904–911, 1995.

[186] M. K. Cheung, R. L. Powell, and M. J. McCarthy, "Sedimentation of noncolloidal bidisperse suspensions," *AIChE Journal*, vol. 42, pp. 271–276, jan 1996.

[187] M. C. Tucker, M. M. Doeff, T. J. Richardson, R. Fiñones, J. A. Reimer, and E. J. Cairns, "7Li and 31P magic angle spinning nuclear magnetic resonance of LiFePO4-type materials," *Electrochemical and Solid-State Letters*, vol. 5, no. 5, pp. 5–9, 2002.

[188] M. C. Tucker, M. M. Doeff, T. J. Richardson, R. Fiñones, E. J. Cairns, and J. A. Reimer, "Hyperfine fields at the Li site in LiFePO4-type olivine materials for lithium rechargeable batteries: A 7Li MAS NMR and SQUID study," *Journal of the American Chemical Society*, vol. 124, no. 15, pp. 3832–3833, 2002.

[189] C. P. Grey and N. Dupré, "NMR studies of cathode materials for lithium-ion rechargeable batteries," *Chemical Reviews*, vol. 104, no. 10, pp. 4493–4512, 2004.

[190] S. L. Wilcke, Y. J. Lee, E. J. Cairns, and J. A. Reimer, "Covalency measurements via NMR in lithium metal phosphates," *Applied Magnetic Resonance*, vol. 32, no. 4, pp. 547–563, 2007.

[191] N. Dupré, J. Oliveri, J. Degryse, J. F. Martin, and D. Guyomard, "Characterization of the surface of positive electrodes for Li-ion batteries using 7Li MAS NMR," *Ionics*, vol. 14, no. 3, pp. 203–207, 2008.

[192] A. Buzlukov, G. Gerbaud, C. Bourbon, S. Hediger, G. De Paëpe, S. Patoux, and M. Bardet, "Application of 7Li NMR to characterize the evolution of intercalated and non-intercalated lithium in LiFePO4-based materials for Li-ion batteries," *Journal of Solid State Electrochemistry*, vol. 17, no. 5, pp. 1421–1427, 2013.

[193] T. V. Satyavani, B. Ramya Kiran, V. Rajesh Kumar, A. Srinivas Kumar, and S. V. Naidu, "Effect of particle size on dc conductivity, activation energy and diffusion coefficient of lithium iron phosphate in Li-ion cells," *Engineering Science and Technology, an International Journal*, vol. 19, no. 1, pp. 40–44, 2016.

[194] I. M. Krieger and T. J. Dougherty, "A Mechanism for Non-Newtonian Flow in Suspensions of Rigid Spheres," *Transactions of the Society of Rheology*, vol. 3, no. 1, pp. 137–152, 1959.

[195] D. Quemada, "Rheology of concentrated disperse systems and minimum energy dissipation.," *Rheologica Acta*, vol. 16, pp. 82–94, 1977.

[196] S. P. Meeker, W. C. Poon, and P. N. Pusey, "Concentration dependence of the low-shear viscosity of suspensions of hard-sphere colloids," *Physical Review E - Statistical Physics, Plasmas, Fluids, and Related Interdisciplinary Topics*, vol. 55, no. 5, pp. 5718–5722, 1997.

[197] A. Guerfi, M. Kaneko, M. Petitclerc, M. Mori, and K. Zaghib, "LiFePO4water-soluble binder electrode for Li-ion batteries," *Journal of Power Sources*, vol. 163, no. 2, pp. 1047–1052, 2007.

[198] J. H. Lee, J. S. Kim, Y. C. Kim, D. S. Zang, and U. Paik, "Dispersion properties of aqueous-based LiFePO4 pastes and their electrochemical performance for lithium batteries," *Ultramicroscopy*, vol. 108, no. 10, pp. 1256–1259, 2008.

[199] R. Gordon, M. Kassar, and N. Willenbacher, "Effect of Polymeric Binders on Dispersion of Active Particles in Aqueous LiFePO4 -Based Cathode Slurries as well as on Mechanical and Electrical Properties of Corresponding Dry Layers," *ACS Omega*, vol. 5, pp. 11455–11465, may 2020.

[200] V. H. Nguyen, W. L. Wang, E. M. Jin, and H. B. Gu, "Impacts of different polymer binders on electrochemical properties of LiFePO4 cathode," *Applied Surface Science*, vol. 282, pp. 444–449, 2013.

[201] W. Bauer and D. Nötzel, "Rheological properties and stability of NMP based cathode slurries for lithium ion batteries," *Ceramics International*, vol. 40, no. 3, pp. 4591–4598, 2014.

[202] Z. P. Cai, Y. Liang, W. S. Li, L. D. Xing, and Y. H. Liao, "Preparation and performances of LiFePO4cathode in aqueous solvent with polyacrylic acid as a binder," *Journal of Power Sources*, vol. 189, no. 1, pp. 547–551, 2009.

[203] J. Chong, S. Xun, H. Zheng, X. Song, G. Liu, P. Ridgway, J. Q. Wang, and V. S. Battaglia, "A comparative study of polyacrylic acid and poly(vinylidene difluoride) binders for spherical natural graphite/LiFePO4 electrodes and cells," *Journal of Power Sources*, vol. 196, no. 18, pp. 7707–7714, 2011.

[204] Z. Zhang, T. Zeng, C. Qu, H. Lu, M. Jia, Y. Lai, and J. Li, "Cycle performance improvement of LiFePO 4 cathode with polyacrylic acid as binder," *Electrochimica Acta*, vol. 80, pp. 440–444, 2012.

[205] J. He, J. Wang, H. Zhong, J. Ding, and L. Zhang, "Cyanoethylated Carboxymethyl Chitosan as Water Soluble Binder with Enhanced Adhesion Capability and electrochemical performances for LiFePO4 Cathode," *Electrochimica Acta*, vol. 182, pp. 900–907, 2015.

[206] S. Gao, Y. Su, L. Bao, N. Li, L. Chen, Y. Zheng, J. Tian, J. Li, S. Chen, and F. Wu, "High-performance LiFePO4/C electrode with polytetrafluoroethylene as an aqueous-based binder," *Journal of Power Sources*, vol. 298, pp. 292–298, 2015.

[207] J.-H. Lee, J.-S. Kim, Y. C. Kim, D. S. Zang, Y.-M. Choi, W. I. Park, and U. Paik, "Effect of Carboxymethyl Cellulose on Aqueous Processing of LiFePO[sub 4] Cathodes and Their Electrochemical Performance," *Electrochemical and Solid-State Letters*, vol. 11, no. 10, p. A175, 2008.

[208] W. Porcher, P. Moreau, B. Lestriez, S. Jouanneau, and D. Guyomard, "Is LiFePO[sub 4] Stable in Water?," *Electrochemical and Solid-State Letters*, vol. 11, no. 1, p. A4, 2008.

[209] G. T. Kim, S. S. Jeong, M. Joost, E. Rocca, M. Winter, S. Passerini, and A. Balducci, "Use of natural binders and ionic liquid electrolytes for greener and safer lithium-ion batteries," *Journal of Power Sources*, vol. 196, no. 4, pp. 2187–2194, 2011.

[210] L. Qiu, Z. Shao, D. Wang, W. Wang, F. Wang, and J. Wang, "Enhanced electrochemical properties of LiFePO4(LFP) cathode using the carboxymethyl cellulose lithium (CMC-Li) as novel binder in lithium-ion battery," *Carbohydrate Polymers*, vol. 111, pp. 588–591, 2014.

[211] Q. Wu, S. Ha, J. Prakash, D. W. Dees, and W. Lu, "Investigations on high energy lithium-ion batteries with aqueous binder," *Electrochimica Acta*, vol. 114, pp. 1–6, 2013.

[212] F. A. Çetinel and W. Bauer, "Processing of water-based LiNi1/3Mn1/3Co1/3O2 pastes for manufacturing lithium ion battery cathodes," *Bulletin of Materials Science*, vol. 37, pp. 1685–1690, dec 2014.

[213] K. Notake, T. Gunji, H. Kokubun, S. Kosemura, Y. Mochizuki, T. Tanabe, S. Kaneko, S. Ugawa, H. Lee, and F. Matsumoto, "The application of a water-based hybrid polymer binder to a high-voltage and high-capacity Li-rich solid-solution cathode and its performance in Li-ion batteries," *Journal of Applied Electrochemistry*, vol. 46, no. 3, pp. 267–278, 2016.

[214] T. Tanabe, T. Gunji, Y. Honma, K. Miyamoto, T. Tsuda, Y. Mochizuki, S. Kaneko, S. Ugawa, H. Lee, T. Ohsaka, and F. Matsumoto, "Preparation of Water-Resistant Surface Coated High-Voltage LiNi0.5Mn1.5O4 Cathode and Its Cathode Performance to Apply a Water-Based Hybrid Polymer Binder to Li-Ion Batteries," *Electrochimica Acta*, vol. 224, pp. 429–438, jan 2017.

[215] M. Wu, X. Xiao, N. Vukmirovic, S. Xun, P. K. Das, X. Song, P. Olalde-Velasco, D. Wang, A. Z. Weber, L. W. Wang, V. S. Battaglia, W. Yang, and G. Liu, "Toward an ideal polymer binder design for high-capacity battery anodes," *Journal of the American Chemical Society*, vol. 135, no. 32, pp. 12048–12056, 2013.

[216] H. A. Barnes and J. O. Carnali, "The vane-in-cup as a novel rheometer geometry for shear thinning and thixotropic materials," *Journal of Rheology*, vol. 34, no. 6, pp. 841–866, 1990.

[217] C. Yüce and N. Willenbacher, "Challenges in Rheological Characterization of Highly Concentrated Suspensions - A Case Study for Screen-printing Silver Pastes," *Journal of Visualized Experiments*, pp. 1–17, apr 2017.

[218] F. M. Smits, "Measurement of Sheet Resistivities with the Four-Point Probe," *Bell System Technical Journal*, vol. 37, pp. 711–718, may 1958.

[219] A. Chatterjee and B. Das, "Radii of gyration of sodium carboxymethylcellulose in aqueous and mixed solvent media from viscosity measurement," *Carbohydrate Polymers*, vol. 98, no. 2, pp. 1297–1303, 2013.

[220] R. Gordon, R. Orias, and N. Willenbacher, "Effect of carboxymethyl cellulose on the flow behavior of lithium-ion battery anode slurries and the electrical as well as mechanical properties of corresponding dry layers," *Journal of Materials Science*, vol. 55, no. 33, pp. 15867–15881, 2020.

[221] L. Croguennec and M. R. Palacin, "Recent achievements on inorganic electrode materials for lithium-ion batteries," *Journal of the American Chemical Society*, vol. 137, no. 9, pp. 3140–3156, 2015.

[222] P. Roy and S. K. Srivastava, "Nanostructured anode materials for lithium ion batteries," *Journal of Materials Chemistry A*, vol. 3, no. 6, pp. 2454–2484, 2015.

[223] H. Maleki, G. Deng, I. Kerzhner-Haller, A. Anani, and J. N. Howard, "Thermal Stability Studies of Binder Materials in Anodes for Lithium-Ion Batteries," *Journal of The Electrochemical Society*, vol. 147, no. 12, p. 4470, 2000.

[224] X. Zhang, P. N. Ross, R. Kostecki, F. Kong, S. Sloop, J. B. Kerr, K. Striebel, E. J. Cairns, and F. McLarnon, "Diagnostic Characterization of High Power Lithium-Ion Batteries for Use in Hybrid Electric Vehicles," *Journal of The Electrochemical Society*, vol. 148, no. 5, p. A463, 2001.

[225] D. L. Wood, J. Li, and C. Daniel, "Prospects for reducing the processing cost of lithium ion batteries," *Journal of Power Sources*, vol. 275, pp. 234–242, 2015.

[226] D. L. Wood, J. D. Quass, J. Li, S. Ahmed, D. Ventola, and C. Daniel, "Technical and economic analysis of solvent-based lithium-ion electrode drying with water and NMP," *Drying Technology*, vol. 36, no. 2, pp. 234–244, 2018.

[227] J. H. Lee, S. Lee, U. Paik, and Y. M. Choi, "Aqueous processing of natural graphite particulates for lithium-ion battery anodes and their electrochemical performance," *Journal of Power Sources*, vol. 147, no. 1-2, pp. 249–255, 2005.

[228] J. H. Lee, Y. M. Choi, U. Paik, and J. G. Park, "The effect of carboxymethyl cellulose swelling on the stability of natural graphite particulates in an aqueous medium for lithium ion battery anodes," *Journal of Electroceramics*, vol. 17, no. 2-4, pp. 657–660, 2006.

[229] W.-R. Liu, M.-H. Yang, H.-C. Wu, S. M. Chiao, and N.-L. Wu, "Enhanced Cycle Life of Si Anode for Li-Ion Batteries by Using Modified Elastomeric Binder," *Electrochemical and Solid-State Letters*, vol. 8, no. 2, p. A100, 2005.

[230] H. Buqa, M. Holzapfel, F. Krumeich, C. Veit, and P. Novák, "Study of styrene butadiene rubber and sodium methyl cellulose as binder for negative electrodes in lithium-ion batteries," *Journal of Power Sources*, vol. 161, no. 1, pp. 617–622, 2006.

[231] J.-H. Lee, U. Paik, V. A. Hackley, and Y.-M. Choi, "Effect of Carboxymethyl Cellulose on Aqueous Processing of Natural Graphite Negative Electrodes and their Electrochemical Performance for Lithium Batteries," *Journal of The Electrochemical Society*, vol. 152, no. 9, p. A1763, 2005.

[232] M. Yoo, C. W. Frank, S. Mori, and S. Yamaguchi, "Effect of poly(vinylidene fluoride) binder crystallinity and graphite structure on the mechanical strength of the composite anode in a lithium ion battery," *Polymer*, vol. 44, no. 15, pp. 4197–4204, 2003.

[233] F. Jeschull, D. Brandell, M. Wohlfahrt-Mehrens, and M. Memm, "Water-Soluble Binders for Lithium-Ion Battery Graphite Electrodes: Slurry Rheology, Coating Adhesion, and Electrochemical Performance," *Energy Technology*, vol. 5, no. 11, pp. 2108–2118, 2017.

[234] Z. Chen, L. Christensen, and J. Dahn, "Large-volume-change electrodes for Li-ion batteries of amorphous alloy particles held by elastomeric tethers," *Electrochemistry Communications*, vol. 5, pp. 919–923, nov 2003.

[235] J. T. Lee, Y. J. Chu, X. W. Peng, F. M. Wang, C. R. Yang, and C. C. Li, "A novel and efficient water-based composite binder for LiCoO2 cathodes in lithium-ion batteries," *Journal of Power Sources*, vol. 173, no. 2 SPEC. ISS., pp. 985–989, 2007.

[236] B. Bitsch, N. Willenbacher, V. Wenzel, S. Schmelzle, and H. Nirschl, "Einflüsse der mechanischen Verfahrenstechnik auf die Herstellung von Elektroden für Lithium-Ionen-Batterien," *Chemie-Ingenieur-Technik*, vol. 87, no. 4, pp. 466–474, 2015.

[237] M. Rubinstein and R. H. Colby, "Polymer physics," 2003.

[238] G. K. Batchelor and J. T. Green, "The effect of Brownian motion on the bulk stress in a suspension of spherical particles," *Journal of Fluid Mechanics*, vol. 56, no. 3, pp. 401–427, 1972.

[239] R. J. Roe, "Multilayer theory of adsorption from a polymer solution," *The Journal of Chemical Physics*, vol. 4192, no. August, pp. 4192–4207, 1974.

[240] J. M. Scheutjens and G. J. Fleer, "Statistical theory of the adsorption of interacting chain molecules. 1. Partition function, segment density distribution, and adsorption isotherms," *Journal of Physical Chemistry*, vol. 83, no. 12, pp. 1619–1635, 1979.

[241] J. M. Scheutjens and G. J. Fleer, "Statistical theory of the adsorption of interacting chain molecules. 2. Train, loop, and tail size distribution," *Journal of Physical Chemistry*, vol. 84, no. 2, pp. 178–190, 1980.

[242] J. Park, N. Willenbacher, and K. H. Ahn, "How the interaction between styrene-butadiene-rubber (SBR) binder and a secondary fluid affects the rheology, microstructure and adhesive properties of capillary-suspension-type graphite slurries used for Li-ion battery anodes," *Colloids and Surfaces A: Physicochemical and Engineering Aspects*, vol. 579, p. 123692, oct 2019.

[243] B. Bitsch, J. Dittmann, M. Schmitt, P. Scharfer, W. Schabel, and N. Willenbacher, "A novel slurry concept for the fabrication of lithium-ion battery electrodes with beneficial properties," *Journal of Power Sources*, vol. 265, pp. 81–90, 2014.

[244] B. Bitsch, T. Gallasch, M. Schroeder, M. Börner, M. Winter, and N. Willenbacher, "Capillary suspensions as beneficial formulation concept for high energy density Li-ion battery electrodes," *Journal of Power Sources*, vol. 328, pp. 114–123, 2016.